Numerical Methods for a Reduced Model in Thin–Film Micromagnetics

Dissertation
zur
Erlangung des Doktorgrades (Dr. rer. nat.)
der
Mathematisch–Naturwissenschaftlichen Fakultät
der
Rheinischen Friedrich–Wilhelms–Universität Bonn

vorgelegt von
Jörg Drwenski
aus
Bielefeld

Bonn, Februar 2008

Angefertigt mit Genehmigung der Mathematisch–Naturwissenschaftlichen Fakultät
der Rheinischen Friedrich–Wilhelms–Universität Bonn

1. Gutachter: Prof. Dr. Felix Otto
2. Gutachter: Prof. Dr. Sören Bartels

Tag der Promotion: 26.05.2008

Diese Dissertation ist auf dem Hochschulschriftenserver der ULB Bonn
http://hss.ulb.uni-bonn.de/diss_online elektronisch publiziert.

Erscheinungsjahr: 2008

Danksagung

Mein herzlicher Dank gilt Prof. Dr. Felix Otto für seine kompetente und geduldige Betreuung dieser Doktorarbeit. Besondere Anerkennung verdient Prof. Dr. Ralf Hiptmair, der mir ausführlich die Methode der Finiten Elemente und die Theorie der hierarchischen Matrizen nahe gebracht hat. Mein Dank gilt ebenso Dr. Jörg Ostrowski und Dr. Lars Grasedyck, die mich in die Implementierung der $\mathcal{H}^2$–Matrizen eingeführt haben. Für weitere Anregungen zur Numerik bin ich Prof. Dr. Angela Kunoth dankbar.

Nicht zuletzt möchte ich mich bei allen Kolleginnen und Kollegen der Abteilung für Mathematische Methoden der Physik bedanken, die mir nicht nur mit fachlichen Ratschlägen zur Seite gestanden haben.

Diese Arbeit ist meiner Familie gewidmet. *The great sense of passing through.*

Contents

1 Introduction & Summary

In this thesis, we address the conformal finite element approximation to a reduced model arising in thin–film micromagnetics. In [16], Antonio DeSimone, Robert V. Kohn, Stefan Müller, and Felix Otto derived a reduced 2–d model for a thin–film ferromagnetic element under external field. It generalizes an ad hoc model proposed in [10]. The physical setting considered is purely stationary, no time dependence is included. The interest in soft ferromagnetic films is due to applications in inductive or GMR sensors, as well as magnetoelectronic memory elements, see [37] for an extensive overview.

The thin ferromagnetic sample is described by its cross–section $\Omega' \subset \mathbb{R}^2$ under an in–plane external field H'_{ext}. The micromagnetic energy E of the in–plane magnetization m' consists of two contributions: the energy of the stray field $-\nabla u$, and the Zeeman energy. The energy E is degenerate in the following sense: it depends on m' only via the "magnetic charge density" σ, which is simply the in–plane divergence $-\nabla' \cdot m'$. For weak external field, m' arranges itself in such a way that the stray field $-\nabla' u$ compensates H'_{ext} in the sample. This can be reformulated as a minimization problem for σ. At a critical field strength $|H'_{ext}|$, the constraint $|m'| \leq 1$ becomes active, and the determination of σ and m' turns into a nonlinear problem.

In Section 3, we consider the approximation of m' by Raviart–Thomas elements, which makes the charge density σ a piecewise constant function on Ω'. This *conformal* finite element approximation fits naturally in the theory of discrete de Rham complexes, a common concept of computational electromagnetism. The numerical challenge in micromagnetic simulations is the determination of the stray field, which in our case amounts to the evaluation of the single layer potential operator. Efficient numerical methods for stray field computation therefore occupy a major part of our considerations. We start in Section 4.1 with quadrature schemes for the single layer potential kernel, exploiting its homogeneity, as recommended in [4] for the numerical integration of weakly singular kernels in lower dimensions.

In Section 4.2, we point out that for weak external fields the problem for σ is a variational formulation of the Dirichlet screen problem. More precisely, it can be seen as a boundary integral ansatz for the magnetostatic potential u in $\mathbb{R}^3$ with prescribed Dirichlet data $H'_{ext} \cdot x'$ on $\Omega' \times \{0\}$. The potential u is written as the convolution of σ with the single layer potential on $\Omega' \times \{0\}$. The bilinear form in the variational formulation is the homogeneous part of the $H^{-1/2}(\mathbb{R}^2)$–norm of σ (hereafter called "energy norm", since it is the energy of the stray field $-\nabla u$).

We think of Ω' as being polygonal, $\Omega' = (0,1)^2$ to fix ideas. The charge distribution σ is known to have characteristic singularities near the edges and corners of Ω'. In Section 4.3, we establish the minimal regularity theory we later require. We only use elementary arguments and express the regularity by pointwise estimates in Theorem 4.1. In Section 4.4, we introduce the Galerkin ansatz. It is based on a regular triangulation $\mathcal{T}_h$ of Ω'. The ansatz functions for σ are piecewise constant. If

σ did not have singularities, the error ϵ in the Galerkin method would scale like $h^{3/2}$, where h denotes the maximal diameter of the triangles. Here and in the sequel, the discretization error ϵ is measured in terms of the energy norm, which is the natural norm in this context of micromagnetics. Because of the singularities of σ, the order $3/2$ can only be preserved under a particular, but a–priori known refinement of $\mathcal{T}_h$ towards the edges. We characterize this refinement of $\mathcal{T}_h$ by an exponent α. In Theorem 4.2, we give an error estimate in terms of the diameter h of the triangles in the bulk. Naturally, it depends on α and yields the optimal scaling $h^{3/2}$ provided $\alpha > 2/3$. This estimate of the discretization error ϵ in the energy norm reduces to an estimate of the approximation error and is based on the regularity theory from Section 4.3. The corner singularities do not affect the scaling.

This impact of the singularities in the Dirichlet screen problem is known on meshes which are anisotropically graded towards an edge, see [22, 52]. However, in view of the succeeding computations including magnetizations m', we are restricted to *isotropically* refined triangulations $\mathcal{T}_h$, to which our regularity results adopt. In Section 4.5, we explain in detail the numerical generation of these a–priori refined triangulations.

In Section 4.6, we investigate how to numerically solve the discrete linear system for σ derived on such triangulations. It amounts to solving a linear problem of the form $K\,z + b = 0$. The non–sparse matrix K comes from the convolution operator with the single layer potential. Since K turns out to be symmetric positive definite, we can employ the conjugate gradient method for the solution of $K\,z + b = 0$. In every step of the conjugate gradient method, a matrix vector multiplication with K has to be carried out. On Cartesian meshes $\mathcal{Q}_h$, the operator K preserves the convolution structure. Hence the matrix vector multiplication can be efficiently carried out with help of the Fast Fourier Transform (FFT). We recall complexity results of the FFT, which is known to be of order $\mathcal{O}(N \log N)$ in the number N of triangles.

In Section 4.8, we give a brief introduction into the alternative method of $\mathcal{H}^2$–matrices [31]. It employs an approximation of K based on a hierarchical organization of the data structure. It is applicable not only on Cartesian meshes $\mathcal{Q}_h$, but also to above locally refined triangulations $\mathcal{T}_h$. We restrict ourselves to our special setup. We discuss its complexity, which roughly speaking is $\mathcal{O}(N)$.

In Section 4.9, we compare the performance of the FFT–method on $\mathcal{Q}_h$–type triangulations with that of the $\mathcal{H}^2$–matrices for the optimally refined triangulation $\mathcal{T}_h$. We compare the methods in terms of the discretization error $\epsilon > 0$ in the energy norm, which we use as a stopping criterion in the conjugate gradient method. We measure the CPU time, excluding the setup time (which is substantial for $\mathcal{H}^2$–matrices). We find that the $\mathcal{H}^2$–matrices beat FFT if one imposes an error tolerance of 5 percent or less. Moreover, the comparison to FFT allows for a "tuning of parameters" in the $\mathcal{H}^2$–matrix method, on which we rely in the succeeding numerical simulations.

Starting with Section 5.1, we turn from mere stray field computation to the determination of energy minimizing magnetizations with active constraint $|m'| \leq 1$,

which falls into the broad class of convex programming problems. We address the numerical solution to this problem by an *interior point method*: the micromagnetic energy $E(m')$ of the reduced model is replaced by a composite function $E_t(m') = E(m') + tB(m')$, $t > 0$, where the logarithmic barrier B models the convex constraint $|m'| \leq 1$. In case of our conformal finite elements m'_h, the Hessian $\mathrm{Hess}E_t(m'_h)$ is positive definite and there exists a unique minimizer $m'_h(t)$ to E_t for each $t > 0$, which defines the so–called *primal path*. This is the content of Sections 5.1 up to 5.4.

Though the reduced micromagnetic energy E is degenerate in the sense that infinitely many minimizers m' exist, the primal path converges to a unique, well–characterized minimizer m^*_h, the so–called *analytic center* of the optimality region: we apply a recent result from convex programming, [41], and give a brief introduction to this concept in Section 5.5. The notion of analytic centers finds a notable illustration by our micromagnetic simulations: for sufficiently weak external field we have $|m^*_h| < 1$ strictly, whereas for stronger fields the analytic center m^*_h is close to unit length in those regions where the external field penetrates the sample, see Sections 5.6 and 5.11.

For fixed $t > 0$, we compute the minimizer $m'_h(t)$ of E_t by Newton's method. It then serves as an initial guess for the minimizer of $E_{t'}$, where $t' < t$. The barrier parameter t is decreased until a suitable approximation to the analytic center m^*_h is attained. Within Newton's method, we apply an inexact Newton step with linesearch, and the Hessian of E_t is inverted by the conjugate gradient method, where the non–sparse stray field matrix K is compressed to an $\mathcal{H}^2$–matrix. This ansatz, outlined in detail in Sections 5.7 up to 5.10, leads to the formal algorithm and corresponding numerical results that we present and comment on in Section 5.11.

Starting with Section 6.1, we consider how to construct minimizers m' close to unit length: these correspond to saturated magnetizations observed in physical experiments. Indeed, for any magnetization satisfying the convex constraint $|m^*| \leq 1$, there exist many regular m' of unit length with the same charge density: $\nabla' \cdot m' = \nabla' \cdot m^*$. We may write $m' = \nabla^\perp \psi + m^*$, and the continuous function $\psi(x')$ on Ω' solves the boundary value problem

$$|\nabla^\perp \psi + m^*| \;=\; 1 \text{ in } \Omega', \quad \psi \;=\; 0 \text{ on } \partial\Omega' \;.$$

We choose the viscosity solution to this problem, which appears to single out a minimizer of unit length with as few walls as possible. We apply well–established numerical schemes provided for Cartesian grids as well as regular triangulations briefly recalled in Sections 6.3 and 6.4. In the Cartesian case we apply a scheme originally developed for solving numerically the shape–from–shading problem. On general triangulations we apply a two–step algorithm: the first part is based on a scheme approximating viscosity solutions as introduced in [6], and is followed by a postprocessing step that adjusts the length of the resulting magnetization. To reduce grid effects, the transition to an alternative refined triangulation turns out to

be beneficial: in terms of discrete de Rham complexes, the resulting magnetization may not be a minimizer on the underlying triangulation, but it is of the same energy as the analytic center m_h^*. We confront our numerical simulations with pictures from physical experiments, kindly provided by R. Schäfer and first published in [17].

2 Fractional Order Sobolev Spaces

This section summarizes results on fractional order Sobolev spaces and their relation to the single layer potential in [12] and [9, Chapter III.1]. We present the statements without proof.

2.1 The Spaces H^s for $|s| \leq 1$

For $0 \leq s \leq 1$ and $n \in \{2, 3\}$ we define the Sobolev spaces $H^s = H^s(\mathbb{R}^n)$ via the Fourier transform: a square integrabel function $f \in L^2(\mathbb{R}^n)$ is said to be in $H^s(\mathbb{R}^n)$ if and only if

$$||f||_{H^s}^2 \ := \ \int_{\mathbb{R}^n} (1 + |k|^2)^{s/2} \ |\widehat{f}(k)|^2 \ dk \ < \ +\infty \ , \tag{2.1}$$

where $\widehat{f}$ denotes the Fourier transform of f.

Whenever we make use of the short hand notation H^s instead of $H^s(\mathbb{R}^n)$, it will be clear from the context if the space $H^s(\mathbb{R}^2)$ or the space $H^s(\mathbb{R}^3)$ is under consideration.

For $s = 0$, the space $H^s(\mathbb{R}^n)$ coincides with $L^2(\mathbb{R}^n)$, the Hilbert space of square integrable functions on $\mathbb{R}^n$. For $s = 1$, the norm (2.1) may be replaced by the more common definition of the H^1–norm,

$$||f||_{H^1}^2 \ = \ ||f||_{L^2}^2 + ||\nabla f||_{L^2}^2 \ ,$$

where the gradient ∇ is to be understood in the distributional sense. The Sobolev space $H^1(\mathbb{R}^n)$ is a Hilbert space with scalar product

$$\langle f, g \rangle_{H^1} \ := \ \int_{\mathbb{R}^n} f(x) \ g(x) \ dx \ + \int_{\mathbb{R}^n} \nabla f(x) \cdot \nabla g(x) \ dx \tag{2.2}$$

for all $f, g \in H^1(\mathbb{R}^n)$. For a fixed Lipschitz domain $\Omega \subset \mathbb{R}^n$ we define H_0^1 as the completion w. r. t. (2.1) of the space of smooth functions that vanish on the complement $\mathbb{R}^n - \Omega$.

For $0 < s \leq 1$ the space of distributions H^{-s} is defined as the dual space of H^s. Here the duality pairing $\langle . \ , . \rangle : H^s \times H^{-s} \mapsto \mathbb{R}$ is given by the continuous extension of the standard scalar product in L^2. Therefore, we write formally

$$\langle f, g \rangle \ = \ \int_{\mathbb{R}^n} f(x) \ g(x) \ dx$$

for $f \in H^s$ and $g \in H^{-s}$.

Remark 2.1. *We are especially interested in the case $s = \frac{1}{2}$, $n = 2$. To avoid any misinterpretations due to the ambiguous use of two– and three–dimensional variables*

in the following, a prime will indicate a two–dimensional variable. In particular, we use the notation

$$x \;=\; (x', x_3)$$

with $x' \in \mathbb{R}^2$ *and* $x_3 \in \mathbb{R}$ *for any* $x \in \mathbb{R}^3$. *The corresponding two–dimensional gradient is denoted by* ∇'.

The norm on $H^{-1/2} = H^{-1/2}(\mathbb{R}^2)$ can be written as

$$||\sigma||_{H^{-1/2}} \;=\; \sup_{f \in H^{1/2}} \frac{\langle f, \sigma \rangle}{||f||_{H^{1/2}}}$$

for every $\sigma \in H^{-1/2}(\mathbb{R}^2)$. An equivalent norm on $H^{-1/2} = H^{-1/2}(\mathbb{R}^2)$ is given by

$$\left(\int_{\mathbb{R}^2} |(\nabla')^{-1/2} \sigma|^2 \, dx' \right)^{1/2} \;:=\; \left(\int_{\mathbb{R}^2} |k'|^{-1} |\widehat{\sigma}(k')|^2 \, dk' \right)^{1/2} , \tag{2.3}$$

where $\widehat{\sigma}$ denotes the Fourier transform of the tempered distribution σ.

2.2 The Single Layer Potential

The expression (2.3) is closely related to the *single layer potential* $1/r$. The single layer potential defines a bijective and continuous linear operator

$$V \;:\; H^{s-1}(\mathbb{R}^2) \to H^s(\mathbb{R}^2), \qquad V\sigma(x') \;:=\; \int_{\mathbb{R}^2} \frac{\sigma(y')}{4\pi \, |x' - y'|} \, dy' \tag{2.4}$$

for any $0 \leq s \leq 1$ and $\sigma \in H^{s-1}(\mathbb{R}^2)$. For $s = \frac{1}{2}$, the operator V is strongly elliptic, i. e. there exists a constant $C > 0$ such that

$$\langle V\sigma, \sigma \rangle \;\geq\; C ||\sigma||^2_{H^{-1/2}}$$

for all $\sigma \in H^{-1/2}(\mathbb{R}^2)$. In particular, the bilinear form $\langle V \cdot \, , \cdot \rangle$ defines a scalar product on the Hilbert space $H^{-1/2}(\mathbb{R}^2)$ with corresponding norm

$$||\sigma||_V \;:=\; \sqrt{\langle V\sigma, \sigma \rangle} \; . \tag{2.5}$$

As a result of the Lax–Milgram theorem, for any $f \in H^{1/2}(\mathbb{R}^2)$ there exists a unique $\sigma \in H^{-1/2}(\mathbb{R}^2)$ with $V\sigma = f$. Moreover, it turns out that (2.3) equals (2.5) up to a constant factor, i. e.

$$\tfrac{1}{2} \int_{\mathbb{R}^2} |(\nabla')^{-1/2} \sigma|^2 dx' \;=\; \int_{\mathbb{R}^2} \int_{\mathbb{R}^2} \sigma(x') \, \frac{1}{4\pi \, |x' - y'|} \, \sigma(y') \, dy' \, dx'. \tag{2.6}$$

It is well–known (see e. g. [27, Chapter 8]) that (2.3) can also be expressed as a three–dimensional Dirichlet integral

$$\tfrac{1}{2} \int_{\mathbb{R}^2} |(\nabla')^{-1/2} \sigma|^2 \, dx' \;=\; \int_{\mathbb{R}^3} |\nabla u|^2 \, dx \; ,$$

where the potential $u \in H^1(\mathbb{R}^3) \cap C^0(\mathbb{R}^3)$ is determined by

$$\left.\begin{array}{rcll} -\Delta u & = & 0 & \text{in } \mathbb{R}^3 - (\Omega' \times \{0\}) \ , \\ \partial_3 u(x',0+) - \partial_3 u(x',0-) & = & \sigma(x') & \text{for } x' \in \Omega' \ . \end{array}\right\} \tag{2.7}$$

Here the one–sided derivatives are defined as

$$\partial_3 u(x',0\pm) \ := \ \lim_{x_3 \to \pm 0} \partial_3 u(x',x_3) \ .$$

Solving equation (2.7) for any $\sigma \in H^{-1/2}(\mathbb{R}^2)$ in Fourier space establishes indeed the relation

$$\int_{\mathbb{R}^3} |\nabla u|^2 \ dx \ = \ \tfrac{1}{2} \int_{\mathbb{R}^2} |k'|^{-1} |\widehat{\sigma}(k')|^2 \ dk' \ .$$

Last but not least, (2.3) can be written as a dual norm

$$\left(\tfrac{1}{2} \int_{\mathbb{R}^2} |(\nabla')^{-1/2} \sigma|^2 dx' \right)^{1/2} \ = \ \sup \left\{ \frac{\int_{\mathbb{R}^2} \sigma \, u \, dx'}{(\int_{\mathbb{R}^3} |\nabla u|^2 dx)^{1/2}} \mid u \colon \mathbb{R}^3 \to \mathbb{R} \right\}, \tag{2.8}$$

resp.

$$\begin{aligned} & \tfrac{1}{2} \int_{\mathbb{R}^2} |(\nabla')^{-1/2} \sigma|^2 dx' \\ & \quad = \ \sup \left\{ - \int_{\mathbb{R}^3} |\nabla u|^2 dx - 2 \int_{\mathbb{R}^2} \sigma \, u \, dx' \mid u \colon \mathbb{R}^3 \to \mathbb{R} \right\}. \end{aligned} \tag{2.9}$$

2.3 The Spaces $H^s(\nabla \cdot)$

We also need subspaces of $(L^2(\mathbb{R}^n))^2$ for which the divergence $\nabla \cdot$ is a well–defined operator with values in $H^s(\mathbb{R}^n)$. This leads for $0 \le s \le 1$ to the definition of the Sobolev spaces

$$H^s(\nabla \cdot) \ := \ \{ \, f \in (L^2(\mathbb{R}^n))^2 \mid \nabla \cdot f \in H^{s-1}(\mathbb{R}^n) \, \} \ , \tag{2.10}$$

with the norm

$$||f||^2_{H^s(\nabla \cdot)} \ := \ \int_{\mathbb{R}^n} f \cdot f \ dx \ + ||\nabla \cdot f||^2_{H^{s-1}} \ . \tag{2.11}$$

In view of (2.2), the space $H^1(\nabla \cdot)$ is a Hilbert space with scalar product

$$\langle f, g \rangle_{H^1(\nabla \cdot)} \ := \ \int_{\mathbb{R}^n} f \cdot g \ dx \ + \int_{\mathbb{R}^n} \nabla \cdot f \ \nabla \cdot g \ dx$$

for all $f, g \in H^1(\nabla \cdot)$.

To point out the special case $n = 2$ we again use the notation $H^s(\nabla' \cdot)$ introduced in Remark 2.1. For $s = \frac{1}{2}$ an equivalent norm on $H^{1/2}(\nabla' \cdot)$ is given by

$$||f||^2_{H^{1/2}(\nabla' \cdot)} \ := \ \int_{\mathbb{R}^2} f \cdot f \ dx' + ||\nabla' \cdot f||^2_V \ ,$$

where the V–norm is defined due to (2.5). The space $H^{1/2}(\nabla'\cdot)$ may be viewed as a Hilbert space with scalar product

$$\langle f, g \rangle_{H^{1/2}(\nabla'\cdot)} \ := \ \int_{\mathbb{R}^n} f \cdot g \ dx \ + \langle V \nabla'\cdot f, \nabla'\cdot g \rangle$$

for all $f, g \in H^{1/2}(\nabla'\cdot)$. We note that the space $H^1(\nabla'\cdot)$ is a subset of $H^{1/2}(\nabla'\cdot)$ by the inclusion

$$H^1(\nabla'\cdot) \ \hookrightarrow \ H^{1/2}(\nabla'\cdot) \ .$$

By combining the operators V and $\nabla'\cdot$ we may also construct a semi–scalar product on $H^{1/2}(\nabla'\cdot)$ as

$$\langle V \nabla'\cdot f, \nabla'\cdot g \rangle \tag{2.12}$$

for all $f, g \in H^{1/2}(\nabla'\cdot)$. This semi–scalar product becomes indeed a scalar product on the quotient space

$$H^{1/2}(\nabla'\cdot) \ / \ \{ \, f \in H^{1/2}(\nabla'\cdot) \mid \nabla'\cdot f \equiv 0 \, \} \ .$$

Remark 2.2. *For any function space H on which the divergence $\nabla\cdot$ is a well–defined linear operator, we introduce the quotient space*

$$H \ / \ \mathrm{Ker}(\nabla\cdot) \ := \ H \ / \ \{ \, f \in H \mid \nabla\cdot f \equiv 0 \, \} \ .$$

For a fixed Lipschitz domain $\Omega \subset \mathbb{R}^n$ we define the space $H_0^1(\nabla\cdot)$ as the completion w. r. t. (2.11) of the space of n–dimensional smooth vector fields with vanishing normal component on the boundary $\partial\Omega$. In particular, Green's formula implies

$$\int_\Omega g \ \nabla\cdot f \ dx \ \ = \ - \int_\Omega f \cdot \nabla g \ dx$$

for all $f \in H_0^1(\nabla\cdot)$ and $g \in H^1$. Thus we consider fields in $H_0^1(\nabla\cdot)$ as being set to zero outside Ω.

3 Conformal Approximation of a Reduced 2–d Model

3.1 A Reduced Model for Thin–Film Micromagnetics

In [16], a reduced 2–d model for a thin–film ferromagnetic element under external field was derived. The thin ferromagnetic sample is described by its cross section $\Omega' \subset \mathbb{R}^2$.

Here and in the following pages the prime denotes the projection on the in–plane components, see Remark 2.1.

In the reduced 2–d model, the magnetization m is in–plane, i. e. $m = m'$, and constant in the thickness direction, i. e. $m' = m'(x')$ for $x' \in \Omega'$. Hence $m' \colon \Omega' \to \mathbb{R}^2$ is a 2–d vector field. Appropriately non–dimensionalized, the reduced energy takes the form

$$E(m') \;=\; \int_{\mathbb{R}^3} |\nabla u|^2 dx - 2 \int_{\Omega'} m' \cdot H'_{ext}\, dx'. \tag{3.1}$$

Here H'_{ext} denotes the in–plane external field and $-\nabla u$ is the stray field. For simplicity, we assume H'_{ext} to be constant in $\mathbb{R}^3$. The stray field potential $u \colon \mathbb{R}^3 \to \mathbb{R}$ is generated by the "magnetic charges": $\sigma = -\nabla' \cdot m'$ on Ω' and $\nu' \cdot m'$ along $\partial\Omega'$. This can be formulated distributionally:

$$\int_{\mathbb{R}^3} \nabla u \cdot \nabla \zeta \, dx \;=\; \int_{\Omega'} m'(x') \cdot \nabla' \zeta(x', 0)\, dx' \quad \text{for all test functions } \zeta \colon \mathbb{R}^3 \to \mathbb{R}\ ,$$

which in turn is equivalent to the "classical" formulation (2.7). In particular, the stray field energy can be expressed in terms of the Fourier transform $\hat{\sigma}$ of σ (which for this purpose we extend trivially on $\mathbb{R}^2$):

$$\int_{\mathbb{R}^3} |\nabla u|^2 \, dx \;=\; \tfrac{1}{2} \int_{\mathbb{R}^2} |k'|^{-1} |\hat{\sigma}(k')|^2 \, dk'.$$

According to Section 2, we interpret this expression as a (squared) $H^{-1/2}(\mathbb{R}^2)$–norm of σ:

$$\int_{\mathbb{R}^2} |k'|^{-1} |\hat{\sigma}(k')|^2 \, dk' \;=\; \int_{\mathbb{R}^2} |(\nabla')^{-1/2} \sigma|^2 \, dx'. \tag{3.2}$$

As the exchange energy is neglected, the saturation constraint $|m'|^2 = 1$ relaxes to its convexification

$$|m'|^2 \;\le\; 1. \tag{3.3}$$

This reduced model generalizes an ad hoc model proposed in [10]. Notice that the reduced model embodies the competition between stray field energy and the effect of the external field. The Zeeman term $\int_{\Omega'} m' \cdot H'_{ext}\, dx'$ favors alignment, the stray field favors pole avoidance. In particular, a finite stray field energy imposes that m' is tangential to $\partial\Omega'$, i. e. we have

$$\nu' \cdot m' \;=\; 0 \quad \text{on } \partial\Omega' \text{ almost everywhere.} \tag{3.4}$$

The space of admissible magnetizations m' is thus defined as

$$\mathcal{A} := \{ m' \in H^{1/2}(\nabla'\cdot) \mid m' = 0 \text{ on } \mathbb{R}^2 - \Omega',\ m' \cdot \nu' = 0 \text{ on } \partial\Omega',\ |m'| \leq 1 \text{ on } \Omega' \} .$$

Assuming that stable magnetizations are modeled by local minimizers of the micromagnetic energy, we are led to the convex variational problem:

$$\text{Minimize } E(m') \text{ among all } m' \in \mathcal{A} . \tag{3.5}$$

We notice that E depends on m' only via σ. Indeed, (3.4) implies that the second term in (3.1) can be reformulated as

$$+2 \int_{\Omega'} \sigma\, H'_{ext} \cdot x'\, dx'.$$

Hence the reduced energy may be rewritten as

$$E(\sigma) \ = \ \tfrac{1}{2} \int_{\mathbb{R}^2} |(\nabla')^{-1/2}\sigma|^2\, dx' + 2 \int_{\Omega'} \sigma\, H'_{ext} \cdot x'\, dx'. \tag{3.6}$$

The reduced problem is therefore highly degenerate: in general, there exists an infinite number of minimizers m'. Nevertheless, some of the minimizers' quantities are determined uniquely: the in–plane divergence $\nabla' \cdot m'$ and the stray field potential $u \in H^1(\mathbb{R}^3) \cap C^0(\mathbb{R}^3)$.

The situation is more subtle with regard to m' itself: the Euler–Lagrange equation of the reduced problem is given by

$$\left.\begin{array}{rcl} -\nabla' u + H'_{ext} & = & \lambda m' \\ \lambda(|m'| - 1) & = & 0 \end{array}\right\} \quad \text{in } \Omega' ,$$

where $\lambda(x') \geq 0$ is the Lagrange multiplier related to (3.3). For sufficiently weak external field H'_{ext}, the constraint (3.3) is not active leading to $\lambda \equiv 0$. Hence in this case, the magnetization adjusts itself such that the stray field $-\nabla' u$ compensates the external field H'_{ext} in Ω'. This magnetization m' is not unique. For sufficiently strong external field H'_{ext}, the constraint (3.3) becomes active and $m'(x')$ is indeed unique on the penetrated region, i. e. the subregion of Ω' where $\lambda(x') > 0$.

First numerical simulations of the reduced model based on finite differences and its comparison to subsequently carried out experiments have been published in [17].

The 2–d model considered here is closely related to a macroscopic model for stationary micromagnetics, where the large–body limit is derived in [15] by Γ–convergence. Numerical simulations for this model are carried out in [11]: for 2–d computations the single layer potential in (2.4) is replaced by the 2–d Newtonian kernel $-\log|x|$, which yields $\nabla' u \in L^2(\mathbb{R}^2)$. The numerical analysis of [11], which offers L^2–a–priori and a–posteriori error estimates, is not applicable to the reduced model considered here: due to [16] we have only $\nabla' u \in L^4_{loc}(\Omega')$ for the stray field.

However, simulations and experimental observations are in good agreement in the regime of sufficiently thick films where the wall type is the asymmetric Bloch wall, see Section 6. In thinner films, the repulsion of the Néel wall from the sample edge leads to some deviations with respect to wall expulsion.

3.2 Conforming Elements in $\mathbb{R}^2$

We suppress all primes for the two–dimensional variables in the following sections dealing with the definition of finite elements.

For the approximation of $\mathcal{A}$ we choose a conforming method, which means that we aim at an internal approximation of the function space $H^{1/2}(\nabla\cdot)$ by a finite dimensional subspace.

Since finite element methods require naturally a minimal regularity of L^2 for all the functions involved, we consider here conforming approximations of the subspace $H^1(\nabla\cdot) \subset H^{1/2}(\nabla\cdot)$. The finite element spaces we introduce are therefore not asymptotically dense in $H^{1/2}(\nabla\cdot)$, but we circumvent the approximation of functions that exist only in a distributional sense.

Raviart and Thomas introduced in [47] lowest–order conforming finite elements in $H^1(\nabla\cdot)$ for the two–dimensional case. These elements are nowadays called *Raviart–Thomas elements*.

Due to [8, Chapter 3], there are three main ingredients in the definition of a finite element space:

- First, a simplicial triangulation of the computational domain has to be constructed.
- Second, for each element of the triangulation a space of polynomials has to be provided.
- Finally, a set of global degrees of freedom, which characterize uniquely a finite element function, must be defined.

3.3 Regular Triangulations

We suppose that the domain $\Omega \subset \mathbb{R}^2$ has a polygonal boundary $\partial\Omega$ and is covered by a regular triangulation $\mathcal{T}$. Therefore $\mathcal{T}$ is a partition of Ω into closed, non–overlapping triangles such that every vertex of a triangle is a vertex of all adjacent triangles. In particular, there are no "hanging nodes". For the closure of the domain Ω we have

$$\overline{\Omega} \;=\; \bigcup_{T\in\mathcal{T}} T \;,$$

and the intersection of two distinct triangles is either empty, a vertex or an edge. We abbreviate the set of all edges of the triangulation by $\mathcal{E}$ and the set of all vertices by $\mathcal{V}$.

We have to settle the issue of edges' orientation. For each edge $e \in \mathcal{E}$ of the triangulation $\mathcal{T}$ we assume a unique ordering of its endpoints $a_0, a_1 \in e$. This induces a unique normal ν on e by setting

$$\nu \;=\; \frac{1}{|e|}(a_0 - a_1)^\perp \;\;=\;\; \frac{1}{|a_0 - a_1|}(a_0 - a_1)^\perp \;. \tag{3.7}$$

For a fixed edge e we denote the neighboring triangles by T^+ and T^-, such that ν points from T^+ into T^-.

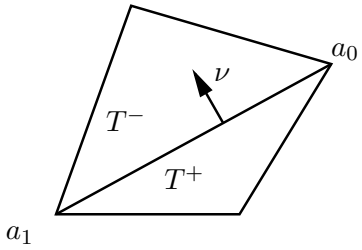

Figure 3.1: Implicit orientation of an edge by ordering its endpoints.

For any vector field $f \in (L^2(\Omega))^2$ and any edge $e \in \mathcal{E}$ with neighboring triangles T^+ and T^-, let $[f]_e$ denote the jump of f across the edge e, i. e.

$$[f]_e(x) \;=\; f|_{T^+}(x) - f|_{T^-}(x) \quad \text{for almost every} \;\; x \in e \;.$$

3.4 The Triangulations $\mathcal{Q}_h$ and $\mathcal{T}_h$

In the case of a rectangular sample Ω we consider two more specific types of triangulations: we start with a Cartesian grid divided into upper and lower triangles as shown in Figure 3.2. The resulting triangulation consists therefore of isosceles right triangles of equal size. For any triangle the two legs have length h, and the hypotenuse has length $h\sqrt{2}$. We denote this class of triangulations by $\mathcal{Q}_h$.

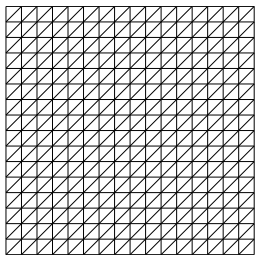

Figure 3.2: Example for a triangulation of class $\mathcal{Q}_h$ on the unit square with $h = 1/16$.

On a triangle $T \in \mathcal{Q}_h$ marked for refinement we apply the standard *red refinement* strategy: we split T into four subtriangles of equal size and equal shape by bisection of each edge, see Figure 3.3. Since a new node appears on each midside, an additional splitting of the neighboring triangles is necessary to avoid hanging nodes. We use the scheme in [49, Chapter 1.1] for this purpose, which terminates after finitely many steps. This results in a triangulation that consists only of isosceles right triangles,

in general of different size. We denote these triangulations by $\mathcal{T}_h$. A typical example is given in Figure 3.4. Obviously, the family of triangulations $\mathcal{Q}_h$ is a subclass of $\mathcal{T}_h$.

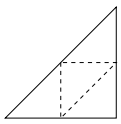

Figure 3.3: Red refinement: the dashed line indicates the splitting of a marked triangle into four subtriangles.

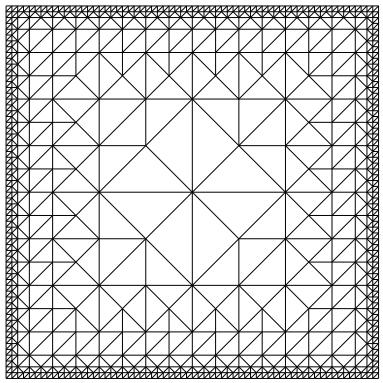

Figure 3.4: Example for a triangulation of class $\mathcal{T}_h$ on the unit square with $h = 1/4$ and refinement levels $0 \le k \le 8$.

A triangle $T \in \mathcal{T}_h$ is said to be of refinement level k if the two legs are of length

$$h\,2^{-k}\ . \tag{3.8}$$

The inradius r_T is then given by

$$r_T \ = \ \tfrac{1}{2}(2-\sqrt{2})h\,2^{-k}\ .$$

The diameter $\mathrm{diam}(T)$ is just the length of the hypotenuse,

$$\mathrm{diam}(T) \ = \ h\,2^{-k+1/2}\ ,$$

and the area equals

$$|T| \ = \ h^2\,2^{-2k-1}\ .$$

The family of triangulations $\mathcal{T}_h$ is quasiuniform in the sense of [7, Chapter II.5], since for every triangle $T \in \mathcal{T}_h$ there holds $Cr_T \ge \mathrm{diam}(T)$ with a universal constant $C > 0$.

3.5 H^1–Conforming Elements in $\mathbb{R}^2$

As a conforming finite element approximation of the space H^1 we choose the subspace of continuous functions which are piecewise affine: for a given triangle $T \in \mathcal{T}_h$ the local trial space $P^1(T)$ is just the space of all polynomials on T up to degree one. Each $p \in P^1(T)$ is uniquely defined by its values in the vertices of T, which are thus chosen as degrees of freedom. The finite element space P_h^1 is then defined as the space of continuous functions on Ω which are of type P^1 if restricted to any triangle $T \in \mathcal{T}_h$.

For any $f \in H^1$ the corresponding interpolation operator Π_h^v is given by the evaluation of f at the vertices of the triangulation and succeeding linear interpolation: $\Pi_h^v f \in P_h^1$ is the uniquely defined function that fulfills

$$(\Pi_h^v f)(x_0) \;=\; f(x_0)$$

for any vertex x_0 of the triangulation $\mathcal{T}_h$. A corresponding finite element approximation of H_0^1 is given by

$$P_{0,h}^1 \;:=\; \{\, \phi_h \in P_h^1 \mid \phi_h|_{\partial\Omega} \equiv 0 \,\} \;.$$

The gradient of $\phi_h \in P_h^1$ is a well–defined L^2–function which is constant on any given triangle $T \in \mathcal{T}_h$. Thus we may consider $\nabla\phi_h$ as an element of the space P_h^0, the space of piecewise constant functions on $\mathcal{T}_h$. The corresponding interpolation operator $\Pi_h^t : L^2 \to P_h^0$ is defined via the identity

$$\int_T \Pi_h^t \sigma \; dx \;=\; \int_T \sigma \; dx$$

for all $T \in \mathcal{T}_h$ and $\sigma \in L^2$. The subspace L_0^2 is defined as the space of L^2–functions with zero average on Ω, i. e. we have $\int_\Omega \sigma \; dx = 0$ for all $\sigma \in L_0^2$. Implicitely, we set $\sigma \equiv 0$ in the complement $\mathbb{R}^2 - \Omega$. The corresponding subspace of P_h^0 is denoted by $P_{0,h}^0$.

3.6 The Raviart–Thomas Element

3.6.1 Local Trial Space

For a given triangle $T \in \mathcal{T}_h$ with vertices a_i, $i = 1, 2, 3$, and corresponding edges e_i, such that a_i faces e_i for every $i = 1, 2, 3$, the local trial space is given by

$$RT(T) = \{\, T \ni x \mapsto c + \beta x \mid c \in \mathbb{R}^2, \beta \in \mathbb{R} \;\} \;. \tag{3.9}$$

The special choice of the ansatz function in (3.9) ensures that for $m_T \in RT(T)$ the normal component is constant along any line segment $[x_0, x_1]$ that lies entirely in the triangle T. Indeed, let $x_0, x_1 \in T$ and $0 \le \lambda \le 1$ be given, then we have for $\nu = (x_1 - x_0)^\perp$:

$$\begin{aligned} m_T(\lambda x_1 + (1-\lambda)x_0) \cdot \nu &= (c + \beta(\lambda x_1 + (1-\lambda)x_0)) \cdot \nu \\ &= c \cdot \nu + \lambda\beta(x_1 - x_0) \cdot \nu + \beta x_0 \cdot \nu \;, \end{aligned}$$

and with $(x_1 - x_0)\cdot\nu = 0$ it follows that $m_T(\lambda x_1 + (1-\lambda)x_0)\cdot\nu$ is independent of λ. In particular, the normal component of m_T is constant along the edges of T. The following properties of the local trial space will be useful later.

In the local representation $m_T(x) = c + \beta x$ the divergence of m_T on T is given by

$$\nabla\cdot m_T \;=\; 2\beta \;. \tag{3.10}$$

Thus $\frac{1}{2}\nabla\cdot m_T$ can be interpreted as a Lipschitz constant of the local vector field m_T on T : for $x_0, x_1 \in T$ we have

$$|m_T(x_0) - m_T(x_1)| \;=\; \tfrac{1}{2}|\nabla\cdot m_T|\,|x_0 - x_1| \;. \tag{3.11}$$

The following simple estimates will be useful later.

Lemma 3.1. *Let $m_T \in RT(T)$ and $x_0 \in T$ be given. If there are constants $C_0, C_1 \geq 0$ such that*

$$|m_T(x_0)| \;\leq\; C_0 \quad \textit{and} \quad |\nabla\cdot m_T| \;\leq\; C_1 \;, \tag{3.12}$$

then we have the estimate

$$\sup_{x\in T} |m_T(x)|^2 \;\leq\; \tfrac{1}{2}C_1^2\,\mathrm{diam}(T)^2 + 2\,C_0^2 \;. \tag{3.13}$$

Proof of Lemma 3.1.
For any $x_1 \in T$ we have by the assumptions (3.12)

$$\begin{aligned} |m_T(x_1)|^2 &\leq 2\,|m_T(x_1) - m_T(x_0)|^2 + 2\,|m_T(x_0)|^2 \\ &\leq \tfrac{1}{2}|\nabla\cdot m_T|^2\,|x_1 - x_0|^2 + 2\,C_0^2 \\ &\leq \tfrac{1}{2}C_1^2\,\mathrm{diam}(T)^2 + 2\,C_0^2 \;, \end{aligned}$$

which proves (3.13). □

Lemma 3.2. *Let $m_T \in RT(T)$ be given. If there exists a constant $C_0 \geq 0$ such that*

$$|m_T(x)| \;\leq\; C_0 \quad \textit{for all } x \in T \;,$$

then we have the estimate

$$|\nabla\cdot m_T| \;\leq\; \frac{4\,C_0}{\mathrm{diam}(T)} \;.$$

Proof of Lemma 3.2.
Let $x_0, x_1 \in T$ be given such that $\mathrm{diam}(T) = |x_0 - x_1|$. Then we have

$$|m_T(x_1) - m_T(x_0)| \;\leq\; 2\,C_0 \;,$$

and with (3.11) therefore

$$|\nabla\cdot m_T| \;\leq\; \frac{4\,C_0}{|x_1 - x_0|} \;.$$

□

3.6.2 Degrees of Freedom

Following [47], the degrees of freedom for $m_T \in RT(T)$ are given by the edge fluxes

$$\gamma_i(m_T) = \int_{e_i} m_T \cdot \nu_i \; ds \; , \quad i = 1, 2, 3 \; , \tag{3.14}$$

which can be equivalently written as

$$\gamma_i(m_T) = (m_T(x) \cdot \nu_i) \, |e_i|$$

for any $x \in e_i$, since the normal component of m_T is constant on each given edge e_i. It is easily checked that with $m_T^{(i)}(x) := (x - a_i)$, $i = 1, 2, 3$, we have $\gamma_i(m_T^{(i)}) \neq 0$ and $\gamma_j(m_T^{(i)}) = 0$ for $j \neq i$. So the linear forms γ_i, $i = 1, 2, 3$ are linearly independent as elements of the dual space $(RT(T))'$, and thus form a basis of the three–dimensional space $(RT(T))'$.

The finite element space RT_h is now defined as the space of vector fields which are locally of type $RT(T)$ and have continuous normal components along edges, i. e.

$$RT_h \; = \; \{m_h \in (L^2(\Omega))^2 \mid \forall T \in \mathcal{T}_h, \; m_h|_T \in RT(T) \text{ and } \forall e \in \mathcal{E}_h, \; [m_h]_e \cdot \nu_e = 0\} \; . \tag{3.15}$$

This makes $\nabla \cdot m_h \in L^2(\Omega)$ a well–defined, piecewise constant function for each $m_h \in RT_h$, and thus we have $RT_h \subset H^1(\nabla\cdot)$. In view of (3.14) this means that for $m_h \in RT_h$ the degrees of freedom are unambiguously defined for each edge $e \in \mathcal{E}_h$. Since $\nabla \cdot m_h$ is piecewise constant on $\mathcal{T}_h$, we frequently use the notation $(\nabla \cdot m_h)(T)$ for the value of $\nabla \cdot m_h$ on $T \in \mathcal{T}_h$.

$RT_{0,h}$ is defined as the subspace of fields $m_h \in RT_h$ for which the normal component of m_h vanishes on $\partial\Omega$. Therefore $RT_{0,h} \subset H_0^1(\nabla\cdot)$.

3.6.3 Basis Functions

We now introduce a basis of RT_h that is dual to the basis of $(RT_h)'$ defined by the linear forms (3.14). The values of a finite element function $m_h \in RT_h$ are then uniquely determined by the values of its degrees of freedom (DOFs) and the values of the basis functions connected with these DOFs.

The canonical basis function $\varphi_h^{(i)}$ associated with a given edge e_i is defined for $x \in T^\pm$ by

$$\varphi_h^{(i)}(x) \; = \; \begin{cases} +\frac{1}{2|T^+|}(x - a_i^+) & \text{for } x \in T^+ \; , \\ -\frac{1}{2|T^-|}(x - a_i^-) & \text{for } x \in T^- \; , \end{cases}$$

and for $x \in \Omega - T^\pm$ by $\varphi_h^{(i)}(x) = 0$. Here $|T^\pm|$ denotes the area of the triangle $T^\pm$ and $a_i^\pm$ is the vertex of $T^\pm$ facing the edge e_i. In particular, we have $\text{supp}\varphi_h^{(i)} = T^+ \cup T^-$. For a point $x \in e_i$ the value $\pm(x - a_i^\pm) \cdot \nu_i$ is just the height $2|T^\pm|/|e_i|$ of the triangle $T^\pm$ and thus the edge flux

$$\int_{e_i} \varphi_h^{(i)} \cdot \nu_i \; ds \; = \; 1$$

is unambiguously defined. Moreover, if e_j is another edge of T^+ or T^-, i. e. $e_i \neq e_j$, then we have

$$\int_{e_j} \varphi_h^{(i)} \cdot \nu_j \; ds \; = \; 0 \; ,$$

since $(x - a_i)$ is tangential to e_j for $x \in e_j$ and thus the normal component $\varphi_h^{(i)} \cdot \nu_j$ vanishes on e_j.

In particular, we have $\varphi_h^{(i)} \in RT_h$, and the set of basis functions $\varphi_h^{(i)}, \; i = 1, .., \#\mathcal{E}_h$, is a set of linearly independent functions.

It remains to show that the set of basis functions $\{\varphi_h^{(i)}\}_{i=1,..,\#\mathcal{E}_h}$ indeed forms a basis of RT_h : for given $m_h \in RT(\mathcal{T}_h)$ define

$$p_h \; := \; m_h - \sum_{i=1}^{\#\mathcal{E}_h} \left(\int_{e_i} m_h \cdot \nu_i \; ds \right) \varphi_h^{(i)} \; .$$

Obviously $p_h \in RT_h$ and $p_h \cdot \nu_i = 0$ for all $i = 1, .., \#\mathcal{E}_h$ due to the definition of $\varphi_h^{(i)}$. Therefore $\nabla \cdot p_h = 0$ on all triangles $T \in \mathcal{T}_h$ and p_h is a piecewise constant vector field. But then the property $p_h \cdot \nu_i = 0$ for all $i = 1, .., \#\mathcal{E}_h$ implies that p_h vanishes identically.

The corresponding interpolation operator $\Pi_h^e : H^1(\nabla \cdot) \rightarrow RT_h$ is thus defined via the identity

$$\int_e (\Pi_h^e m) \cdot \nu \; ds \; = \; \int_e m \cdot \nu \; ds \tag{3.16}$$

for every edge $e \in \mathcal{E}_h$ and $m \in H^1(\nabla \cdot)$.

3.7 The Discrete De Rham Complex

We suppress all primes for the two–dimensional variables in this section.

$H^1(\nabla \cdot)$–conforming and H^1–conforming elements are related in terms of the *discrete de Rham complex*, which plays a paramount role in the theory of computational electromagnetism. For details and proofs we refer the reader to the survey article [35] and the references therein. Here we only state those results needed in the following for our discussion.

Presuming a minimal regularity of L^2 for all the functions involved, the de Rham complex in two space dimensions can be stated as

$$\mathbb{R} \; \stackrel{\subset}{\longrightarrow} \; H^1 \; \stackrel{\nabla^\perp}{\longrightarrow} \; H^1(\nabla \cdot) \; \stackrel{\nabla \cdot}{\longrightarrow} \; L^2 \; \longrightarrow \; 0 \; . \tag{3.17}$$

If the function spaces in (3.17) are restricted to a simply connected sample $\Omega \subset \mathbb{R}^2$, then the sequence is exact, i. e. the range of each map coincides with the kernel of the succeeding map. In particular, a field $f \in H^1(\nabla \cdot)$ is divergence–free if and only if there exists a function $\phi \in H^1$ such that

$$f \; = \; \nabla^\perp \phi \; . \tag{3.18}$$

Moreover, the map from $H^1(\nabla\cdot)$ to L^2 is surjective: for any $\sigma \in L^2$ there exists a field $f \in H^1(\nabla\cdot)$ such that

$$\sigma \;=\; \nabla\cdot f \;.$$

We may restrict (3.17) to fields and functions satisfying homogeneous Dirichlet boundary conditions in the sense of Section 3.5 and Section 3.6.2. The corresponding de Rham complex then reads:

$$0 \;\xrightarrow{\subset}\; H_0^1 \;\xrightarrow{\nabla^\perp}\; H_0^1(\nabla\cdot) \;\xrightarrow{\nabla\cdot}\; L_0^2 \;\longrightarrow\; 0 \;. \tag{3.19}$$

Given a regular triangulation $\mathcal{T}_h$ of Ω, a *discrete* de Rham complex in two space dimensions may be stated as

$$\mathbb{R} \;\xrightarrow{\subset}\; P_h^1 \;\xrightarrow{\nabla^\perp}\; RT_h \;\xrightarrow{\nabla\cdot}\; P_h^0 \;\longrightarrow\; 0 \tag{3.20}$$

or

$$0 \;\xrightarrow{\subset}\; P_{0,h}^1 \;\xrightarrow{\nabla^\perp}\; RT_{0,h} \;\xrightarrow{\nabla\cdot}\; P_{0,h}^0 \;\longrightarrow\; 0 \;, \tag{3.21}$$

respectively. The discrete de Rham complexes (3.20) and (3.21) may be considered as conforming finite element approximations to the complexes (3.17) and (3.19), respectively.

Referring to the interpolation operators in Section 3.5 and Section 3.6.3, the combination of (3.17) and (3.20) yields a commutative diagram:

$$\begin{array}{ccccc} H^1 & \xrightarrow{\nabla^\perp} & H^1(\nabla\cdot) & \xrightarrow{\nabla\cdot} & L^2 \\ \big\downarrow \Pi_h^v & & \big\downarrow \Pi_h^e & & \big\downarrow \Pi_h^t \\ P_h^1 & \xrightarrow{\nabla^\perp} & RT_h & \xrightarrow{\nabla\cdot} & P_h^0 \end{array}$$

In particular, the discrete de Rham complex (3.20) shares several fundamental properties with (3.17): for simply connected samples $\Omega \subset \mathbb{R}^2$ the sequence is exact and thus a field $m_h \in RT_h$ is divergence–free if and only if there exists a function $\phi_h \in P_h^1$ such that

$$m_h \;=\; \nabla^\perp \phi_h \;. \tag{3.22}$$

Moreover, for any $\sigma_h \in P_h^0$ there exists a field $m_h \in RT_h$ such that

$$\sigma_h \;=\; \nabla\cdot m_h \;.$$

But if we impose the constraint $|m_h| \le 1$ on fields in RT_h, the divergence $\nabla\cdot$ fails to be surjective on that restricted subset: due to Lemma 3.2 the constraint $|m_h| \le 1$ implies the upper bound

$$|(\nabla\cdot m_h)(T)| \;\le\; 4\,\mathrm{diam}(T)^{-1} \tag{3.23}$$

for every $T \in \mathcal{T}_h$, and the range of $\nabla\cdot$ now depends on the triangulation. This observation becomes crucial if we discuss refinement strategies to deal with singularities of the "magnetic charges" $\nabla\cdot m$, see Section 4.2.

3.8 The Reduced Energy on $RT_{0,h}$

We suppress all primes for the two–dimensional variables in this section.

Due to the use of divergence–conforming finite elements, the reduced micromagnetic energy E of $m_h \in RT_{0,h}$ is given by the restriction of the energy to the linear subspace $RT_{0,h} \subset H^{1/2}(\nabla\cdot)$. Thus we have

$$E(m_h) \;=\; \tfrac{1}{2}\int_{\mathbb{R}^2} |\nabla^{-1/2}\nabla\cdot m_h|^2 \; dx - 2\int_\Omega H_{ext}\cdot m_h \; dx \;, \tag{3.24}$$

where the magnetostatic part may be rewritten as

$$\tfrac{1}{2}\int_{\mathbb{R}^2} |\nabla^{-1/2}\nabla\cdot m_h|^2 \; dx \;=\; \int_{\mathbb{R}^2}\int_{\mathbb{R}^2} \frac{\nabla\cdot m_h(x)\;\nabla\cdot m_h(y)}{4\pi|x-y|}\; dy\; dx \;. \tag{3.25}$$

In particular, we are allowed to oppress an additional subscript h on E. Thus we consider the variational problem

Minimize

$$E(m_h) \;=\; \int_{\mathbb{R}^2}\int_{\mathbb{R}^2} \frac{\nabla\cdot m_h(x)\;\nabla\cdot m_h(y)}{4\pi|x-y|}\; dy\; dx \;- 2\int_\Omega H_{ext}\cdot m_h(x)\; dx \tag{3.26}$$

among all $m_h \in RT_{0,h}$ with $|m_h| \le 1$.

The question of how to deal with the constraint $|m_h| \le 1$ numerically will be discussed in Section 5. Next we take a closer look on the energy $E(m_h)$.

Since $\nabla\cdot m_h$ is a piecewise constant function on $\mathcal{T}_h$, the evaluation of $E(m_h)$ forces us to deal with the *fully populated* matrix K with entries

$$K_{ij} \;=\; \int_{T_i}\int_{T_j} \frac{1}{4\pi|x-y|}\; dy\; dx \;, \quad 1 \le i,j \le N \;, \tag{3.27}$$

where $N = \#\mathcal{T}_h$ is the number of triangles. In particular, we have to compute matrix–vector products of the form

$$Kz \;,$$

where the vector $z \in \mathbb{R}^N$ registers the piecewise constant values of $\nabla\cdot m_h \in P_h^0$. Efficient methods for the evaluation of products involving fully populated matrices will be the content of Section 4.6 and following.

For a constant external field $H_{ext} \in \mathbb{R}^2$ the Zeeman term in (3.24) is computed simply as

$$\int_\Omega H_{ext}\cdot m_h \; dx \;\; = \sum_{T\in\mathcal{T}_h} |T|\; H_{ext}\cdot m_h(x_T) \;, \tag{3.28}$$

since m_h is piecewise affine. Here x_T denotes the barycenter of the triangle T and $|T|$ its area. The numerically challenging part of the energy $E(m_h)$ is thus the stray field contribution, since it involves (3.27).

The first derivative of the energy acting on a test function $u_h \in RT_{0,h}$ reads

$$DE(m_h)u_h \;=\; 2\int_{\mathbb{R}^2}\int_{\mathbb{R}^2} \frac{\nabla\cdot u_h(x)\;\nabla\cdot m_h(y)}{4\pi|x-y|}\;dy\;dx \;-2\int_\Omega H_{ext}\cdot u_h\;dx\;, \qquad (3.29)$$

whereas the second derivative acting on test functions $u_h, v_h \in RT_{0,h}$ is given as

$$D^2E(m_h)(u_h,v_h) \;=\; 2\int_{\mathbb{R}^2}\int_{\mathbb{R}^2} \nabla\cdot u_h(x)\frac{1}{4\pi|x-y|}\nabla\cdot v_h(y)\;dy\;dx\;. \qquad (3.30)$$

By inserting the basis functions $\{\varphi_h^{(i)}\}_{i=1,..,n}$ of $RT_{0,h}$ as test functions in (3.29) and (3.30) we get the gradient and the Hessian of the energy E due to that basis. So $\nabla E(m_h)$ is the vector with components

$$(\,\nabla E(m_h)\,)_i \;=\; DE(m_h)\varphi_h^{(i)} \qquad i=1,..,n\;, \qquad (3.31)$$

whereas Hess$E$ is the $n\times n$ matrix with entries

$$(\,\mathrm{Hess}E\,)_{ij} \;=\; D^2E(m_h)(\varphi_h^{(i)},\varphi_h^{(j)}) \qquad (3.32)$$

for $i,j=1,..,n$. We note that the matrix Hess$E$ depends only on the given triangulation $\mathcal{T}_h$, but not on m_h.

Now let $\chi_h^{(1)},\chi_h^{(2)},..,\chi_h^{(N)}$ be the characteristic functions associated to the triangles $T_1,T_2,..,T_N \in \mathcal{T}_h$. The set of functions $\{\chi_h^{(j)}\}_{j=1,..,N}$ forms a basis of the space P_h^0 of piecewise constant functions on $\mathcal{T}_h$.

Since the operator $\nabla\cdot$ maps $RT_{0,h}$ to P_h^0, there is a matrix representation $W\in\mathbb{R}^{N\times n}$ of $\nabla\cdot$ such that

$$W_{ij} \;=\; \frac{1}{|T_j|}\int_{\mathbb{R}^2}\chi_h^{(i)}\;\nabla\cdot\varphi_h^{(j)}\;dx \qquad (3.33)$$

for all $i=1,..,N$ and $j=1,..,n$. Due to the locality of the basis functions involved, the matrix W is sparse. Since $N<n$, the rank of the matrix W is at most N. In particular, the Hessian of E, which may be factorized in the way

$$\mathrm{Hess}E = 2\;W^TKW\;, \qquad (3.34)$$

is a singular matrix. More precisely, for $\gamma\in\mathbb{R}^n$ we have the relation

$$\gamma^T\;\mathrm{Hess}E\;\gamma \;=\; 0 \qquad\Leftrightarrow\qquad W\gamma \;=\; 0\;,$$

since K is positive definite, and the condition $W\gamma=0$ itself is equivalent to the property $\sum_i\gamma_i\varphi_h^{(i)}\in\mathrm{Ker}(\nabla\cdot)$. Thus we have

Lemma 3.3. *For each $m_h \in RT_{0,h}$ we define the corresponding equivalence class $\tilde{m}_h$ as*

$$\tilde{m}_h \;:=\; \{u_h \in RT_{0,h} \mid \nabla\cdot u_h = \nabla\cdot m_h\}\ .$$

Then the quotient function $\tilde{E}$ defined by

$$\tilde{E}(\tilde{m}_h) \;:=\; E(m_h)$$

is a strictly convex and quadratic function on the quotient space $RT_{0,h}/\mathrm{Ker}(\nabla\cdot)$.

The reduced energy E belongs therefore to a general class of convex functions we consider in the following useful lemma. This property of convex functions is stated in [41]. We include an elementary proof here.

Lemma 3.4. *Let $f : \mathbb{R}^n \to \mathbb{R}$ be a convex function that is constant on the (unbounded) line $L \subset \mathbb{R}^n$. Then f is constant on every line L' parallel to L.*

Proof of Lemma 3.4.
Since two parallel lines, which are not identical, uniquely define a plane in $\mathbb{R}^n$, we may assume $n = 2$. Moreover, the property of convexity is invariant under affine transformations, thus it is sufficient to consider the case $f|_L = 0$ with $L = \{(a,0) \in \mathbb{R}^2 \mid a \in \mathbb{R}\}$ and $L' = \{(a,-1) \in \mathbb{R}^2 \mid a \in \mathbb{R}\}$.

We note that f is continuous on all of $\mathbb{R}^2$. Besides to that, f is constant on the line L' if it is bounded from above on L'. These facts follow from the well–known properties of convex functions.

Thus we may assume that f is non–negative and monotonically increasing on the ray $L'_+ := \{(a,-1) \in \mathbb{R}^2 \mid a \geq 0\}$. Let us define the convex sets

$$Q \;=\; \{(a,b) \in \mathbb{R}^2 \mid a \geq 0\ ,\ 0 \geq b \geq -1\}$$

and

$$\mathcal{L} \;=\; \{(a,b) \in Q \mid f(a,b) \leq f(0,-1)\}\ . \tag{3.35}$$

By definition we have $\mathcal{L} \subset Q$. Next we introduce for all $a \geq 0$ the well–defined function

$$g(a) \;=\; \min\{0 \geq b \geq -1 \mid f(a,b) \leq f(0,-1)\}\ .$$

We show that g is convex for $a \geq 0$. It is sufficient to prove

$$g\left(\frac{a_1+a_2}{2}\right) \;\leq\; \tfrac{1}{2}g(a_1) + \tfrac{1}{2}g(a_2)$$

for any given $a_1, a_2 \geq 0$. By definition of $\mathcal{L}$ there exist $0 \geq b_1, b_2 \geq -1$ such that $g(a_1) = b_1$ and $g(a_2) = b_2$. In particular, $(a_1,b_1), (a_2,b_2) \in \mathcal{L}$. Due to the convexity of $\mathcal{L}$ we have also

$$\left(\frac{a_1+a_2}{2}, \frac{b_1+b_2}{2}\right) \in \mathcal{L}\ ,$$

which gives

$$g\left(\frac{a_1+a_2}{2}\right) \;\leq\; \frac{b_1+b_2}{2} \;=\; \tfrac{1}{2}g(a_1)+\tfrac{1}{2}g(b_2)\;.$$

But g is also bounded from above and below, i. e. we have $-1 \leq g(a) \leq 0$ for all $a \geq 0$. Therefore g is constant. Since $g(0) = -1$, we have $g(a) = -1$ for every $a \geq 0$, and thus $f(a,-1) = f(0,-1)$ for all $a \geq 0$.

Now, since g is constant for $a \geq 0$, it has to be a decreasing function for $a < 0$. Thus either $g(a) \to +\infty$ as $a \to -\infty$, or g is constant on $\mathbb{R}$. By the same arguments as before, we conclude that g is indeed constant on $\mathbb{R}$. □

4 Stray Field Computation

Since the computation of the stray field energy in (3.1) amounts to the evaluation of the single layer potential operator (2.4), it dominates our numerical simulations with respect to CPU time. Efficient numerical methods for stray field computation therefore occupy a major part of our considerations.

We start in Section 4.1 with quadrature schemes for the single layer potential kernel, exploiting its homogeneity. Based on a thorough regularity analysis and a–priori estimates, we introduce a refinement rule for triangulations $\mathcal{T}_h$, see Sections 4.2 up to 4.5. The discretization of the single layer potential operator leads to a fully populated stiffness matrix, demanding compression techniques that we consider in Sections 4.7 and 4.8. As a first demonstration of the beforementioned methods in practice, we present and discuss numerical results on a linear model problem: the Dirichlet screen problem. This is the content of Section 4.9.

Major parts of Sections 4.2 up to 4.9 are joint work with Felix Otto and have been published in the preprint [19].

4.1 Quadrature Rules

Since the numerical computation of the energy $E(m_h)$ involves the calculation of the fourfold integrals

$$I(T_0, T_1) \;:=\; \int_{T_0} \int_{T_1} \frac{1}{4\pi|x-y|}\, dx\, dy \tag{4.1}$$

for pairs of triangles $T_0, T_1 \in \mathcal{T}_h$, we start this Section by introducing corresponding quadrature schemes: for any source point $y \in \mathbb{R}^2$ and any triangle $T_0 \in \mathcal{T}_h$ the twofold integral

$$I(y) \;:=\; \int_{T_0} \frac{1}{4\pi|x-y|}\, dx \tag{4.2}$$

can be evaluated analytically, see [1]. But for $y \in \partial T_0$ the first derivatives of $I(y)$ exhibit a singularity, thus we have to approach carefully the outer integration $\int_{T_1} I(y)\, dy$ if T_0 and T_1 have common points.

We suppress all primes for the two–dimensional variables in this section.

4.1.1 The Self–Energy of Triangles in $\mathcal{T}_h$

If T_0 and T_1 in (4.1) are identical, we call $I(T_0) = I(T_0, T_0)$ the *self–energy* of the triangle T_0.

Now let the reference triangle T_{ref} be given in Cartesian coordinates as depicted in Figure 4.1.

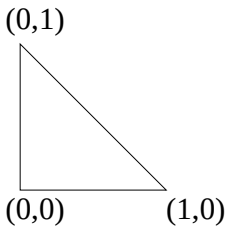

Figure 4.1: The reference triangle $T_{ref} \subset \mathbb{R}^2$. It is an isosceles right triangle, both legs are of length one.

Lemma 4.1. *For the reference triangle T_{ref} in Figure 4.1 we have the self–energy*

$$4\pi I(T_{ref}) \;=\; \int_{T_{ref}} \int_{T_{ref}} \frac{1}{|x-y|}\; dy\; dx \;=\; -\tfrac{1}{3}(2+\sqrt{2})\log(-1+\sqrt{2})\;.$$

For a general triangle $T \in \mathcal{T}_h$ of refinement level k (see Section 3.4) the self–energy is computed in terms of $I(T_{ref})$ as

$$\int_T \int_T \frac{1}{4\pi|x-y|}\; dx\; dy \;=\; h^3\; 2^{-3k/2}\; I(T_{ref})\;,$$

according to the scaling properties of the kernel. Lemma 4.1 is related to

Lemma 4.2. *For the two–dimensional square $\Omega = (0,1)^2$ we have the self–energy*

$$\begin{aligned} 4\pi I(\Omega) \;&=\; \int_\Omega \int_\Omega \frac{1}{|x-y|}\; dy\; dx \\ =\; \tfrac{4}{3}(1-\sqrt{2}) - 2\log(-1+\sqrt{2}) - \tfrac{1}{2}\log(2+\sqrt{2}) + \tfrac{1}{2}\log(2-\sqrt{2}) + 3\;&\mathrm{artanh}(\tfrac{1}{2}\sqrt{2})\;. \end{aligned}$$

For any rectangular sample Ω the self–energy can be evaluated analytically by substitution to multiple integrals of the kernel function $1/r$ (see [37, Chapter 3.2.5 (C)]). Since the corresponding analytic expressions for triangles are hardly found in literature, we present the proof of Lemma 4.1 in an appendix to this Thesis, see Section 7.

4.1.2 The Interaction Energy of Distant Triangles

For pairs of triangles $T_0, T_1 \in \mathcal{T}_h$ with positive distance

$$\mathrm{dist}(T_0, T_1) \;>\; 0$$

comparable to their diameters, we apply a semi–analytical ansatz, since the integrand in (4.1) is smooth on $T_0 \times T_1$. We presume that T_1 denotes the larger triangle. On T_1 we apply a symmetrical Gaussian quadrature rule of fixed degree $d > 0$ provided by [20]. Our numerical experiments in Section 4.1.6 suggest to set $d = 5$. For any Gaussian point $y \in T_1$ the twofold integrals

$$I(y) \;=\; \int_{T_0} \frac{1}{4\pi|x-y|}\; dx$$

are evaluated analytically according to [1].

4.1.3 The Interaction Energy of Neighboring Triangles

We introduce the following classification of neighboring triangles:

- *Edge neighbors*: these are pairs of non–identical triangles $T_0, T_1 \in \mathcal{T}_h$ that share an edge;
- *Vertex neighbors*: these are pairs of triangles $T_0, T_1 \in \mathcal{T}_h$ that share a vertex but no edge.

For these pairs of triangles the integrand in (4.1) becomes weakly singular. Moreover, the derivatives of the inner integration (4.2) become singular in the triangles' common points, and a Gaussian quadrature as in the case of distant triangles is therefore precarious.

In [4] a splitting strategy is presented for the numerical integration of weakly singular kernels in two dimensions. We generalize this ansatz to the fourfold integrals (4.1). Generally speaking, this strategy relies on the combination of the triangulation's structural properties with those of the integrand. In the case of vertex neighbors, we split each triangle into subtriangles of equal size by virtual bisection. On pairs of subtriangles where the integrand is regular, we apply standard Gaussian quadrature rules. Due to the scaling properties of the kernel $k(\cdot\,,\cdot)$, the interaction energies for the remaining pairs of subtriangles turn into the unknowns of a system of linear equations. The splitting strategy for edge neighbors is quite similar.

The term "virtual bisection" indicates that this splitting is only a technical step in the numerical quadrature scheme. It does not lead to a lasting refinement of the given triangulation $\mathcal{T}_h$. In particular, we are not concerned with the occurance of hanging nodes in a virtual bisection.

We briefly recall the basic properties of the function k. The kernel

$$k(x,y) \;=\; \frac{1}{4\pi|x-y|}$$

is *asymptotically smooth*, i. e. we have for all $n \in \mathbb{N}$ and $z \in \{x_1, x_2, y_1, y_2\}$ the inequality

$$\left|\frac{\partial^n k}{\partial z^n}(x,y)\right| \;\leq\; \frac{n!}{4\pi|x-y|^{n+1}}\;.$$

An analogous inequality for mixed partial derivatives is obvious. Furthermore, the kernel has the following structural properties.

- Symmetry: for all $x, y \in \mathbb{R}^2$ there holds

$$k(x,y) \;=\; k(y,x)\;.$$

- Translational invariance: given $x, y \in \mathbb{R}^2$, we have

$$k(x,y) \;=\; k(x+a, y+a) \quad \text{for all} \quad a \in \mathbb{R}^2\;.$$

- Rotational invariance: given $x, y \in \mathbb{R}^2$, we have

$$k(x,y) \;=\; k(Ax,Ay) \quad \text{for all orthogonal matrices} \quad A \in O(2)\ .$$

- Homogeneity: given $x, y \in \mathbb{R}^2$, there holds

$$k(rx,ry) \;=\; r^{-1}k(x,y) \quad \text{for all} \quad r \in \mathbb{R}^+\ .$$

Next we turn to the structural properties of the triangulation $\mathcal{T}_h$. First we note that any triangle $T \in \mathcal{T}_h$ is a scaled, rotated, and translated copy of the reference triangle T_{ref}. But by construction, at least one of the triangle's sides is parallel to one of the coordinate axes. The triangle $T \in \mathcal{T}_h$ is therefore up to translation and scaling one of the sixteen triangles depicted in Figure 4.2. Here the two legs of each triangle are assumed to have length one.

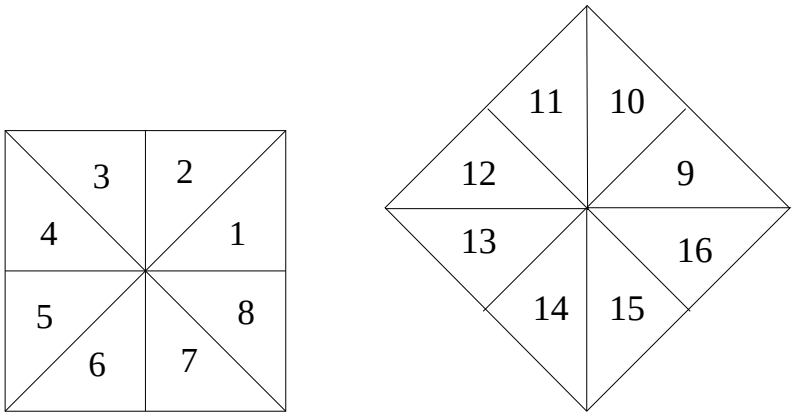

Figure 4.2: The possible different orientations of the reference triangle.

For each index $i \in \{1, 2, .., 16\}$ in Figure 4.2 we denote the corresponding triangle by T_i. For any pair of such triangles we consider the interaction energy

$$I(T_i, T_j) \;:=\; \int_{T_i}\int_{T_j} \frac{1}{4\pi|x-y|}\, dx\, dy\ , \quad i,j \in \{1,2,..,16\}\ . \tag{4.3}$$

For $i = j$ we have $I(T_i, T_i) = I(T_{ref})$, where $I(T_{ref})$ is the self–energy of the reference triangle T_{ref} due to Lemma 4.1. W. l. o. g. , we may assume $i = 1$ in (4.3).

4.1.4 The Interaction Energy of Vertex Neighbors

We start by considering vertex neighbors of equal size with both hypotenuses meeting at the common vertex. The following interaction energies never occur in our calculations since they correspond to prohibited neighbor configurations:

$$I(T_1, T_9)\ ,\ I(T_1, T_{10})\ ,\ I(T_1, T_{16})\ .$$

Due to symmetry considerations we may confine ourselves to the following permitted neighbor configurations:

$$I(T_1, T_j) \quad \text{with} \quad j \in \{3, 4, 5, 6, 11, 12, 13, 15\} \, . \tag{4.4}$$

A virtual bisection of the vertex neighbors in combination with the homogeneity of the kernel $k(\cdot\,, \cdot)$ leads to a system of linear equations, as indicated by the diagrams on the following pages. Here the dashed lines indicate the virtual bisection, and the indices in the figures are those of the subtriangles S_1, S_2, S_3, and S_4. The interaction energy of two subtriangles like S_1 and S_3 is denoted by $I(S_1, S_3)$.

The interaction energies $I(S_i, S_j)$ for $1 \leq i, j \leq 4$ and $\operatorname{dist}(S_i, S_j) > 0$ are approximated numerically as described in Subsection 4.1.2 with a Gaussian quadrature rule of degree $d = 7$. Solving the resulting linear system for the interaction energies (4.4) yields the entries of Table 4.1.

j	$I(T_1, T_j)$
3	1.98414834e–2
4	1.57542299e–2
5	1.44450574e–2
6	1.53548034e–2
11	2.04871058e–2
12	1.55404669e–2
13	1.44545195e–2
15	1.92854249e–2

Table 4.1: Tight approximation of the interaction energies for the vertex neighbors (4.4).

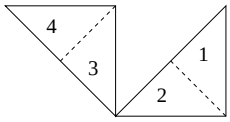

$$I(T_1, T_3) \;=\; I(S_1, S_3) + I(S_1, S_4) + I(S_2, S_4) + \tfrac{1}{4}\sqrt{2}\; I(T_1, T_3)$$

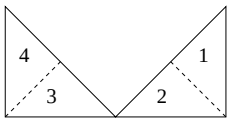

$$I(T_1, T_4) \;=\; 2\; I(S_1, S_3) + I(S_1, S_4) + \tfrac{1}{4}\sqrt{2}\; I(T_1, T_6)$$

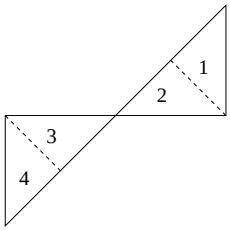

$$I(T_1, T_5) \;=\; 2\; I(S_1, S_3) + I(S_1, S_4) + \tfrac{1}{4}\sqrt{2}\; I(T_1, T_5)$$

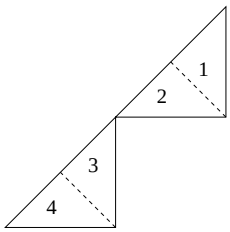

$$I(T_1, T_6) \;=\; 2\; I(S_1, S_3) + I(S_1, S_4) + \tfrac{1}{4}\sqrt{2}\; I(T_1, T_4)$$

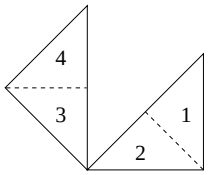

$$I(T_1, T_{11}) = 2\ I(S_1, S_3) + I(S_1, S_4) + \tfrac{1}{4}\sqrt{2}\ I(T_1, T_{15})$$

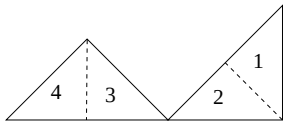

$$I(T_1, T_{12}) = I(S_1, S_3) + I(S_1, S_4) + I(S_2, S_4) + \tfrac{1}{4}\sqrt{2}\ I(T_1, T_{12})$$

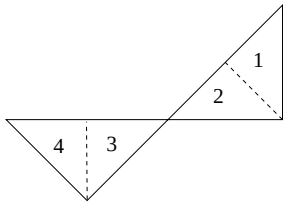

$$I(T_1, T_{13}) \ = \ 2\ I(S_1, S_3) + I(S_1, S_4) + \tfrac{1}{4}\sqrt{2}\ I(T_1, T_{13})$$

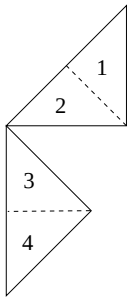

$$I(T_1, T_{15}) = 2\ I(S_1, S_3) + I(S_1, S_4) + \tfrac{1}{4}\sqrt{2}\ I(T_1, T_{11})$$

Next we consider vertex neighbors $T_0, T_1 \in \mathcal{T}_h$ of different size. This case is reduced to the previous one by additional virtual bisections. First, modulo a virtual bisection, it is sufficient to consider vertex neighbors that meet at a common $\pi/4$–degree vertex. Besides we note that any triangle has at most three edge neighbors and at most seven vertex neighbors, since $\mathcal{T}_h$ consists only of isosceles right triangles.

In the following, let $T_0 \in \mathcal{T}_h$ be of refinement level k. If the common vertex x_0 lies on the boundary of the rectangular sample Ω, then the vertex neighbor T_1 is of refinement level k' with

$$k - 3 \;\leq\; k' \;\leq\; k + 3 \;,$$

as illustrated in Figure 4.3. If the common vertex lies in the interior of Ω, the same conclusion is evident from Figure 4.4. Thus, after performing at most three additional virtual bisections, it is sufficient to consider vertex neighbors of the same size. This is also evident from the formal algorithm included at the end of the following Section.

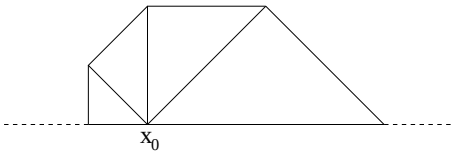

Figure 4.3: Vertex neighbors with common vertex x_0 on the boundary of Ω.

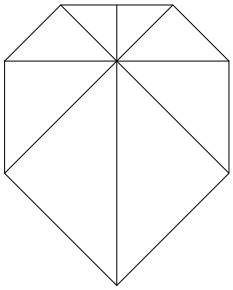

Figure 4.4: Vertex neighbors: For a triangle of level 1, the smallest possible vertex neighbor is of level 3.

4.1.5 The Interaction Energy of Edge Neighbors

Obviously, edge neighbors can differ in their size only by one refinement level. Thus, up to rotations and scaling, there are only four possible neighbor configurations (the legs of the solid line triangles are assumed to have length one):

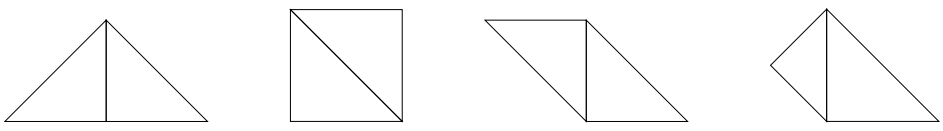

The corresponding splitting strategy is illustrated by the following diagrams. Again, the dashed lines indicate the virtual bisection, and the indices in the figures are those of the Triangles S_1, S_2, S_3, and S_4. The values of $I(\Omega)$ and $I(T_{ref})$ are exactly known from Lemma 4.2 and Lemma 4.1. The approximate value of $I(T_1, T_3)$ can be read off from Table 4.1. This gives the results in Table 4.2.

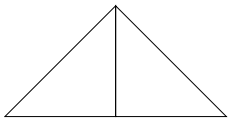

$$2\sqrt{2}\ I(T_{ref}) \ = \ 2\ I(T_{ref}) + I(T_1, T_8)$$

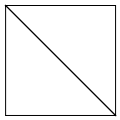

$$I(\Omega) \ = \ 2\ I(T_{ref}) + 2\ I(T_1, T_2)$$

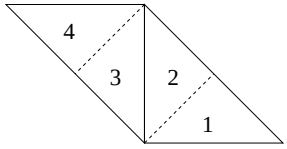

$$I(S_1 \cup S_2, S_3 \cup S_4) \ = \ I(S_1, S_4) + \tfrac{1}{4}\sqrt{2}\ I(T_1, T_2) + \tfrac{1}{2}\sqrt{2}\ I(T_1, T_3)$$

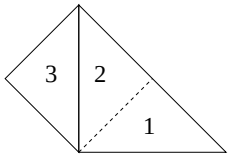

$$I(S_1 \cup S_2, S_3) \ = \ \tfrac{1}{4}\sqrt{2}\ I(T_1, T_2) + \tfrac{1}{4}\sqrt{2}\ I(T_1, T_3)$$

	3.30631020e–2
	3.84788042e–2
	3.18705920e–2
	2.06193354e–2

Table 4.2: Tight approximation of the interaction energies for the possible edge neighbors.

The nunmerical quadrature scheme for (4.1) developed so far, is summarized in the following abstract algorithm:

procedure $I(T_0, T_1)$
if $T_0 = T_1$
    compute $I(T_0, T_0)$ as described in Subsection 4.1.1 ;
else if $\mathrm{dist}(T_0, T_1) > 0$
    compute $I(T_0, T_1)$ as described in Subsection 4.1.2 ;
else if T_0, T_1 are edge neighbors
    read off $I(T_0, T_1)$ from Table 4.2 (scaled appropriately) ;
else if T_0, T_1 are vertex neighbors
    for $i = 0$ **to** 1
        if T_i has $\pi/2$–angle at common vertex
            split T_i into T_i' and T_i'',
            then compute $I(T_i, T_{i+1}) = I(T_i', T_{i+1}) + I(T_i'', T_{i+1})$;
    end
    for $i = 0$ **to** 1
        if $|T_i| > |T_{i+1}|$
            split T_i into T_i' and T_i'',
            then compute $I(T_i, T_{i+1}) = I(T_i', T_{i+1}) + I(T_i'', T_{i+1})$;
    end
    if $|T_0| = |T_1|$
        read off $I(T_0, T_1)$ from Table 4.1 (scaled appropriately) ;
return $I(T_0, T_1)$.

4.1.6 Numerical Tests

We compare the theoretical value for the self–energy of the unit square Ω in Lemma 4.2 with numerical results gained by the following method: choose a triangulation of class $\mathcal{Q}_h$ or $\mathcal{T}_h$ consisting of triangles $T_1, T_2, .., T_N$, and sum up all interaction

energies of the triangles:

$$\int_\Omega \int_\Omega \frac{1}{4\pi|x-y|}\, dx\, dy \;=\; \sum_{i=1}^{N}\sum_{j=1}^{N} \int_{T_i}\int_{T_j} \frac{1}{4\pi|x-y|}\, dx\, dy\ . \tag{4.5}$$

Here the interaction energy for a given pair of triangles is approximated by the quadrature scheme introduced in the preceding Sections. We choose different degrees for the Gaussian quadrature rules involved. We document the CPU time in seconds for the numerical approximation of (4.5), and the relative error (4.7). Our numerical tests suggest a degree of five for the Gaussian quadrature rule in order to attain a tolerance of 5.0e–4 for the relative error.

We notice that evaluating (4.5) amounts to the computation of the quadratic form

$$z^T K z\ , \tag{4.6}$$

where K is the matrix with entries (3.27) and $z \in \mathbb{R}^N$ is the vector

$$z = (1, 1, .., 1)^T\ .$$

The relative error listed in the Tables 4.3 and 4.4 can then be written as

$$\sqrt{\Big|\frac{I(\Omega) - z^T K z}{I(\Omega)}\Big|}\ . \tag{4.7}$$

This definition of the relative error with respect to energy will be justified in detail in Section 4.9.

d	CPU time (s)	relative error
3	6.18e+0	3.89e–3
4	9.16e+0	6.80e–4
5	1.05e+1	4.00e–4
6	1.74e+1	3.01e–4
7	1.87e+1	3.02e–4

Table 4.3: Numerical test on the $\mathcal{Q}_h$–type triangulation in Figure 3.2: d is the degree of the Gaussian quadrature rule involved, the second column documents the CPU time in seconds, and the relative error is defined in (4.7). All numerical experiments were done on a Pentium III processor running at 700 MHz.

4.1.7 Quadrature Schemes for General Triangulations

For general, regular triangulations $\mathcal{T}$ and neighboring triangles $A, B \in \mathcal{T}$ we replace the virtual green refinement by a virtual *red* refinement: the triangles A and B are subdivided into the subtriangles $A_1, .., A_4$ and $B_1, .., B_4$, respectively, as indicated

d	CPU time (s)	relative error
3	3.97e+1	6.13e–3
4	5.93e+1	7.21e–4
5	6.73e+1	2.32e–4
6	1.12e+2	3.77e–4
7	1.20e+2	3.72e–4

Table 4.4: Numerical test on the $\mathcal{T}_h$–type triangulation in Figure 3.4. Notations are as in Table 4.3.

in Figures 4.5, 4.6, and 4.7. We notice that the subtriangles A_i, $i = 1, 2, 3, 4$, are of equal size and are a scaled version of the original triangle A. The same observation holds for B_i, $i = 1, 2, 3, 4$, and B.

The scaling properties of the kernel $k(\cdot, \cdot)$ now yield the formulas (4.8), (4.9), and (4.10), where the right hand side of each equation contains only interaction energies either of distant triangles or of neighbor configurations considered by one of the other two formulas.

The implementation of an algorithm solving the corresponding system of linear equations is straightforward. We apply a Gaussian quadrature rule of degree $d = 5$ on all distant triangles.

The quadrature schemes for general, regular triangulations are used in Section 5.11 in the stray field computation on circular domains.

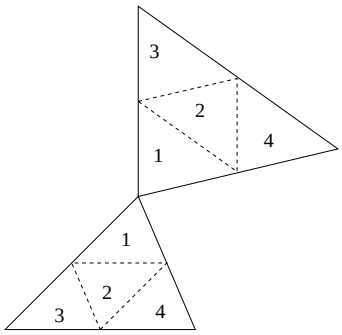

$$(1 - \tfrac{1}{8})\ I(A, B) \ = \ \sum_{i=2}^{4} I(A_1, B_i) + \sum_{i=2}^{4} I(A_i, B) \tag{4.8}$$

Figure 4.5: Splitting strategy for general vertex neighbors.

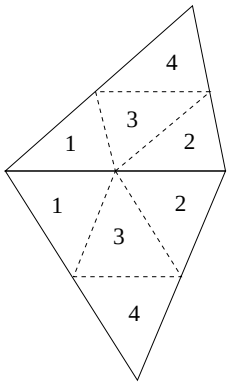

$$(1-\tfrac{1}{4})\ I(A,B) \ = \ \sum_{i=1}^{2}\sum_{j\neq i} I(A_i,B_j) + \sum_{i=1}^{4} I(A_3,B_i) + I(A_4,B) \qquad (4.9)$$

Figure 4.6: Splitting strategy for general edge neighbors.

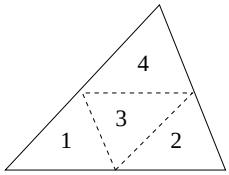

$$(1-\tfrac{1}{2})\ I(A,A) \ = \ \sum_{i=1}^{4}\sum_{j\neq i} I(A_i,A_j) \qquad (4.10)$$

Figure 4.7: Splitting strategy for the self–energie of general triangles.

4.2 The Dirichlet Screen Problem

In the following sections, we adopt the prime notation of Remark 2.1 for two–dimensional variables.

For sufficiently weak external field H'_{ext}, the constraint (3.3) is not active, see [16]. In view of (3.6), the reduced problem turns into the quadratic variational problem

Minimize
$$E(\sigma) \ = \ \tfrac{1}{2}\int_{\mathbb{R}^2} |(\nabla')^{-1/2}\sigma|^2 dx' + 2\int_{\Omega'} H'_{ext}\cdot x'\,\sigma\,dx' \qquad (4.11)$$
among all σ with $\int_{\Omega'}\sigma dx' = 0$.

From (2.9) we see that (4.11) can be understood as a saddle point problem in (σ, u) with solution (σ^*, u^*). The first variation in u yields

$$\begin{aligned} \Delta u^* &= 0 \qquad \text{in } \mathbb{R}^3 - (\Omega'\times\{0\}), \\ \partial_3 u^*(x',0+) - \partial_3 u^*(x',0-) &= \sigma^*(x') \quad \text{for } x'\in\Omega'. \end{aligned} \qquad (4.12)$$

The first variation in σ yields, up to additive constants,

$$u^*(x',0) \ = \ H'_{ext}\cdot x' \quad \text{for } x'\in\Omega'. \qquad (4.13)$$

Hence *solving* the variational problem (4.11) amounts to *evaluating* the Dirichlet–Neumann operator of the *bounded* surface Ω'. For constant fields H'_{ext}, this representation shows that it is essentially the geometry of Ω' which determines σ^*.

Problem (4.11) is mathematically equivalent to the *Dirichlet screen problem*. This problem is usually encountered in an electrostatic instead of a magnetostatic context: Given the surface potential u find the charge density σ of a thin–film conductor described by Ω'. Mathematically, this amounts to the solution of a Dirichlet problem in $\mathbb{R}^3 - (\Omega' \times \{0\})$ with the help of a single layer potential on $\Omega' \times \{0\}$. In our reduced thin–film model, the prescribed potential is related to the external field via $u(x') = H'_{ext} \cdot x'$.

The Dirichlet screen problem is a well–studied problem for domains Ω' with polygonal boundary $\partial\Omega'$. In our setting the regularity theory and numerical analysis due to [22, 52] is of particular interest: there it is shown that the solution σ^* fails to be a smooth function up to the boundary $\partial\Omega'$.

The singularities of σ^* near edges and corners raise the question of how to choose a local refinement strategy for a triangulation of Ω'. In the case of graded meshes and piecewise constant functions it is shown in [22] that it suffices to refine the mesh only towards the edges to retain optimal convergence. In particular, it is observed that near an edge, but away from the corners, the solution σ^* of (4.11) becomes singular only in the direction orthogonal to the edge. As a consequence, efficient numerical approximations are based on meshes which are anisotropically graded towards an edge, see Figure 4.8 for an illustration.

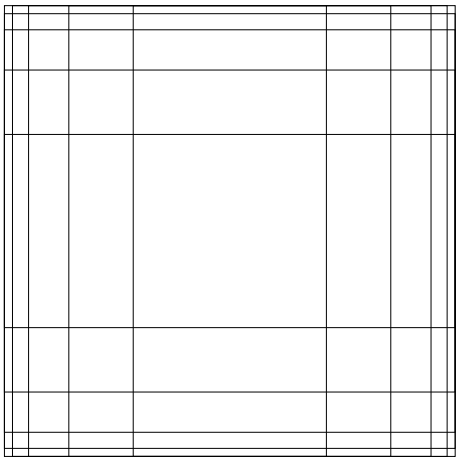

Figure 4.8: Illustration of a graded mesh. Near edges, but away from the corners, elements become very long and thin.

For our type of finite element discretization such graded meshes are prohibitive. Since subsequent computations not only involve σ, but also the magnetization m itself, we have to keep in mind the conclusion of Lemma 3.2: the constraint $||m_h||_\infty <$

1 for any $m_h \in RT_{0,h}$ leads to the upper bound

$$|\sigma_h(x')| \;=\; |\nabla' \cdot m_h(x')| \;\leq\; 4\ \mathrm{diam}(T)^{-1} \tag{4.14}$$

for any $T \in \mathcal{T}_h$ and $x' \in T$. Since the diameter of T in (4.14) can not be replaced by the elongation of T in one of the two dimensions, we have to consider an *isotropic* refinement strategy.

4.3 Regularity Theory

It is well–known and easy to understand that σ^* diverges like $r^{-1/2}$ where r denotes the distance to a smooth edge of Ω'. Corner singularities are at least numerically well–characterized: In [42], it is shown that σ^* diverges like $R^{-0.7034}$ where R denotes the distance to a square corner, like the corner $(-\frac{1}{2}, -\frac{1}{2})$ of $\Omega' = (-\frac{1}{2}, \frac{1}{2})^2$. For our purpose the special form of the corner singularity is irrelevant. Roughly speaking, we only need the bound R^{-1}. On the other hand, it is important to know how the $r^{-1/2}$–behavior near the middle of an edge degenerates as one approaches a corner.

In [52] it is shown that σ^* allows for a decomposition into edge and corner singularities in the vicinity of a corner of Ω'. This regularity result is used in [22] for the numerical analysis of the Dirichlet screen problem on anisotropically graded meshes.

We give here an elementary and self–contained proof of the statement our numerical analysis in Section 4.4 requires. In particular, we do not attempt to characterize the corner singularities. Our analysis is elementary in the sense that it is based exclusively on the maximum principle. For simplicity, we formulate the regularity result for $\Omega' = \left(-\frac{1}{2}, \frac{1}{2}\right)^2$. However, the statements of the following Theorem 4.1 generalize to arbitrary convex polygonal domains in a straightforward manner, see Remark 4.2 at the end of this section.

We use the following language:

$$\begin{aligned} \text{edges} &= \partial\Omega', \\ \text{corners} &= \left\{ \left(\tfrac{1}{2}, \tfrac{1}{2}\right), \left(\tfrac{1}{2}, -\tfrac{1}{2}\right) \left(-\tfrac{1}{2}, \tfrac{1}{2}\right), \left(-\tfrac{1}{2}, -\tfrac{1}{2}\right) \right\} \ . \end{aligned}$$

For any given point $x' \in \Omega'$ we set

$$r \;:=\; \mathrm{dist}(x', \mathrm{edges}) \ , \quad R \;:=\; \mathrm{dist}(x', \mathrm{corners}) \ . \tag{4.15}$$

The method we present works for the general variational problem

$$\begin{aligned} &\text{Minimize} \\ &E(\sigma) \;=\; \tfrac{1}{2} \int_{\mathbb{R}^2} |(\nabla')^{-1/2} \sigma|^2 dx' + 2 \int_{\Omega'} g\, \sigma \, dx' \\ &\text{among all } \sigma \text{ with } \textstyle\int_{\Omega'} \sigma dx' = 0. \end{aligned} \tag{4.16}$$

Here we assume $g \in C^3(\overline{\Omega'})$.

In the sequel, we use the notation "$\lesssim$" to denote "$\leq C$" with a generic universal constant C.

Theorem 4.1. *For given $g \in C^3(\overline{\Omega'})$ we set*

$$\begin{aligned} G_2 &:= \sup_{\Omega'} |g| + \sup_{\Omega'} |\nabla' g| + \sup_{\Omega'} |(\nabla')^2 g| \ , \\ G_3 &:= \sup_{\Omega'} |g| + \sup_{\Omega'} |\nabla' g| + \sup_{\Omega'} |(\nabla')^2 g| + \sup_{\Omega'} |(\nabla')^3 g| \ . \end{aligned}$$

Then there exists a universal constant $\delta > 0$ such that the solution σ^* of (4.16) satisfies for all $x' \in \Omega'$

$$|\sigma^*(x')| \ \lesssim \ r^{-1/2} R^{-1/2+\delta} \left(\sup_{B_1} |u^*| + G_2 \right), \tag{4.17}$$

$$|\nabla' \sigma^*(x')| \ \lesssim \ r^{-3/2} R^{-1/2+\delta} \left(\sup_{B_1} |u^*| + G_3 \right). \tag{4.18}$$

Here $u^* \in H^1(\mathbb{R}^3) \cap C^0(\mathbb{R}^3)$ is the solution to (4.12) with $u^*(x',0) = g(x')$ for $x' \in \Omega'$.

Remark 4.1. *Problem (4.11) implies the choice $g(x') = H'_{ext} \cdot x'$ with constant vector $H'_{ext} \in \mathbb{R}^2$. The maximum principle on $\mathbb{R}^3 - (\Omega' \times \{0\})$ then yields*

$$\sup_{\mathbb{R}^3} |u^*| \ \leq \ \sup_{x' \in \Omega'} |H'_{ext} \cdot x'| \ \lesssim \ |H'_{ext}| \ . \tag{4.19}$$

The inequalities (4.17) and (4.18) therefore turn into

$$|\sigma^*(x')| \ \lesssim \ r^{-1/2} R^{-1/2+\delta} \ |H'_{ext}|, \tag{4.20}$$

$$|\nabla' \sigma^*(x')| \ \lesssim \ r^{-3/2} R^{-1/2+\delta} \ |H'_{ext}|. \tag{4.21}$$

Theorem 4.1 relies on the following lemmata, which are proven in Section 4.3.2. These proofs in turn rely on elementary applications of the maximum principle considered in Section 4.3.1.

Lemma 4.3. *Let u be harmonic in $B_1 - \{x_3 = 0\}$ with*

$$u \ \leq \ g \ \text{on} \ B'_1$$

for a smooth function g defined on B'_1. Then we have for all $\rho \leq 1$

$$\sup_{B_\rho} (u - g(0)) \ \lesssim \ \rho \left(\sup_{B_1} (u - g(0)) + \sup_{B'_1} |\nabla' g| + \sup_{B'_1} |(\nabla')^2 g| \right) \ . \tag{4.22}$$

By symmetry, there follows:

Corollary 4.1. *Let u be harmonic in $B_1 - \{x_3 = 0\}$ with smooth boundary values g on B'_1. Then we have for all $\rho \leq 1$*

$$\sup_{B_\rho} |u - g(0)| \ \lesssim \ \rho \left(\sup_{B_1} |u - g(0)| + \sup_{B'_1} |\nabla' g| + \sup_{B'_1} |(\nabla')^2 g| \right) \ . \tag{4.23}$$

Lemma 4.4. *Let u be harmonic in $B_1 - \{x_3 = 0, x_2 \geq 0\}$ with smooth boundary values g on $B_1' \cap \{x_2 \geq 0\}$. Then we have for all $\rho \leq 1$*

$$\sup_{B_\rho} |u - g(0)| \lesssim \rho^{1/2} \left(\sup_{B_1} |u - g(0)| + \sup_{B_1' \cap \{x_2 \geq 0\}} |\nabla' g| + \sup_{B_1' \cap \{x_2 \geq 0\}} |(\nabla')^2 g| \right) . \tag{4.24}$$

Lemma 4.5. *There exists a universal $\delta > 0$ with the property: for any u which is harmonic in $B_1 - \{x_3 = 0, x_2 \geq 0, x_1 \geq 0\}$ with smooth boundary values g on $B_1' \cap \{x_2 \geq 0, x_1 \geq 0\}$ we have*

$$\sup_{B_\rho} |u - g(0)| \lesssim \rho^{\delta} \left(\sup_{B_1} |u - g(0)| + \sup_{B_1' \cap \{x_2 \geq 0, x_1 \geq 0\}} |\nabla' g| \right) \tag{4.25}$$

for any $\rho \leq 1$.

Lemma 4.6. *Let u be harmonic in $B_1 - \{x_3 = 0\}$ with smooth boundary values g on B_1'. Then we have*

$$\sup_{B_{1/2}} |\nabla' u| \lesssim \sup_{B_1} |u| + \sup_{B_1'} |\nabla' g| .$$

Proof of Theorem 4.1
We first address (4.17). Let $x' \in \Omega'$ be arbitrary and set

$$r := \operatorname{dist}(x', \text{edges}) \leq \operatorname{dist}(x', \text{corners}) =: R \leq 1 .$$

It suffices to consider points x with

$$4r \leq R , \tag{4.26}$$

since the right hand side of (4.17) diverges only as x' approaches $\partial\Omega'$. Applying Corollary 4.1 (rescaled and translated), we get for $\rho \leq r$

$$\rho^{-1} \sup_{B_\rho(x')} |u^* - g(x')| \lesssim r^{-1} \sup_{B_r(x')} |u^* - g(x')| + \sup_{B_r'(x')} |\nabla' g| + r \sup_{B_r'(x')} |(\nabla')^2 g| .$$

In the limit $\rho \downarrow 0$ this yields due to the definition of u^*

$$|\sigma^*(x')| \lesssim r^{-1} \sup_{B_r(x')} |u^* - g(x')| + \sup_{\Omega'} |\nabla' g| + r \sup_{\Omega'} |(\nabla')^2 g| . \tag{4.27}$$

Now we need to estimate the term

$$r^{-1} \sup_{B_r(x')} |u^* - g(x')| .$$

For this purpose let $y' \in$ edges be such that

$$r = |x' - y'| . \tag{4.28}$$

Because of $B_r(x') \subset B_{2r}(y')$ and

$$|g(x') - g(y')| \;\leq\; r \sup_{\Omega'} |\nabla' g| \;,$$

we have

$$r^{-1} \sup_{B_r(x')} |u^* - g(x')| \;\leq\; r^{-1} \sup_{B_{2r}(y')} |u^* - g(y')| + \sup_{\Omega'} |\nabla' g| \;. \tag{4.29}$$

Now let $z' \in$ corners denote the corner next to y'. Then we have for the distance $\overline{R} = |y' - z'|$ the relation

$$R\sqrt{\tfrac{15}{16}} \;\leq\; \overline{R} \;\leq\; R \;,$$

due to (4.26). Thus a rescaled and translated version of Lemma 4.4 applied on $B_{\overline{R}}(y')$ yields

$$\begin{aligned} &\sup_{B_{2r}(y')} |u^* - g(y')| \\ &\qquad \lesssim \; \left(\frac{r}{R}\right)^{1/2} \left(\sup_{B_R(y')} |u^* - g(y')| + R \sup_{\Omega'} |\nabla' g| + R^2 \sup_{\Omega'} |(\nabla')^2 g| \right) \;. \end{aligned} \tag{4.30}$$

From (4.29) and (4.30) we get

$$\begin{aligned} &r^{-1} \sup_{B_r(x')} |u^* - g(x')| \\ &\lesssim (rR)^{-1/2} \left(\sup_{B_R(y')} |u^* - g(y')| + R \sup_{B'_R(y')} |\nabla' g| + R^2 \sup_{B'_R(y')} |(\nabla')^2 g| \right) + \sup_{B'_{2r}} |\nabla' g| \;. \end{aligned} \tag{4.31}$$

Estimates (4.27) and (4.31) yield (we notice that $(rR)^{-1/2} \geq 1$ due to (4.26))

$$|\sigma^*(x')| \;\lesssim\; (rR)^{-1/2} \left(\sup_{B_R(y')} |u^* - g(y')| + R \sup_{B'_R(y')} |\nabla' g| + R^2 \sup_{B'_R(y')} |(\nabla')^2 g| \right) \;. \tag{4.32}$$

Now we need to estimate

$$\sup_{B_R(y')} |u^* - g(y')| \;.$$

Because of $B_R(y') \subset B_{2R}(z')$ for the corner z' next to y' and

$$|g(y') - g(z')| \;\lesssim\; R \sup_{\Omega'} |\nabla' g|$$

we have

$$\sup_{B_R(y')} |u^* - g(y')| \;\lesssim\; \sup_{B_{2R}(z')} |u^* - g(z')| + R \sup_{\Omega'} |\nabla' g| \;. \tag{4.33}$$

A translated version of Lemma 4.5 yields

$$\sup_{B_{2R}(z')} |u^* - g(z')| \;\lesssim\; R^\delta \left(\sup_{B_1} |u^* - g(z')| + \sup_{\Omega'} |\nabla' g| \right) \;. \tag{4.34}$$

From (4.33) and (4.34) we get (with $R^\delta \geq R$)

$$\sup_{B_R(y')} |u^* - g(y')| \lesssim R^\delta \left(\sup_{B_1} |u^* - g(z')| + \sup_{\Omega'} |\nabla' g| \right) . \tag{4.35}$$

Combining (4.32) and (4.35), we conclude

$$\begin{aligned} &|\sigma^*(x')| \\ &\lesssim (rR)^{-1/2} \left(R^\delta (\sup_{B_1} |u^*| + \sup_{\Omega'} |g| + \sup_{\Omega'} |\nabla' g|) + R \sup_{\Omega'} |\nabla' g| + R^2 \sup_{\Omega'} |(\nabla')^2 g| \right) \\ &\lesssim r^{-1/2} R^{-1/2+\delta} \left(\sup_{B_1} |u^*| + \sup_{\Omega'} |g| + \sup_{\Omega'} |\nabla' g| + \sup_{\Omega'} |(\nabla')^2 g| \right) . \end{aligned} \tag{4.36}$$

With the definition of G_2 this proves (4.17).

It remains to show (4.18). Our proof relies on the estimate

$$\rho^{-1} \sup_{B_\rho(x')} |u^* - g(x')| \lesssim r^{-1/2} R^{-1/2+\delta} \left(\sup_{B_1} |u^*| + \sup_{\Omega'} |g| + \sup_{\Omega'} |\nabla' g| + \sup_{\Omega'} |(\nabla')^2 g| \right) \tag{4.37}$$

for $\rho \leq r$, which follows directly from (4.17) and the definition of u^*. By symmetry it is sufficient to bound the derivative $\partial_1 \sigma^*$ from above. By applying Corollary 4.1 (translated and rescaled) to the harmonic function $\partial_1 u^*$ we get

$$\begin{aligned} &\rho^{-1} \sup_{B_\rho(x')} |\partial_1 u^* - (\partial_1 g)(x')| \\ &\qquad \lesssim r^{-1} \left(\sup_{B_r(x')} |\partial_1 u^* - (\partial_1 g)(x')| + \sup_{B'_r(x')} |\nabla' \partial_1 g| + \sup_{B'_r(x')} |(\nabla')^2 \partial_1 g| \right) . \end{aligned}$$

For $\rho \downarrow 0$ this yields

$$|\partial_1 \sigma^*(x')| \lesssim r^{-1} \left(\sup_{B_r(x')} |\partial_1 u^* - (\partial_1 g)(x')| + \sup_{\Omega'} |(\nabla')^2 g| + \sup_{\Omega'} |(\nabla')^3 g| \right) . \tag{4.38}$$

Now we apply Lemma 4.6 (translated and rescaled) to the harmonic function $u^*(x) - (g(x') + (\partial_1 g)(x')(x_1 - x'_1))$ and get

$$\begin{aligned} &r \sup_{B_r(x')} |\partial_1 u^* - (\partial_1 g)(x')| \\ &\quad \lesssim \sup_{B_{2r}(x')} |u^* - g(x') - (\partial_1 g)(x')(x_1 - x'_1)| + r \sup_{B'_{2r}(x')} |\partial_1 g - (\partial_1 g)(x')| \\ &\quad \lesssim \sup_{B_{2r}(x')} |u^* - g(x')| + r \sup_{\Omega'} |\nabla' g| . \end{aligned} \tag{4.39}$$

Inserting (4.39) in (4.38) yields

$$\begin{aligned} &|\partial_1 \sigma^*(x')| \\ &\lesssim r^{-1} \left(r^{-1} \sup_{B_{2r}(x')} |u^* - g(x')| + \sup_{\Omega'} |\nabla' g| + \sup_{\Omega'} |(\nabla')^2 g| + \sup_{\Omega'} |(\nabla')^3 g| \right) . \end{aligned} \tag{4.40}$$

Using (4.37) with $\rho = r$, we get from (4.40)

$$\begin{aligned}&|\partial_1 \sigma^*(x')| \\ &\lesssim\ r^{-3/2} R^{-1/2+\delta} \left(\sup_{B_1} |u^*| + \sup_{\Omega'} |g| + \sup_{\Omega'} |\nabla' g| + \sup_{\Omega'} |(\nabla')^2 g| + \sup_{\Omega'} |(\nabla')^3 g| \right) \ .\end{aligned}$$

With the definition of G_3 this proves (4.18). □

4.3.1 Three Applications of the Maximum Principle

We use the notations

$$B_1 \ = \ \{x \in \mathbb{R}^3 \mid |x| < 1\} \quad \text{and} \quad B_1' \ = \ B_1 \cap \{x_3 = 0\} \ .$$

Lemma 4.7. *Let u be a harmonic function in $B_1 - \{x_3 = 0\}$ with*

$$u \ \leq \ 1 \quad \text{in } B_1 \ ,$$

$$u(x) \ \leq \ \tfrac{1}{2}(x_1^2 + x_2^2) \quad \text{for } x \in B_1' \ .$$

Then we have

$$u(0,0,x_3) \ \leq \ 3|x_3|$$

for all $-1 \leq x_3 \leq 1$.

Proof of Lemma 4.7.
We start by considering the case $0 \leq x_3 \leq 1$. By assumption we have

$$\left.\begin{array}{ll} u \leq 1 & \text{on } \partial B_1 \cap \{x_3 > 0\} \ , \\ u(x) \leq \frac{1}{2}(x_1^2 + x_2^2) & \text{for } x \in B_1' \end{array}\right\} \ . \tag{4.41}$$

We choose as a suitable comparison function on $B_1 \cap \{x_3 > 0\}$:

$$w(x) \ = \ 3x_3 + x_1^2 + x_2^2 - 2x_3^2 \ .$$

Obviously, w is harmonic. By construction we have for $x_3 = 0$

$$w(x) \ = \ x_1^2 + x_2^2 \ \geq \ \tfrac{1}{2}(x_1^2 + x_2^2) \ \overset{(4.41)}{\geq} \ u(x) \ .$$

Further notice that for $x \in \partial B_1 \cap \{x_3 \geq 0\}$ we have because of $x_3 \geq x_3^2$ the estimate

$$w(x) \ \geq \ 3x_3^2 + x_1^2 + x_2^2 - 2x_3^2 \ = \ 1 \ \overset{(4.41)}{\geq} \ u(x) \ .$$

Hence by the maximum principle $w \geq u$ in $B_1 \cap \{x_3 \geq 0\}$ and thus, in particular,

$$u(0,0,x_3) \ \leq \ w(0,0,x_3) \ \leq \ 3x_3 \ . \tag{4.42}$$

It remains to consider the case $-1 \le x_3 \le 0$. By assumption we have

$$\left.\begin{array}{ll} u \le 1 & \text{on } \partial B_1 \cap \{x_3 < 0\} \ , \\ u(x) \le \frac{1}{2}(x_1^2 + x_2^2) & \text{for } x \in B_1' \end{array}\right\} \ . \tag{4.43}$$

By choosing as comparison function on $B_1 \cap \{x_3 < 0\}$ the function

$$w(x) \ = \ -3x_3 + x_1^2 + x_2^2 - 2x_3^2 \ ,$$

we may conclude as before and yield

$$u(0,0,x_3) \ \le \ w(0,0,x_3) \ \le \ -3x_3$$

for $-1 \le x_3 \le 0$. □

Lemma 4.8. *Let u be harmonic in $B_1 - \{x_3 = 0, x_2 \ge 0\}$ with*

$$u \ \le \ 1 \quad \text{in } B_1 \ ,$$

$$u(x) \ \le \ \tfrac{1}{2}(x_1^2 + x_2^2) \quad \text{for } x \in B_1' \cap \{x_2 \ge 0\} \ .$$

Then we have

$$u(0,x_2,x_3) \ \lesssim \ \left(\sqrt{x_2^2 + x_3^2}\right)^{1/2}$$

for all x_2, x_3 with $x_2^2 + x_3^2 \le 1$.

Proof of Lemma 4.8.
By assumption we have

$$\left.\begin{array}{ll} u \le 1 & \text{on } \partial B_1 \ , \\ u(x) \le \frac{1}{2}(x_1^2 + x_2^2) & \text{for } x \in B_1' \cap \{x_2 \ge 0\} \ . \end{array}\right\} \tag{4.44}$$

For notational convenience, we introduce the distance to the edge

$$r := \sqrt{x_2^2 + x_3^2} \ . \tag{4.45}$$

Our comparison function is

$$w(x) = 6(r - x_2)^{1/2} + x_1^2 + x_2^2 - 2x_3^2 \ .$$

The polynomial contribution is obviously harmonic. That the function $(r - x_2)^{1/2}$ of the two variables (x_2, x_3) is harmonic outside of $\{x_3 = 0, x_2 \ge 0\}$ requires a short calculation. Alternatively, it can be inferred from the representation in polar coordinates

$$\tfrac{1}{\sqrt{2}}(r - x_2)^{1/2} \ = \ r^{1/2} \sin \tfrac{\phi}{2}$$

for $(x_2, x_3) = (r\cos\phi, r\sin\phi)$. This function is also chosen such that it vanishes on $\{x_3 = 0, x_2 \ge 0\}$. Thus we have on $B_1' \cap \{x_2 \ge 0\}$

$$w(x) \ = \ x_1^2 + x_2^2 \ \ge \ \tfrac{1}{2}(x_1^2 + x_2^2) \ \overset{(4.44)}{\ge} \ u(x) \ . \tag{4.46}$$

Furthermore we notice for $x \in B_1$

$$r - x_2 \;=\; \sqrt{x_2^2 + x_3^2} - x_2 \;\geq\; \tfrac{1}{4} x_3^2$$

and thus

$$\sqrt{r - x_2} \;\geq\; \tfrac{1}{2}|x_3| \;,$$

so that for $x \in \partial B_1$

$$\begin{aligned} w(x) \;&\geq\; 3|x_3| + x_1^2 + x_2^2 - 2x_3^2 \\ &\geq\; 3x_3^2 + x_1^2 + x_2^2 - 2x_3^2 \\ &=\; x_1^2 + x_2^2 + x_3^2 \\ &=\; 1 \\ &\overset{(4.44)}{\geq}\; u(x) \end{aligned} \tag{4.47}$$

By the maximum principle, (4.46) and (4.47) propagate into $B_1 - \{x_3 = 0, x_2 \geq 0\}$, so that in particular

$$\begin{aligned} u(0, x_2, x_3) \;&\leq\; w(0, x_2, x_3) \\ &=\; 6(r - x_2)^{1/2} + x_2^2 - 2x_3^2 \\ &\leq\; 6(2r)^{1/2} + r^2 \\ &\leq\; (6\sqrt{2} + 1) r^{1/2} \end{aligned}$$

With the definition of the distance r in (4.45) this proves the lemma. □

Lemma 4.9. *For $\gamma \in (0, \pi)$ let the sector*

$$\mathcal{S} = \{ x \in B_1' \mid x = r(\cos\mu, \sin\mu, 0),\, r \in (0,1),\, \mu \in (0, \gamma) \}$$

be given. Then there exists a universal $\theta < 1$ with the property: for any u which is harmonic in $B_1 - \mathcal{S}$ with

$$u \;\leq\; 1 \quad \text{in } B_1 \qquad \text{and} \qquad u \;\leq\; 0 \quad \text{on } \mathcal{S} \;,$$

we have

$$u \;\leq\; \theta \quad \text{in } B_{1/2} \;.$$

Proof of Lemma 4.9.
We introduce the points

$$x_R \;:=\; R\left(\cos\tfrac{\gamma}{2}, \sin\tfrac{\gamma}{2}, 0\right)$$

along the "diagonal" of the sector $\mathcal{S}$. For $R \leq \frac{1}{2}$ and $R_\gamma := R \sin\frac{\gamma}{2}$ we consider the balls $B_{R_\gamma}(x_R) \subset B_1$. They have the property

$$B_{R_\gamma}(x_R) \cap \mathcal{S} \;=\; B_{R_\gamma}(x_R) \cap \{x_3 = 0\} \;.$$

Now we set

$$c_\gamma \;:=\; \tfrac{1}{12} \sin\tfrac{\gamma}{2} \;.$$

Clearly we have

$$B_{c_\gamma R}(x_R) \;\subset\; B_{R_\gamma/2}(x_R)\;.$$

Let further the point $(x_1, x_2, x_3) \in B_{c_\gamma R}(x_R)$ be given. Then we have

$$B_{R_\gamma/2}(x_1, x_2, 0) \;\subset\; B_{R_\gamma}(x_R)\;,$$

and hence by Lemma 4.7 (after shifting the origin to $(x_1, x_2, 0)$ and rescaling by $R_\gamma/2$)

$$u(x) \;\leq\; 3\frac{|x_3|}{R_\gamma/2} \;\leq\; \tfrac{1}{2}\;, \tag{4.48}$$

where we have used that

$$|x_3| \;\leq\; c_\gamma R \;=\; \tfrac{1}{12} R_\gamma$$

for $x \in B_{c_\gamma R}(x_R)$.

For given $R \leq \frac{1}{2}$ we now construct a comparison function w_R on

$$B_1 \;-\; \big(\mathcal{S} \cup B_{c_\gamma R}(x_R)\big)\;. \tag{4.49}$$

It is given by

$$w_R(x) \;=\; \tfrac{1}{2}\left(1 + \frac{1 - \frac{c_\gamma R}{|x - x_R|}}{1 - \frac{c_\gamma R}{1-R}}\right)\;.$$

Since w_R is an affine transformation of the shifted fundamental solution $|x - x_R|^{-1}$, it is harmonic in $\mathbb{R}^3 - \{x_R\}$ and therefore also in (4.49). By construction we have

$$w_R \;=\; \tfrac{1}{2} \quad \text{on } \partial B_{c_\gamma R}(x_R)\;, \tag{4.50}$$

and $w_R \geq \frac{1}{2}$ in $\mathbb{R}^3 - B_{c_\gamma R}(x_R)$, so that in particular,

$$w_R \;\geq\; 0 \quad \text{on } \mathcal{S} - B_{c_\gamma R}(x_R)\;. \tag{4.51}$$

Finally, for $x \in \partial B_1$ we have

$$|x - x_R| \;\geq\; |x| - |x_R| \;=\; 1 - R\;,$$

so that

$$w_R \;\geq\; 1 \quad \text{on } \partial B_1\;. \tag{4.52}$$

In view of (4.48), (4.50), (4.51) and (4.52) we conclude

$$u \;\leq\; w_R \quad \text{on } \partial\left(B_1 \;-\; \big(\mathcal{S} \cup B_{c_\gamma R}(x_R)\big)\right)\;,$$

and thus by the maximum principle

$$u \;\leq\; w_R \quad \text{in } B_1 - B_{c_\gamma R}(x_R)\;.$$

Together with (4.48) this yields

$$u \;\leq\; \max\{\tfrac{1}{2}, \sup_{B_{1/2}} w_R\} \quad \text{in } B_{1/2}\;. \tag{4.53}$$

It remains to show that there exists an $R \leq \frac{1}{2}$ such that

$$\theta_R \;:=\; \sup_{B_{1/2}} w_R \;<\; 1 \;.$$

We notice that for $x \in B_{1/2}$

$$|x - x_R| \;\leq\; |x| + |x_R| \;\leq\; \tfrac{1}{2} + R \;, \tag{4.54}$$

so that

$$\sup_{B_{1/2}} w_R \;\leq\; \tfrac{1}{2}\left(1 + \frac{1 - \frac{c_\gamma R}{\frac{1}{2}+R}}{1 - \frac{c_\gamma R}{1-R}}\right) \;=\; 1 - \tfrac{1}{2}c_\gamma R + O(R^2) \;.$$

Hence $\theta_R < 1$ for sufficiently small $R > 0$, which proves the lemma. □

4.3.2 Concluding Proofs on Regularity

Proof of Lemma 4.3.
We go through several reductions of the claim so that we can apply Lemma 4.7. It is obvious that it is enough to show (4.22) for all $\rho \leq \frac{1}{2}$. We now argue that it is sufficient to establish

$$\begin{aligned} &u(x_1,x_2,x_3) - g(x_1,x_2) \\ &\lesssim\; |x_3|\left(\sup_{B_{1/2}(x_1,x_2,0)}(u - g(x_1,x_2)) + \sup_{B'_{1/2}(x_1,x_2)}|\nabla' g| + \sup_{B'_{1/2}(x_1,x_2)}|(\nabla')^2 g|\right) \end{aligned} \tag{4.55}$$

for all $(x_1,x_2,x_3) \in B_{1/2}$. Indeed, for any $(x_1,x_2,x_3) \in B_\rho$ with $\rho \leq \frac{1}{2}$ we have

$$\begin{aligned} u(x_1,x_2,x_3) - g(0) \;&\leq\; u(x_1,x_2,x_3) - g(x_1,x_2) + |g(x_1,x_2) - g(0)| \\ &\overset{(4.55)}{\lesssim}\; |x_3|\left(\sup_{B_{1/2}(x_1,x_2,0)}(u - g(x_1,x_2)) + \sup_{B'_{1/2}(x_1,x_2)}|\nabla' g| + \sup_{B'_{1/2}(x_1,x_2)}|(\nabla')^2 g|\right) \\ &\qquad + |g(x_1,x_2) - g(0)| \\ &\lesssim\; |x_3|\left(\sup_{B_{1/2}(x_1,x_2,0)}(u - g(0)) + \sup_{B'_{1/2}(x_1,x_2)}|\nabla' g| + \sup_{B'_{1/2}(x_1,x_2)}|(\nabla')^2 g|\right) \\ &\qquad + \sup_{B'_{1/2}(x_1,x_2)}|g(x_1,x_2) - g(0)| \;, \end{aligned}$$

where we have used the triangle inequality for the supremum in the way

$$\begin{aligned} \sup(u - g(x_1,x_2)) \;&\leq\; \sup(u - g(0)) + \sup(g(0) - g(x_1,x_2)) \\ &\leq\; \sup(u - g(0)) + \sup|g(x_1,x_2) - g(0)| \;. \end{aligned}$$

It remains to notice that $(x_1,x_2,x_3) \in B_\rho$ and $\rho \leq \frac{1}{2}$ imply $|x_3| \leq \rho$, $B_{1/2}(x_1,x_2,0) \subset B_1$, $B'_{1/2}(x_1,x_2) \subset B'_1$ and

$$|g(x_1,x_2) - g(0)| \;\leq\; \rho \sup_{B'_1}|\nabla' g| \;.$$

By translational invariance and rescaling, (4.55) reduces to

$$u(0,0,x_3) - g(0) \;\lesssim\; |x_3| \left(\sup_{B_1} (u - g(0)) + \sup_{B_1'} |\nabla' g| + \sup_{B_1'} |(\nabla')^2 g| \right) \tag{4.56}$$

for all $|x_3| \leq 1$. Since affine functions are harmonic, we may assume

$$g(0) = 0 \quad \text{and} \quad (\nabla' g)(0) = 0 \;, \tag{4.57}$$

so that (4.56) is a consequence of

$$u(0,0,x_3) \;\lesssim\; |x_3| \left(\sup_{B_1} u + \sup_{B_1'} |(\nabla')^2 g| \right) \tag{4.58}$$

for all $|x_3| \leq 1$. By rescaling u and g simultaneously, we may assume

$$\sup_{B_1} u + \sup_{B_1'} |(\nabla')^2 g| \;\leq\; 1 \;, \tag{4.59}$$

so that (4.58) reduces to

$$u(0,0,x_3) \;\lesssim\; |x_3| \tag{4.60}$$

for $|x_3| \leq 1$. In view of (4.57) and (4.59), the function u now satisfies the assumptions of Lemma 4.7, which in turn yields (4.60). □

Proof of Lemma 4.4.
We repeat the reduction of Lemma 4.3: it is enough to show (4.24) for all $\rho \leq \frac{1}{2}$. Moreover, we argue that it is sufficient to establish

$$\begin{aligned} &|u(x_1,x_2,x_3) - g(x_1,0)| \\ &\lesssim \left(\sqrt{x_2^2 + x_3^2} \right)^{1/2} \left(\sup_{B_{1/2}(x_1,0,0)} |u - g(x_1,0)| + \sup_{B'_{1/2}(x_1,0)} |\nabla' g| + \sup_{B'_{1/2}(x_1,0)} |(\nabla')^2 g| \right) \end{aligned} \tag{4.61}$$

for all $(x_1,x_2,x_3) \in B_{1/2}$. Indeed, for any $(x_1,x_2,x_3) \in B_\rho$ with $\rho \leq \frac{1}{2}$ we have

$$\begin{aligned} &|u(x_1,x_2,x_3) - g(x_1,0)| \\ &\overset{(4.61)}{\lesssim} \left(\sqrt{x_2^2 + x_3^2} \right)^{1/2} \left(\sup_{B_{1/2}(x_1,0,0)} |u - g(x_1,0)| + \sup_{B'_{1/2}(x_1,0)} |\nabla' g| + \sup_{B'_{1/2}(x_1,0)} |(\nabla')^2 g| \right) \\ &\qquad + \; |g(x_1,0) - g(0)| \;. \end{aligned}$$

It remains to observe that $(x_1,x_2,x_3) \in B_\rho$ with $\rho \leq \frac{1}{2}$ implies $\left(\sqrt{x_2^2 + x_3^2} \right)^{1/2} \leq \rho^{1/2}$, $B_{1/2}(x_1,0,0) \subset B_1$, $B'_{1/2}(x_1,0) \subset B_1'$ and

$$|g(x_1,0) - g(0)| \;\leq\; \rho \sup_{B_1'} |\nabla' g| \;\leq\; \rho^{1/2} \sup_{B_1'} |\nabla' g| \;.$$

By translational invariance and rescaling, (4.61) reduces to

$$|u(0,x_2,x_3)-g(0)| \;\lesssim\; \left(\sqrt{x_2^2+x_3^2}\right)^{1/2}\left(\sup_{B_1}|u-g(0)|+\sup_{B_1'}|\nabla' g|+\sup_{B_1'}|(\nabla')^2 g|\right) \tag{4.62}$$

for all x_2, x_3 with $x_2^2+x_3^2 \le 1$. By substracting an affine and thus harmonic function, we may assume that

$$g(0)=0 \quad \text{and} \quad (\nabla' g)(0)=0\ ,$$

so that (4.62) reduces to

$$|u(0,x_2,x_3)| \;\lesssim\; \left(\sqrt{x_2^2+x_3^2}\right)^{1/2}\left(\sup_{B_1}|u|+\sup_{B_1'}|(\nabla')^2 g|\right)$$

for all $x_2^2+x_3^2 \le 1$. The same symmetry considerations as in Lemma 4.3 lead to the claim that

$$u(0,x_2,x_3) \;\lesssim\; \left(\sqrt{x_2^2+x_3^2}\right)^{1/2} \tag{4.63}$$

under the assumptions

$$\left.\begin{array}{ll} u\le 1 & \text{on } \partial B_1\ , \\ u(x)\le \frac{1}{2}(x_1^2+x_2^2) & \text{for } x\in B_1'\cap\{x_2\ge 0\}\ . \end{array}\right\}$$

But this is the content of Lemma 4.8. □

Proof of Lemma 4.5.
We may assume $g(0)=0$ and $\delta \le 1$, so it is enough to establish

$$\sup_{B_\rho}|u| \;\lesssim\; \rho^\delta\left(\sup_{B_1}|u|+\sup_{B_1'\cap\{x_2\ge 0,x_1\ge 0\}}|\nabla' g|\right)\ . \tag{4.64}$$

We notice that the function $-u$ satisfies the assumptions of Lemma 4.5 with boundary values $-g$. Since the sign of g does not enter the estimate (4.64), it is a consequence of

$$\sup_{B_\rho} u \;\lesssim\; \rho^\delta\left(\sup_{B_1}|u|+\sup_{B_1'\cap\{x_2\ge 0,x_1\ge 0\}}|\nabla' g|\right)\ . \tag{4.65}$$

We now argue that it is sufficient to show

$$\sup_{B_\rho}\tilde{u} \;\lesssim\; \rho^\delta \sup_{B_1}|\tilde{u}| \tag{4.66}$$

for any $\tilde{u}$ which is harmonic in $B_1-\{x_3=0, x_2\ge 0, x_1\ge 0\}$ and has boundary values $\tilde{u}\le 0$ on $B_1'\cap\{x_2\ge 0, x_1\ge 0\}$. Indeed, if u is harmonic in $B_1-\{x_3=0, x_2\ge 0, x_1\ge 0\}$ with boundary values g on $B_1'\cap\{x_2\ge 0, x_1\ge 0\}$, we define the function $\tilde{u}$ for all $(x_1,x_2,x_3)\in B_1$ by

$$\tilde{u}(x_1,x_2,x_3) \;:=\; u(x_1,x_2,x_3)-C_0(x_1+x_2), \tag{4.67}$$

where

$$C_0 \;:=\; \sup_{B_1' \cap \{x_2 \geq 0, x_1 \geq 0\}} |\nabla' g| \;.$$

Obviously $\tilde{u}$ is harmonic in $B_1 - \{x_3 = 0, x_2 \geq 0, x_1 \geq 0\}$ and for all $x_1 \geq 0, x_2 \geq 0$ with $\sqrt{x_1^2 + x_2^2} < 1$ we have

$$\tilde{u}(x_1, x_2, 0) \;=\; u(x_1, x_2, 0) - C_0(x_1 + x_2) \;\leq\; u(x_1, x_2, 0) - C_0\sqrt{x_1^2 + x_2^2} \;\leq\; 0 \;, \quad (4.68)$$

since $u = g$ on $B_1' \cap \{x_2 \geq 0, x_1 \geq 0\}$ and $g(0) = 0$. Therefore $\tilde{u} \leq 0$ on $B_1' \cap \{x_2 \geq 0, x_1 \geq 0\}$ and (4.65) now follows from (4.66):

$$\begin{aligned} u \;&=\; \tilde{u} + (x_1 + x_2)\, C_0 \\ &\overset{(4.66)}{\lesssim}\; \rho^\delta \sup_{B_1} |\tilde{u}| + \rho\, C_0 \\ &\overset{(4.67)}{\lesssim}\; \rho^\delta \left(\sup_{B_1} |u| + C_0 \right) + \rho\, C_0 \\ &\lesssim\; \rho^\delta \left(\sup_{B_1} |u| + C_0 \right) \;. \end{aligned}$$

It remains to proof (4.66). It is well known that the exponent δ in (4.66) can be characterized as the smallest eigenvalue of the Laplace–Beltrami operator on ∂B_1 with non–positive boundary conditions on the quarter arc $\partial B_1' \cap \{x_2 \geq 0, x_1 \geq 0\}$. We give here an independent and elementary argument that relies on Lemma 4.9.

It is enough to show that there exists a universal $\theta < 1$ such that for any $\tilde{u}$, which is harmonic in $B_1 - \{x_3 = 0, x_2 \geq 0, x_1 \geq 0\}$ and has boundary values $\tilde{u} \leq 0$ on $B_1' \cap \{x_2 \geq 0, x_1 \geq 0\}$, there holds

$$\sup_{B_{1/2}} \tilde{u} \;\leq\; \theta \sup_{B_1} \tilde{u} \;. \quad (4.69)$$

Indeed, by scaling this implies for any $k \in \mathbb{N}$

$$\sup_{B_{2^{-k}}} \tilde{u} \;\leq\; \theta \sup_{B_{2^{-k+1}}} \tilde{u} \;,$$

and thus by iteration

$$\sup_{B_{2^{-k}}} \tilde{u} \;\leq\; \theta^k \sup_{B_1} \tilde{u} \;.$$

With $\delta := -\log\theta / \log 2 > 0$, the latter can be rewritten as

$$\sup_{B_{2^{-k}}} \tilde{u} \;\leq\; (2^{-k})^\delta \sup_{B_1} \tilde{u} \;,$$

which yields for $x \in B_{1/2}$

$$\tilde{u}(x) \;\leq\; (2|x|)^\delta \sup_{B_1} \tilde{u} \;.$$

By scaling, it is enough to consider the case

$$\sup_{B_1} \tilde{u} \;=\; 1 \tag{4.70}$$

and to show

$$\tilde{u} \;\leq\; \theta \quad \text{ on } B_{1/2}\;. \tag{4.71}$$

Now $\tilde{u}$ satisfies the assumptions of Lemma 4.9, and (4.71) follows thereby. □

Proof of Lemma 4.6.
By symmetry, it is sufficient to show

$$\sup_{B_{1/2}} |\partial_1 u| \;\lesssim\; \sup_{B_1} |u| + \sup_{B_1'} |\partial_1 g|\;.$$

We use that

$$\partial_1 u \quad \text{is harmonic in} \quad B_1 - \{x_3 = 0\}, \tag{4.72}$$

$$\partial_1 u = \partial_1 g \qquad \text{on} \qquad \{x_3 = 0\}. \tag{4.73}$$

We apply Bernstein's argument. Fix a cut–off function $\eta \in C_0^\infty(B_1)$ with $\eta = 1$ on $B_{1/2}$ and consider for a constant $\lambda > 0$

$$w \;:=\; \eta^2(\partial_1 u)^2 - \lambda u^2\;.$$

By construction of η and by (4.73),

$$w \;\leq\; 0 \quad \text{ on } \quad \partial B_1 \cap \{x_3 \geq 0\}\;, \tag{4.74}$$

$$w \;\leq\; \sup_{B_1'} |\partial_1 g|^2 \quad \text{ on } \quad \overline{B}_1 \cap \{x_3 = 0\}\;. \tag{4.75}$$

We claim that for $\lambda = \lambda(\eta)$ sufficiently large

$$-\Delta w \;\leq\; 0. \tag{4.76}$$

Indeed

$$\begin{aligned}
-\Delta w \;&=\; -\eta^2\Delta(\partial_1 u)^2 - 4\eta\nabla\eta\cdot\nabla(\partial_1 u)^2 - \Delta\eta^2(\partial_1 u)^2 - \lambda\Delta u^2 \\
&\overset{(4.72)}{=}\; -2\eta^2|\nabla\partial_1 u|^2 - 8\eta\partial_1 u\nabla\eta\cdot\nabla\partial_1 u - \Delta\eta^2(\partial_1 u)^2 - 2\lambda|\nabla u|^2 \\
&\leq\; 8(\partial_1 u)^2|\nabla\eta|^2 - \Delta\eta^2(\partial_1 u)^2 - 2\lambda|\nabla u|^2 \\
&\leq\; (8|\nabla\eta|^2 + |\Delta\eta^2| - 2\lambda)\;|\nabla u|^2,
\end{aligned}$$

so that (4.76) holds provided $\lambda \geq 4|\nabla\eta|^2 + \frac{1}{2}|\Delta\eta^2|$. By the maximum principle we obtain from (4.76) and (4.74)

$$w \;\leq\; \sup_{B_1'} |\partial_1 g|^2 \quad \text{ in } B_1,$$

that is

$$\eta^2(\partial_1 u)^2 \;\le\; \lambda u^2 + \sup_{B_1'} |\partial_1 g|^2 \;\lesssim\; (\sup_{B_1} |u|)^2 + \sup_{B_1'} |\partial_1 g|^2 \quad \text{in } B_1.$$

By construction of η this yields as desired

$$(\partial_1 u)^2 \;\lesssim\; (\sup_{B_1} |u|)^2 + \sup_{B_1'} |\partial_1 g|^2 \quad \text{in } B_{1/2}.$$

□

Remark 4.2. *The corner angles of the polygonal boundary $\partial\Omega'$ enter our regularity theory only via Lemma 4.9, which propagates into Lemma 4.5 and finally into Theorem 4.1. Since Lemma 4.9 is established for general corner angles $\gamma \in (0, \pi)$, the statements of Theorem 4.1 hold analogously for arbitrary convex polygonal domains.*

4.4 A–priori Error Estimate

We consider a triangulation of type $\mathcal{T}_h$ on Ω' with typical triangle diameter h. The divergence–conforming finite element ansatz for the magnetization m' with Raviart–Thomas elements leads on the level of σ to the space $P^0_{0,h}$ of all piecewise constant σ_h's with vanishing mean $\int_{\Omega'} \sigma_h dx' = 0$ (which we extend trivially on $\mathbb{R}^2$). Hence we are investigating the following Galerkin ansatz for (4.11):

$$\begin{aligned} &\text{Minimize} \\ &\quad E(\sigma_h) \;=\; \tfrac{1}{2} \int_{\mathbb{R}^2} |(\nabla')^{-1/2} \sigma_h|^2 dx' + 2 \int_{\Omega'} H'_{ext} \cdot x' \, \sigma_h \, dx' \qquad (4.77) \\ &\text{among all } \sigma_h \in P^0_{0,h}. \end{aligned}$$

We now formulate our estimate of the discretization error.

Theorem 4.2. *Let $\Omega' = (-\frac{1}{2}, \frac{1}{2})^2$ and $0 < h, \alpha < 1$. Let the triangulation $\mathcal{T}_h$ of Ω' satisfy*

$$\forall T \in \mathcal{T}_h \quad \operatorname{diam}(T) \;\le\; h \operatorname{dist}(x'_T, \partial\Omega')^\alpha, \qquad (4.78)$$

where x'_T denotes the barycenter of T. Then there exists a constant C, which only depends on α, such that we have for the solutions σ^* and σ^*_h of (4.11) resp. (4.77)

$$\left(\int_{\mathbb{R}^2} |(\nabla')^{-1/2} (\sigma^*_h - \sigma^*)|^2 dx' \right)^{1/2} \;\le\; C \, |H'_{ext}| \left\{ \begin{array}{ll} h^{3/2} & \text{for } \alpha > \frac{2}{3} \\ (\log^{1/2} \frac{1}{h}) h^{\frac{1}{2(1-\alpha)}} & \text{for } \alpha < \frac{2}{3} \end{array} \right\}. \qquad (4.79)$$

Proof of Theorem 4.2.
We denote by C a generic constant which only depends on α. In view of (4.11) and (4.77), the disrectization error in the energy norm is given by the approximation error. It thus suffices to show

$$\left(\int_{\mathbb{R}^2} |(\nabla')^{-1/2} (I\sigma^* - \sigma^*)|^2 dx' \right)^{1/2} \;\le\; C \, |H'_{ext}| \left\{ \begin{array}{l} h^{3/2} \\ (\log \frac{1}{h}) h^{\frac{1}{2(1-\alpha)}} \end{array} \right\}, \qquad (4.80)$$

where the interpolation $I\sigma \in P^0_{0,h}$ is defined via

$$\forall\, T \in \mathcal{T}_h \quad \int_T I\sigma \, dx' \;=\; \int_T \sigma \, dx'.$$

In view of (2.8), i. e.

$$\left(\tfrac{1}{2} \int_{\mathbb{R}^2} |(\nabla')^{-1/2}(I\sigma^* - \sigma^*)|^2 dx' \right)^{\frac{1}{2}} \;=\; \sup \left\{ \frac{\int_{\Omega'} (I\sigma^* - \sigma^*)\, u \, dx'}{(\int_{\mathbb{R}^3} |\nabla u|^2 dx)^{1/2}} \mid u \colon \mathbb{R}^3 \to \mathbb{R} \right\},$$

(4.80) amounts to show

$$\begin{aligned} &\left| \sum_{T \in \mathcal{T}_h} \int_T (I\sigma^* - \sigma^*)\, (Iu - u)\, dx' \right| \\ &\quad = \; \left| \int_{\Omega'} (I\sigma^* - \sigma^*)\, (Iu - u)\, dx' \right| \\ &\quad = \; \left| \int_{\Omega'} (I\sigma^* - \sigma^*)\, u \, dx' \right| \\ &\quad \leq \; C\, |H'_{ext}| \left(\int_{\mathbb{R}^3} |\nabla u|^2 \, dx \right)^{1/2} \left\{ \begin{array}{l} h^{\frac{3}{2}} \\ (\log \tfrac{1}{2}\, \tfrac{1}{h}) h^{\frac{1}{2(1-\alpha)}} \end{array} \right\} \end{aligned} \tag{4.81}$$

for an arbitrary test function u.

We will need the following trace estimate for u on each triangle T with area $|T|$ and for exponents $p \in \{2, 4\}$

$$\left(\int_T |u - Iu|^p dx' \right)^{1/p} \;\leq\; C\, \frac{\operatorname{diam}(T)^{1/2}}{|T|^{1/2 - 1/p}} \left(\int_{T \times \mathbb{R}} |\nabla u|^2 dx \right)^{1/2}. \tag{4.82}$$

Indeed, let $\hat{T}$ be the reference triangle on which we are sure to have the estimate, which is a mixture of a Sobolev estimate, a trace estimate (recall that $H^1(\mathbb{R}^3)$ embeds into $L^4(\mathbb{R}^2)$) and a Poincaré estimate:

$$\left(\int_{\hat{T}} |u - Iu|^p d\hat{x}' \right)^{1/p} \;\leq\; C \left(\int_{\hat{T} \times \mathbb{R}} |\hat{\nabla} u|^2 d\hat{x} \right)^{1/2} \tag{4.83}$$

with a universal constant C. Let $\hat{x}' \mapsto A\hat{x}' + b$ be the affine map which maps $\hat{T}$ onto T. We change coordinates $x = (x', x_3)$ according to

$$\begin{array}{rcl@{\qquad}rcl} x' &=& A\hat{x}', & \hat{\nabla}' &=& A^t \nabla', \\ x_3 &=& |A^t| \hat{x}_3, & \hat{\partial}_3 &=& |A^t|\, \partial_3. \end{array} \tag{4.84}$$

Then we have

$$\begin{aligned}
&\left(\int_T |u - Iu|^p dx'\right)^{1/p} \\
&\quad = \left(|\mathrm{det}A| \int_{\hat{T}} |u - Iu|^p d\hat{x}'\right)^{1/p} \\
&\quad \overset{(4.83)}{\leq} C\,|\mathrm{det}A|^{1/p} \left(\int_{\hat{T}\times\mathbb{R}} |\hat{\nabla}' u|^2 + |\hat{\partial}_3 u|^2 d\hat{x}\right)^{1/2} \\
&\quad \overset{(4.84)}{\leq} C\,|\mathrm{det}A|^{1/p} \left(|A^t|^2 \int_{\hat{T}\times\mathbb{R}} |\nabla' u|^2 + |\partial_3 u|^2 d\hat{x}\right)^{1/2} \\
&\quad = C\,|\mathrm{det}A|^{1/p} \left(|A^t|\,|\mathrm{det}A|^{-1} \int_{T\times\mathbb{R}} |\nabla' u|^2 + |\partial_3 u|^2 dx\right)^{1/2} \\
&\quad = C\,|\mathrm{det}A|^{1/p-1/2} |A|^{1/2} \left(\int_{T\times\mathbb{R}} |\nabla' u|^2 + |\partial_3 u|^2 dx\right)^{1/2}.
\end{aligned}$$

Now (4.82) follows because of $\frac{1}{2}\,|\mathrm{detA}| = |T|$ and $|A| \leq C\,\mathrm{diam}(T)$.

We will distinguish between interior and boundary triangles.

- Interior triangles T are those for which

$$\mathrm{dist}(x'_T, \partial\Omega') \;\geq\; (2h)^{\frac{1}{1-\alpha}}. \tag{4.85}$$

  Those triangles satisfy in particular

$$\mathrm{diam}(T) \overset{(4.78)}{\leq} h\,\mathrm{dist}(x'_T, \partial\Omega')^\alpha \overset{(4.85)}{\leq} \tfrac{1}{2}\mathrm{dist}(x'_T, \partial\Omega'), \tag{4.86}$$

  so that

$$\forall x' \in T \quad \tfrac{1}{2}\mathrm{dist}(x'_T, \partial\Omega') \;\leq\; \mathrm{dist}(x', \partial\Omega') \;\leq\; 2\mathrm{dist}(x'_T, \partial\Omega'). \tag{4.87}$$

  These triangles furthermore have the property that

$$\mathrm{dist}(T, \partial\Omega') \overset{(4.86)}{\geq} \tfrac{1}{2}\mathrm{dist}(x'_T, \partial\Omega') \overset{(4.85)}{\geq} h^{\frac{1}{1-\alpha}},$$

  so that

$$T \;\subset\; \{x' \in \Omega' \mid \mathrm{dist}(x', \partial\Omega') \geq h^{\frac{1}{1-\alpha}}\} \;=:\; \Omega'_h. \tag{4.88}$$

- Boundary triangles T are those for which (4.85) fails, i.e.

$$\mathrm{dist}(x'_T, \partial\Omega') \;<\; (2h)^{\frac{1}{1-\alpha}}. \tag{4.89}$$

  Since

$$\mathrm{diam}(T) \overset{(4.78)}{\leq} h\,\mathrm{dist}(x'_T, \partial\Omega')^\alpha \overset{(4.89)}{\leq} (2h)^{\frac{1}{1-\alpha}},$$

it follows from (4.89) that

$$\forall x' \in T \quad \operatorname{dist}(x', \partial\Omega') \;\le\; (4h)^{\frac{1}{1-\alpha}}.$$

We retain

$$T \;\subset\; \{x' \in \Omega' \mid \operatorname{dist}(x', \partial\Omega') \le (4h)^{\frac{1}{1-\alpha}}\} \;=:\; \partial\Omega'_h. \tag{4.90}$$

We call $\mathcal{T}_{h,\mathrm{int}}$, $\mathcal{T}_{h,\mathrm{bdry}}$ the partitioning of $\mathcal{T}_h$.
We start with an interior triangle $T \in \mathcal{T}_{h,\mathrm{int}}$. By Cauchy–Schwarz inequality

$$\left|\int_T (I\sigma^* - \sigma^*)(Iu - u)\, dx'\right| \;\le\; \left(\int_T |I\sigma^* - \sigma^*|^2\, dx'\right)^{1/2} \left(\int_T |Iu - u|^2\, dx'\right)^{1/2}. \tag{4.91}$$

For the first factor, we use Poincaré's estimate for a convex set T

$$\left(\int_T |I\sigma^* - \sigma^*|^2\, dx'\right)^{\frac{1}{2}} \;\le\; C\, \left(\operatorname{diam}(T)^2 \int_T |\nabla\sigma^*|^2\, dx'\right)^{1/2}$$

and appeal to Theorem 4.1

$$\left(\int_T |\nabla\sigma^*|^2\, dx'\right)^{1/2} \;\le\; C\, |H'_{ext}| \left(\int_T \operatorname{dist}(x', \partial\Omega')^{-3} \operatorname{dist}(x', P)^{-1}\, dx'\right)^{1/2},$$

where $P = \{(\frac{1}{2}, \frac{1}{2}), (\frac{1}{2}, -\frac{1}{2}), (-\frac{1}{2}, \frac{1}{2}), (-\frac{1}{2}, -\frac{1}{2})\}$ denotes the set of corners.
For the second factor in (4.91), we use (4.82) for $p = 2$:

$$\left(\int_T |Iu - u|^2\, dx'\right)^{1/2} \;\le\; C\, \left(\operatorname{diam}(T) \int_{T\times\mathbb{R}} |\nabla u|^2\, dx\right)^{1/2}.$$

The combination yields

$$\begin{aligned}&\left|\int_T (I\sigma^* - \sigma^*)(Iu - u)\, dx'\right| \\ &\quad\le\; C|H'_{ext}| \left(\operatorname{diam}(T)^3 \int_T \operatorname{dist}(x', \partial\Omega')^{-3} \operatorname{dist}(x', P)^{-1}\, dx' \int_{T\times\mathbb{R}} |\nabla u|^2\, dx\right)^{1/2}.\end{aligned} \tag{4.92}$$

We now observe

$$\begin{aligned}&\operatorname{diam}(T)^3 \int_T \operatorname{dist}(x', \partial\Omega')^{-3} \operatorname{dist}(x', P)^{-1}\, dx' \\ &\qquad\overset{(4.78)}{\le}\; h^3 \operatorname{dist}(x'_T, \partial\Omega')^{3\alpha} \int_T \operatorname{dist}(x', \partial\Omega')^{-3} \operatorname{dist}(x', P)^{-1}\, dx' \\ &\qquad\overset{(4.87)}{\le}\; C\, h^3 \int_T \operatorname{dist}(x', \partial\Omega')^{3(\alpha-1)} \operatorname{dist}(x', P)^{-1}\, dx'.\end{aligned}$$

Thus (4.92) turns into

$$\left|\int_T (I\sigma^* - \sigma^*)(Iu - u)\, dx'\right| \\ \leq C|H'_{ext}|\, h^{3/2} \left(\int_T \mathrm{dist}(x', \partial\Omega')^{3(\alpha-1)} \mathrm{dist}(x', P)^{-1}\, dx' \int_{T\times\mathbb{R}} |\nabla u|^2\, dx\right)^{1/2}. \quad (4.93)$$

Cauchy–Schwarz yields in view of (4.88)

$$\left|\sum_{T\in\mathcal{T}_{h,\mathrm{int}}} \int_T (I\sigma^* - \sigma^*)(Iu - u)\, dx'\right| \\ \overset{(4.88)}{\leq} C|H'_{ext}|\, h^{3/2} \left(\int_{\Omega'_h} \mathrm{dist}(x', \partial\Omega')^{3(\alpha-1)} \mathrm{dist}(x', P)^{-1}\, dx' \int_{\mathbb{R}^3} |\nabla u|^2\, dx\right)^{1/2}. \quad (4.94)$$

Hence we are lead to discuss the scaling of the singular integral

$$\int_{\Omega'_h} \mathrm{dist}(x', \partial\Omega')^{3(\alpha-1)} \mathrm{dist}(x', P)^{-1}\, dx' \quad (4.95)$$

in h. By symmetry, it is enough to consider one eighth of Ω'_h, say $\Omega'_h \cap (-\frac{1}{2}, 0)^2 \cap \{x_1 > x_2\}$. After translation of the corner $(-\frac{1}{2}, -\frac{1}{2})$ into $(0,0)$, we have

$$\mathrm{dist}(x', \partial\Omega') = x_2 \quad \text{and} \quad \mathrm{dist}(x', P) \geq x_1\ , \quad (4.96)$$

so that we need to consider

$$\int_{h^{\frac{1}{1-\alpha}}}^{1/2} \int_{h^{\frac{1}{1-\alpha}}}^{x_1} x_2^{3(\alpha-1)} x_1^{-1}\, dx_2\, dx_1 \ = \ \int_{h^{\frac{1}{1-\alpha}}}^{1/2} x_1^{-1} \int_{h^{\frac{1}{1-\alpha}}}^{x_1} x_2^{3(\alpha-1)}\, dx_2\, dx_1.$$

We notice

$$\int_{h^{\frac{1}{1-\alpha}}}^{x_1} x_2^{3(\alpha-1)}\, dx_2 \ \leq \ C \left\{ \begin{array}{ll} x_1^{3\alpha-2} & \alpha > \frac{2}{3} \\ h^{\frac{3\alpha-2}{1-\alpha}} & \alpha < \frac{2}{3} \end{array} \right\}.$$

Hence we obtain for (4.95)

$$\int_{\Omega'_h} \mathrm{dist}(x', \partial\Omega')^{3(\alpha-1)} \mathrm{dist}(x', P)^{-1}\, dx' \ \leq \ C \left\{ \begin{array}{l} 1 \\ (\log \frac{1}{h}) h^{\frac{3\alpha-2}{1-\alpha}} \end{array} \right\}.$$

We use this in (4.94):

$$\left|\sum_{T\in\mathcal{T}_{h,\mathrm{int}}} \int_T (I\sigma^* - \sigma^*)(Iu - u)\, dx'\right| \\ \leq C|H'_{ext}| \left(\int_{\mathbb{R}^3} |\nabla u|^2\, dx\right)^{1/2} \left\{ \begin{array}{ll} h^{3/2} & \text{for } \alpha > \frac{2}{3} \\ (\log^{1/2} \frac{1}{h}) h^{\frac{1}{2(1-\alpha)}} & \text{for } \alpha < \frac{2}{3} \end{array} \right\}. \quad (4.97)$$

We now turn to a boundary triangle $T \in \mathcal{T}_{h,\mathrm{bdry}}$. We start with Hölder's inequality

$$\begin{aligned}
&\left| \int_T (I\sigma^* - \sigma^*)(Iu - u)\, dx' \right| \\
&\quad \le \left(\int_T |I\sigma^* - \sigma^*|^{4/3}\, dx' \right)^{3/4} \left(\int_T |Iu - u|^4\, dx' \right)^{1/4} \\
&\quad \le 2 \left(\int_T |\sigma^*|^{4/3}\, dx' \right)^{3/4} \left(\int_T |Iu - u|^4\, dx' \right)^{1/4}.
\end{aligned}$$

For the first factor, we appeal to Theorem 4.1. For the second factor, we evoke the trace estimate (4.82) with $p = 4$. This yields

$$\begin{aligned}
&\left| \int_T (I\sigma^* - \sigma^*)(Iu - u)\, dx' \right| \\
&\quad \le C\, |H'_{ext}| \left(\int_T \mathrm{dist}(x', \partial\Omega')^{-2/3} \mathrm{dist}(x', P)^{-2/3}\, dx' \right)^{3/4} \\
&\quad \times \frac{\mathrm{diam}(T)^{1/2}}{|T|^{1/4}} \left(\int_{T\times\mathbb{R}} |\nabla u|^2\, dx \right)^{1/2}. \qquad (4.98)
\end{aligned}$$

We now need the following reverse Hölder estimate

$$\begin{aligned}
&\int_T \mathrm{dist}(x', \partial\Omega')^{-2/3} \mathrm{dist}(x', P)^{-2/3}\, dx' \\
&\quad \times \left(\int_T \mathrm{dist}(x', \partial\Omega')\, dx' \right)^{2/3} \left(\int_T \mathrm{dist}(x', P)\, dx' \right)^{2/3} \\
&\quad \le C\, |T|^{7/3}. \qquad (4.99)
\end{aligned}$$

By symmetry, it is enough to consider triangles T in $\Omega' \cap (-\frac{1}{2}, 0)^2 \cap \{x_1 > x_2\}$. After translation of the corner $(-\frac{1}{2}, -\frac{1}{2})$ into $(0, 0)$, we have

$$\mathrm{dist}(x', \partial\Omega') = x_2 \quad \text{and} \quad x_1 \le \mathrm{dist}(x', P) \le 2x_1\ , \qquad (4.100)$$

so that we need to show

$$\left(\int_T x_2^{-2/3}\, x_1^{-2/3}\, dx' \right) \left(\int_T x_2\, dx' \right)^{2/3} \left(\int_T x_1\, dx' \right)^{2/3} \le C\, |T|^{7/3}. \qquad (4.101)$$

The worst case is when T lies in the corner $(0, 0)$, i. e. when T is half of the rectangle $(0, \ell_1) \times (0, \ell_2)$. In this case (4.101) follows from

$$\begin{aligned}
\int_T x_2^{-2/3}\, x_1^{-2/3}\, dx' &\le \int_0^{\ell_1} x_1^{-2/3} dx_1 \int_0^{\ell_2} x_2^{-2/3} dx_2 \le C\, \ell_1^{1/3} \ell_2^{1/3}, \\
\int_T x_2\, dx' &\le \ell_1 \int_0^{\ell_2} x_2\, dx_2 \le C \ell_1 \ell_2^2, \\
\int_T x_1\, dx' &\le \ell_2 \int_0^{\ell_1} x_1\, dx_1 \le C \ell_1^2 \ell_2, \\
|T| &= \frac{1}{2}\, \ell_1\, \ell_2.
\end{aligned}$$

We also need the following consequence of the standard Hölder inequality:

$$|T|^{3-\alpha}\left(\int_T \operatorname{dist}(x',\partial\Omega')\,dx'\right)^{\alpha-1}\left(\int_T \operatorname{dist}(x',P)\,dx'\right)^{-1} \\ \leq \int_T \operatorname{dist}(x',\partial\Omega')^{\alpha-1}\operatorname{dist}(x',P)^{-1}\,dx'. \tag{4.102}$$

Indeed (4.102) can be reformulated as

$$\begin{aligned}|T| \;&\leq\; \left(\int_T \operatorname{dist}(x',\partial\Omega')^{\alpha-1}\operatorname{dist}(x',P)^{-1}\,dx'\right)^{\frac{1}{3-\alpha}} \\ &\quad\times\left(\int_T \operatorname{dist}(x',\partial\Omega')\,dx'\right)^{\frac{1-\alpha}{3-\alpha}}\left(\int_T \operatorname{dist}(x',P)\,dx'\right)^{\frac{1}{3-\alpha}},\end{aligned}$$

which follows from Hölder's inequality by writing

$$1 \;=\; \operatorname{dist}(x',\partial\Omega')^{\frac{\alpha-1}{3-\alpha}}\operatorname{dist}(x',P)^{\frac{-1}{3-\alpha}}\;\operatorname{dist}(x',\partial\Omega')^{\frac{1-\alpha}{3-\alpha}}\;\operatorname{dist}(x',P)^{\frac{1}{3-\alpha}}.$$

We now use (4.78) in form of

$$\operatorname{diam}(T) \;\leq\; Ch\left(|T|^{-1}\int_T \operatorname{dist}(x',\partial\Omega')\,dx'\right)^{\alpha}$$

and the reverse Hölder estimate (4.99) in (4.98). This yields

$$\begin{aligned}&\left|\int_T (I\sigma^*-\sigma^*)(Iu-u)\,dx'\right| \\ &\quad\leq\; C\,|H'_{ext}|\left[|T|^{7/3}\left(\int_T \operatorname{dist}(x',\partial\Omega')\,dx'\right)^{-2/3}\left(\int_T \operatorname{dist}(x',P)\,dx'\right)^{-2/3}\right]^{3/4} \\ &\quad\times|T|^{-1/4}\left[h\left(|T|^{-1}\int_T \operatorname{dist}(x',\partial\Omega')\,dx'\right)^{\alpha}\right]^{1/2}\left(\int_{T\times\mathbb{R}}|\nabla u|^2\,dx\right)^{1/2} \\ &\quad=\; C\,|H'_{ext}|\,h^{1/2}\Big[|T|^{3-\alpha}\left(\int_T \operatorname{dist}(x',\partial\Omega')\,dx'\right)^{\alpha-1}\left(\int_T \operatorname{dist}(x',P)\,dx'\right)^{-1}\Big]^{1/2} \\ &\quad\times\left(\int_{T\times\mathbb{R}}|\nabla u|^2\,dx\right)^{1/2}.\end{aligned}$$

We now apply to the above the Hölder inequality (4.102):

$$\begin{aligned}&\left|\int_T (I\sigma^*-\sigma^*)(Iu-u)\,dx'\right| \\ &\quad\leq\; C\,|H'_{ext}|\,h^{1/2}\left(\int_T \operatorname{dist}(x',\partial\Omega')^{\alpha-1}\operatorname{dist}(x',P)^{-1}\,dx'\right)^{1/2} \\ &\quad\times\left(\int_{T\times\mathbb{R}}|\nabla u|^2\,dx\right)^{1/2}.\end{aligned} \tag{4.103}$$

Finally, we sum (4.103) over all $T \in \mathcal{T}_{h,bdry}$. In view of (4.90), this yields by Cauchy–Schwarz

$$\begin{aligned}
&\left| \sum_{T \in \mathcal{T}_{h,bdry}} \int_T (I\sigma^* - \sigma^*)(Iu - u)\, dx' \right| \\
&\quad \leq C\, |H'_{ext}|\, h^{1/2} \left(\int_{\partial\Omega'_h} \mathrm{dist}(x', \partial\Omega')^{\alpha-1} \mathrm{dist}(x', P)^{-1}\, dx' \right)^{1/2} \\
&\quad \times \left(\int_{\mathbb{R}^3} |\nabla u|^2\, dx \right)^{1/2}. \qquad (4.104)
\end{aligned}$$

Hence we need to discuss

$$\int_{\partial\Omega'_h} \mathrm{dist}(x', \partial\Omega')^{\alpha-1} \mathrm{dist}(x', P)^{-1}\, dx'. \qquad (4.105)$$

Analogously to (4.95) we see that (4.105) behaves as

$$\begin{aligned}
&\int_0^{1/2} \int_0^{\min\{h^{\frac{1}{1-\alpha}}, x_1\}} x_2^{\alpha-1} x_1^{-1}\, dx_2\, dx_1 \\
&\quad = \int_0^{1/2} \alpha^{-1} \min\{h^{\frac{\alpha}{1-\alpha}}, x_1^\alpha\}\, x_1^{-1}\, dx_1 \\
&\quad \leq C(\log \frac{1}{h})\, h^{\frac{\alpha}{1-\alpha}}.
\end{aligned}$$

Therefore (4.104) turns into

$$\begin{aligned}
&\left| \sum_{T \in \mathcal{T}_{h,bdry}} \int_T (I\sigma^* - \sigma^*)(Iu - u)\, dx' \right| \\
&\quad \leq C\, |H'_{ext}| \left((\log \frac{1}{h})\, h^{\frac{1}{1-\alpha}} \right)^{1/2} \left(\int_{\mathbb{R}^3} |\nabla u|^2\, dx \right)^{1/2}. \qquad (4.106)
\end{aligned}$$

Since $\frac{1}{2(1-\alpha)} > \frac{3}{2}$ for $\alpha > \frac{2}{3}$, (4.81) follows from combining (4.97) with (4.106).

□

4.5 A–priori Refined Triangulation and Complexity Considerations

The numerical analysis from Section 4.4 suggests to consider triangulations $\mathcal{T}_h$ which are refined at the boundary according to

$$\mathrm{diam}(T) \sim h\ \mathrm{dist}(x'_T, \partial\Omega')^\alpha, \qquad (4.107)$$

where

- $\mathrm{diam}(T)$ denotes the diameter of a triangle T and $|T|$ its area,
- $\mathrm{dist}(x'_T, \partial\Omega')$ denotes the distance of the barycenter x'_T of T to the boundary $\partial\Omega'$.

Estimate (4.14) suggests to consider triangulations which are regular in the sense of

$$|T| \sim \mathrm{diam}(T)^2. \tag{4.108}$$

Given $h > 0$, we use the following algorithm to generate $\mathcal{T}_h$ with properties (4.107) and (4.108):

- We start from a uniform triangulation $\mathcal{Q}_h$ of mesh size h, see Section 3.4.
- Then we mark all triangles which do not satisfy (4.107). The marked triangles are divided into four subtriangles of the same shape; this preserves (4.108). Neighboring triangles are divided so that the triangulation property is restored.
- This procedure is repeated until all triangles meet (4.107).

The algorithm produces evidently a triangulation of the type $\mathcal{T}_h$ introduced in Section 3.4. Figure 4.9 in Section 4.6 shows an example of such a locally refined triangulation with property (4.107).

We now work out how the number of triangles scales in h, depending on α. We find that there is a cross–over at $\alpha = \frac{1}{2}$.

Lemma 4.10. *For any constants $\Lambda \geq 1$ and $0 \leq \alpha_0 < 1$ there exists a constant $C = C(\Lambda, \alpha_0) < \infty$ with the following property: Let $0 \leq \alpha \leq \alpha_0$, $0 < h \leq \frac{1}{4}$ and triangulations $\mathcal{T}_h$ of $\Omega' = (0,1)^2$, which are refined towards the boundary in the sense of*

$$\forall T \in \mathcal{T}_h \quad \mathrm{diam}(T) \;\leq\; h\,\mathrm{dist}(x'_T, \partial\Omega')^\alpha \;\leq\; \Lambda\,\mathrm{diam}(T) \tag{4.109}$$

and regular in the sense of

$$\forall T \in \mathcal{T}_h \quad \mathrm{diam}(T)^2 \;\leq\; \Lambda\,|T| \tag{4.110}$$

be arbitrary. Then the number $\#\mathcal{T}_h$ of triangles scales as

$$\tfrac{1}{C}\#\mathcal{T}_h \;\leq\; \left\{ \begin{array}{llll} \frac{1}{1-2\alpha}h^{-2} & for & h \leq e^{-\frac{1}{|1-2\alpha|}} & and \quad \alpha < \frac{1}{2} \\ (\log\frac{1}{h^2})h^{-2} & for & h \geq e^{-\frac{1}{|1-2\alpha|}} & or \quad \alpha = \frac{1}{2} \\ \frac{1}{2\alpha-1}h^{-\frac{1}{1-\alpha}} & for & h \leq e^{-\frac{1}{|1-2\alpha|}} & and \quad \alpha > \frac{1}{2} \end{array} \right\} \;\leq\; C\mathcal{T}_h. \tag{4.111}$$

Proof of Lemma 4.10.
It is convenient to think in terms of the local number density of triangles

$$n(x') := |T|^{-1} \quad \text{for} \quad x' \in T$$

since we have

$$\#\mathcal{T}_h = \int_{\Omega'} n(x')\,dx'. \tag{4.112}$$

Hence we need to estimate the number density n by below and above.

Let $C < \infty$ denote a generic constant which only depends on Λ and α_0. We use the notation $A \lesssim B$ if there exists such a C with $A \le CB$. We write $A \sim B$ if $A \lesssim B$ and $B \lesssim A$.

In this notation our assumptions (4.109) and (4.110) read

$$\operatorname{diam}(T) \;\sim\; h \operatorname{dist}(x'_T, \partial\Omega')^\alpha, \quad \operatorname{diam}(T)^2 \;\lesssim\; |T|, \tag{4.113}$$

respectively. Since $|T| \lesssim \operatorname{diam}(T)^2$ comes for free, we have for any $x' \in T$:

$$\begin{aligned} n(x') &= |T|^{-1} \\ &\sim \operatorname{diam}(T)^{-2} \\ &\sim h^{-2} \operatorname{dist}(x'_T, \partial\Omega')^{-2\alpha}. \end{aligned} \tag{4.114}$$

We now argue that

$$\operatorname{dist}(x'_T, \partial\Omega') \;\sim\; \max\left\{\operatorname{dist}(x', \partial\Omega'), h^{\frac{1}{1-\alpha}}\right\}. \tag{4.115}$$

To this purpose, we split (4.115) into the two statements

$$|\operatorname{dist}(x'_T, \partial\Omega') - \operatorname{dist}(x', \partial\Omega')| \;\le\; \tfrac{1}{2} \operatorname{dist}(x'_T, \partial\Omega') + Ch^{\frac{1}{1-\alpha}} \tag{4.116}$$

and

$$\operatorname{dist}(x'_T, \partial\Omega') \;\gtrsim\; h^{\frac{1}{1-\alpha}}. \tag{4.117}$$

Indeed, (4.116) implies

$$\operatorname{dist}(x'_T, \partial\Omega') \;\lesssim\; \max\left\{\operatorname{dist}(x', \partial\Omega'), h^{\frac{1}{1-\alpha}}\right\}, \tag{4.118}$$

whereas the combination of (4.116) and (4.117) yields

$$\operatorname{dist}(x', \partial\Omega') \overset{(4.116)}{\lesssim} \operatorname{dist}(x'_T, \partial\Omega') + Ch^{\frac{1}{1-\alpha}} \overset{(4.117)}{\lesssim} \operatorname{dist}(x'_T, \partial\Omega'). \tag{4.119}$$

Combining (4.119) once more with (4.117) we obtain the reverse of (4.118), i.e.

$$\operatorname{dist}(x'_T, \partial\Omega') \;\gtrsim\; \max\left\{\operatorname{dist}(x', \partial\Omega'), h^{\frac{1}{1-\alpha}}\right\}.$$

So indeed (4.115) follows from (4.116) and (4.117).

Let us now argue in favour of (4.116):

$$\begin{aligned} |\operatorname{dist}(x'_T, \partial\Omega') - \operatorname{dist}(x', \partial\Omega')| &\le \operatorname{diam}(T) \\ &\overset{(4.109)}{\le} \Lambda h \operatorname{dist}(x'_T, \partial\Omega')^\alpha \\ &= \Lambda (2\alpha)^\alpha h \left(\tfrac{1}{2\alpha} \operatorname{dist}(x'_T, \partial\Omega')\right)^\alpha. \end{aligned}$$

We now appeal to Young's inequality $ab \leq (1-\alpha)a^{\frac{1}{1-\alpha}} + \alpha b^{\frac{1}{\alpha}}$ and obtain

$$\begin{aligned} |\mathrm{dist}(x'_T, \partial\Omega') - \mathrm{dist}(x', \partial\Omega')| &\leq (1-\alpha)\left(\Lambda(2\alpha)^\alpha h\right)^{\frac{1}{1-\alpha}} + \tfrac{1}{2}\,\mathrm{dist}(x'_T, \partial\Omega') \\ &\leq Ch^{\frac{1}{1-\alpha}} + \tfrac{1}{2}\,\mathrm{dist}(x'_T, \partial\Omega'). \end{aligned}$$

We now establish (4.117). We notice that (4.113) implies that the angles of T are uniformly bounded away from zero so that

$$\begin{aligned} \mathrm{dist}(x'_T, \partial\Omega') &\geq \mathrm{dist}(x'_T, \partial T) \\ &\sim \mathrm{diam}(T) \\ &\overset{(4.109)}{\gtrsim} h\,\mathrm{dist}(x'_T, \partial\Omega')^\alpha. \end{aligned}$$

This yields (4.117).

The combination of (4.114) and (4.115) gives

$$\begin{aligned} n(x') &\sim h^{-2}\left(\max\left\{\mathrm{dist}(x', \partial\Omega'), h^{\frac{1}{1-\alpha}}\right\}\right)^{-2\alpha} \\ &= h^{-2}\min\left\{\mathrm{dist}(x', \partial\Omega')^{-2\alpha}, h^{-\frac{2\alpha}{1-\alpha}}\right\}. \end{aligned}$$

Hence according to (4.112)

$$\#\mathcal{T}_h \sim h^{-2}\int_{\Omega'} \min\left\{\mathrm{dist}(x', \partial\Omega')^{-2\alpha}, h^{-\frac{2\alpha}{1-\alpha}}\right\} dx'. \tag{4.120}$$

It remains to analyze the asymptotic behaviour of the integral in (4.120) for $h \downarrow 0$. By symmetry, it is enough to consider one eighth of Ω', namely $\Omega'_{\frac{1}{8}} := \{(x_1, x_2) \in \Omega' \,|\, x_2 < x_1 < \frac{1}{2}\}$. There, we have

$$\mathrm{dist}(x', \partial\Omega') = x_2 \quad \text{for} \quad x' \in \Omega'_{\frac{1}{8}}$$

so that for $h \leq \frac{1}{4}$ (and thus $h^{\frac{1}{1-\alpha}} \leq \frac{1}{4}$)

$$\begin{aligned} &\int_{\Omega'} \min\left\{\mathrm{dist}(x', \partial\Omega')^{-2\alpha}, h^{-\frac{2\alpha}{1-\alpha}}\right\} dx' \\ &\quad = 8\int_0^{\frac{1}{2}}\int_0^{x_1} \min\left\{x_2^{-2\alpha}, h^{-\frac{2\alpha}{1-\alpha}}\right\} dx_2 dx_1 \\ &\quad = 8\left\{\int_0^{h^{\frac{1}{1-\alpha}}} x_1 h^{-\frac{2\alpha}{1-\alpha}} dx_1 + \int_{h^{\frac{1}{1-\alpha}}}^{\frac{1}{2}} \left(h^{\frac{1}{1-\alpha}} h^{-\frac{2\alpha}{1-\alpha}} + \int_{h^{\frac{1}{1-\alpha}}}^{x_1} x_2^{-2\alpha} dx_2\right) dx_1\right\}. \end{aligned}$$

In the case of $\alpha \neq \frac{1}{2}$ we therefore have

$$\begin{aligned}
&\int_{\Omega'} \min\left\{\operatorname{dist}(x',\partial\Omega')^{-2\alpha}, h^{-\frac{2\alpha}{1-\alpha}}\right\} dx' \\
&\quad = 8\Bigg\{\tfrac{1}{2}\left(h^{\frac{1}{1-\alpha}}\right)^2 h^{-\frac{2\alpha}{1-\alpha}} + \left(\tfrac{1}{2} - h^{\frac{1}{1-\alpha}}\right) h^{\frac{1}{1-\alpha}} h^{-\frac{2\alpha}{1-\alpha}} \\
&\qquad\qquad + \tfrac{1}{1-2\alpha}\int_{h^{\frac{1}{1-\alpha}}}^{\frac{1}{2}} \left(x_1^{1-2\alpha} - \left(h^{\frac{1}{1-\alpha}}\right)^{1-2\alpha}\right) dx_1\Bigg\} \\
&\quad = 8\Bigg\{\tfrac{1}{2}h^2 + \tfrac{1}{2}h^{\frac{1-2\alpha}{1-\alpha}} - h^2 + \tfrac{1}{1-2\alpha}\tfrac{1}{2(1-\alpha)}\left(\left(\tfrac{1}{2}\right)^{2(1-\alpha)} - \left(h^{\frac{1}{1-\alpha}}\right)^{2(1-\alpha)}\right) \\
&\qquad\qquad - \tfrac{1}{1-2\alpha}\left(\tfrac{1}{2} - h^{\frac{1}{1-\alpha}}\right)\left(h^{\frac{1}{1-\alpha}}\right)^{1-2\alpha}\Bigg\} \\
&\quad = 8\left\{\tfrac{\alpha}{2(1-\alpha)}h^2 + \tfrac{1}{1-2\alpha}\left(\tfrac{1}{1-\alpha}\left(\tfrac{1}{2}\right)^{3-2\alpha} - \alpha h^{\frac{1-2\alpha}{1-\alpha}}\right)\right\}. \qquad (4.121)
\end{aligned}$$

To have a closer look at $\frac{1}{1-2\alpha}\left(\frac{1}{1-\alpha}\left(\frac{1}{2}\right)^{3-2\alpha} - \alpha h^{\frac{1-2\alpha}{1-\alpha}}\right)$ for $\alpha \approx \frac{1}{2}$, we introduce

$$\beta := 1 - 2\alpha \ \in\ (-1,1] \quad \text{and} \quad g := h^{\frac{1}{1-\alpha}} \ \in\ (0,\tfrac{1}{4}),$$

so that for $\beta \ll 1$

$$\begin{aligned}
&\tfrac{1}{1-2\alpha}\left(\tfrac{1}{1-\alpha}\left(\tfrac{1}{2}\right)^{3-2\alpha} - \alpha h^{\frac{1-2\alpha}{1-\alpha}}\right) \\
&\quad = \tfrac{1}{2\beta}\left(\tfrac{1}{(1+\beta)2^\beta} - (1-\beta)g^\beta\right) \\
&\quad \sim \tfrac{1}{\beta}(1-g^\beta) \\
&\quad = (\log\tfrac{1}{g})\tfrac{1}{\beta\log\frac{1}{g}}\left(1 - e^{-\beta\log\frac{1}{g}}\right) \\
&\quad \sim (\log\tfrac{1}{g})\begin{cases} \frac{1}{\beta\log\frac{1}{g}} & \text{for} \quad \beta\log\frac{1}{g} \gtrsim 1 \\ 1 & \text{for} \quad |\beta\log\frac{1}{g}| \lesssim 1 \\ -\frac{1}{\beta\log\frac{1}{g}}e^{-\beta\log\frac{1}{g}} & \text{for} \quad -\beta\log\frac{1}{g} \gtrsim 1 \end{cases} \\
&\quad = \left\{\begin{array}{cccc} \frac{1}{|\beta|} & \text{for} & \log\frac{1}{g} \gtrsim \frac{1}{|\beta|} & \text{and} \quad \beta > 0 \\ \log\frac{1}{g} & \text{for} & \log\frac{1}{g} \lesssim \frac{1}{|\beta|} & \\ \frac{1}{|\beta|}g^{-|\beta|} & \text{for} & \log\frac{1}{g} \gtrsim \frac{1}{|\beta|} & \text{and} \quad \beta < 0 \end{array}\right\}. \qquad (4.122)
\end{aligned}$$

Formula (4.121) and estimate (4.122) translate into

$$\begin{aligned}
&\int_{\Omega'} \min\left\{\operatorname{dist}(x',\partial\Omega')^{-2\alpha}, h^{-\frac{2\alpha}{1-\alpha}}\right\} dx' \\
&\quad \sim \left\{\begin{array}{cccc} \frac{1}{1-2\alpha} & for & h \le e^{-\frac{1}{|1-2\alpha|}} & and \quad \alpha < \frac{1}{2} \\ (\log\frac{1}{h^2}) & for & h \ge e^{-\frac{1}{|1-2\alpha|}} & or \quad \alpha = \frac{1}{2} \\ \frac{1}{2\alpha-1}h^{-\frac{2\alpha-1}{1-\alpha}} & for & h \le e^{-\frac{1}{|1-2\alpha|}} & and \quad \alpha > \frac{1}{2} \end{array}\right\}.
\end{aligned}$$

In view of (4.120), this yields the proposition for $\alpha \neq \frac{1}{2}$. The case $\alpha = \frac{1}{2}$ follows by continuity. □

Table 4.5 and Table 4.6 show that the theoretical asymptotic result captures the actual experimental behavior. The parameters h and α listed in the tables are the ones specifying the refinement rule (4.107). The number $\#\mathcal{T}_h$ of triangles is denoted by N. The last column in each table documents the experimental value of the scaling predicted in Lemma 4.10. All the triangulations involved in the numerical experiments are generated by the algorithm presented at the beginning of this section.

h	N	Nh^3
5.0e–1	2768	3.5e+2
4.0e–1	5824	3.7e+2
3.0e–1	15224	4.1e+2
2.0e–1	50464	4.0e+2
1.0e–1	416456	4.2e+2

Table 4.5: Experimental complexity for $\alpha = 2/3$ and h as listed: N denotes the number $\#\mathcal{T}_h$ of triangles in Lemma 4.10 and the last column documents the approximate proportionality factor predicted there.

h	N	$Nh^2 \log^{-1}(h^{-2})$
2.0e–1	3136	3.9e+1
1.0e–1	15440	3.4e+1
5.0e–2	72216	3.0e+1
2.5e–2	328576	2.8e+1

Table 4.6: Experimental complexity for $\alpha = 1/2$. Notations are as in Table 4.5 above.

In view of Theorem 4.2, which states that the discretization error ϵ is estimated as

$$\epsilon \lesssim \left\{ \begin{array}{ccc} h^{\frac{3}{2}} & \text{for} & \alpha \geq \frac{2}{3} \\ h^{\frac{1}{2(1-\alpha)}} & \text{for} & \alpha \leq \frac{2}{3} \end{array} \right\}, \tag{4.123}$$

(we neglect logarithmic terms) and of (4.111) we now ask the following question: For which degree of refinement is the $\epsilon - N$ relation most favorable? A glance at (4.111) and (4.123) reveals

$$\epsilon \lesssim \left\{ \begin{array}{ccc} N^{-\frac{3(1-\alpha)}{2}} & \text{for} & \frac{2}{3} \leq \alpha \\ N^{-\frac{1}{2}} & \text{for} & \frac{1}{2} \leq \alpha \leq \frac{2}{3} \\ N^{-\frac{1}{4(1-\alpha)}} & \text{for} & \alpha \leq \frac{1}{2} \end{array} \right\}.$$

Hence the α in the range $\left[\frac{1}{2}, \frac{2}{3}\right]$ lead to the best $\epsilon - N$ relation. In the sequel, we shall focus on $\alpha = \frac{2}{3}$.

Remark 4.3. *The $\epsilon - N$ relation predicted here is less optimal than the one proven in [22] for anisotropically graded meshes: there the optimal scaling gives the relation $\epsilon \lesssim N^{-3/4}$. For our type of triangulations $\mathcal{T}_h$ justified in Section 4.2 with emphasis on the bound (4.14), we can expect only $\epsilon \lesssim N^{-1/2}$ (with the choice $\alpha = \frac{2}{3}$). Still, this improves the scaling $\epsilon \lesssim N^{-1/4}$ related to Cartesian meshes, which becomes also evident in the numerical experiments presented in Section 4.9.*

4.6 A Fully Populated Stiffness Matrix

With this section, we start the discussion of algorithms to solve the Galerkin ansatz (4.77). Let $\chi_1, \chi_2, .., \chi_N$ be the characteristic functions associated to the triangles $T_1, T_2, .., T_N \in \mathcal{T}_h$ (with $N = \#\mathcal{T}_h$). The ansatz

$$\sigma_h \;=\; \sum_{i=1}^{N} z_i \chi_i$$

for the solution of (4.77) leads to the linear system of algebraic equations

$$\sum_{i=1}^{N} z_i \int_{T_i} \int_{T_j} \frac{1}{4\pi|x' - y'|}\, dy'\, dx' + \int_{T_j} H'_{ext} \cdot x'\, dx' \;=\; 0\ .$$

These can be written in matrix–vector form as

$$Kz + b \;=\; 0, \tag{4.124}$$

where K is a positive definite and symmetric matrix with entries

$$K_{ij} \;:=\; \int_{T_i} \int_{T_j} \frac{1}{4\pi|x' - y'|}\, dy'\, dx'\ , \tag{4.125}$$

$z = (z_j)_{j=1,..,N}$ is the vector of the unknowns and b is defined by

$$b_j := \int_{T_j} H'_{ext} \cdot x'\, dx'\ .$$

K_{ij} represents the interaction energy of unit charges placed in T_i and T_j. We calculate the entries K_{ij} by the numerical quadrature scheme introduced in Section 4.1. Due to the non–locality of the magnetostatic interaction, the matrix K is fully populated.

Using direct methods such as Gaussian elimination or Cholesky factorization to solve (4.124) is prohibitive for large problems. Iterative solvers in general need $\mathcal{O}(N^2)$ operations per iteration, so computational cost still becomes excessive for large N. Indeed, any algorithm based on an *explicit* representation of K has at least $\mathcal{O}(N^2)$–complexity in time and memory.

To solve (4.124) in sub–quadratic time, we combine the conjugate gradient method with two different methods of matrix compression:

- For a uniform triangulation $\mathcal{Q}_h$ as in Section 3.4, the interaction matrix K bears a Toeplitz–type structure, i. e. the matrix entries depend only on the distance vector between the corresponding cells. This discrete convolution structure of course reflects the continuous convolution structure (2.6). A matrix–vector product in form of a discrete convolution can be efficiently computed by FFT with complexity $\mathcal{O}(N \log N)$. By simply filling up the data by zeros up to the next dyadic size, no periodicity is required [3, 46].

- For a–priori locally refined triangulations $\mathcal{T}_h$ (see Figure 4.9) we implemented a more flexible, yet (near) optimal–complexity algorithm to carry out the convolution, based on the concept of $\mathcal{H}$–matrices (hierarchical matrices) [28]. $\mathcal{H}$–matrices are natural approximations of fully populated stiffness matrices as they appear in the finite element–based Galerkin discretization of non–local integral operators: Depending on the smoothness properties of the kernel, submatrices of the stiffness matrix are replaced by suitable low rank approximations. We implemented a new class of hierarchical matrices, the so–called $\mathcal{H}^2$–matrices [29], see Section 4.8.

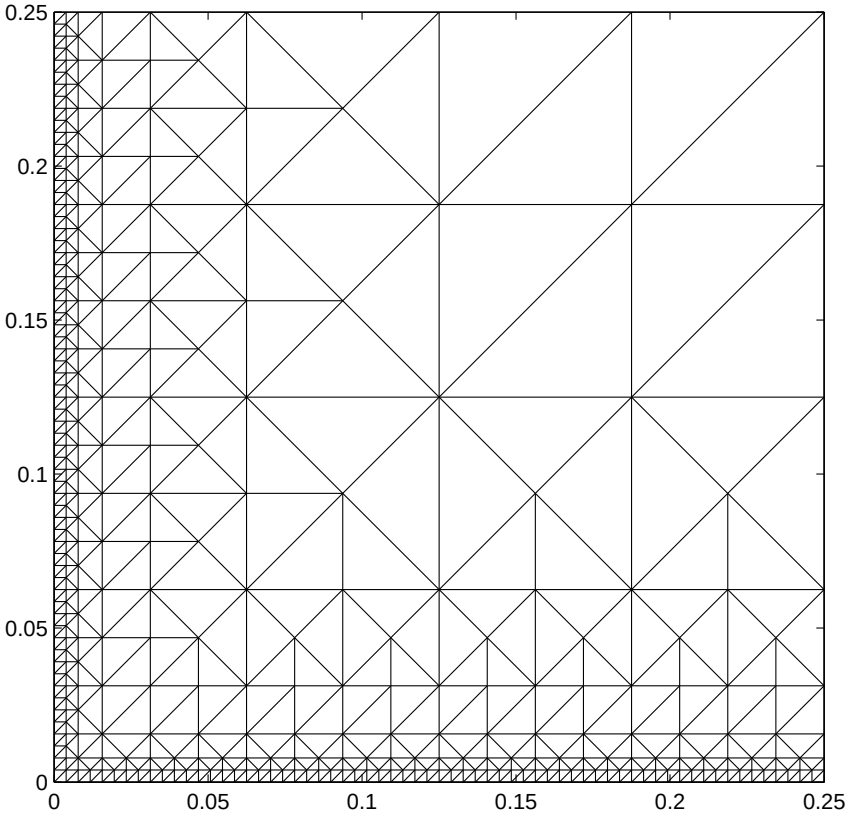

Figure 4.9: Section of a triangulation $\mathcal{T}_h$ with $\alpha = 2/3$ near the corner of $\Omega' = (0,1)^2$

4.7 FFT–Based Algorithm

We consider a triangulation $\mathcal{Q}_h$ which comes from a Cartesian grid and is divided into lower and upper triangles, see Section 3.4. For a suitable choice of indices the matrix K and the vector z have a special block structure

$$K = \begin{pmatrix} K^{(l,l)} & K^{(l,u)} \\ K^{(u,l)} & K^{(u,u)} \end{pmatrix}, \quad z = \begin{pmatrix} z^{(l)} \\ z^{(u)} \end{pmatrix}, \tag{4.126}$$

where $z^{(l)}$ represents the data on lower triangles and $z^{(u)}$ those on upper triangles. $K^{(l,l)}$ is the interaction matrix for lower triangles, $K^{(l,u)}$ is the interaction matrix for one fixed lower triangle with all the upper ones, and so on.

Since the given triangulation is translation invariant, each of the K–blocks bears a Toeplitz–type structure, i. e. the matrix elements depend only on the distance vector between the corresponding cells, thus instead of storing $N^2/4$ matrix elements we only have to store a vector of length $N/2$. The mathematical form of the matrix–vector multiplication $K^{(l,l)}z^{(l)}$ is that of a discrete convolution, reflecting the continuous convolution structure (2.6).

Direct computation of the discrete convolution of two n–long sequences requires $\mathcal{O}(n^2)$ operations. Computational cost is reduced by taking advantage of the discrete convolution theorem: the discrete Fourier transform (DFT) of the convolution of two discrete periodic functions equals the componentwise product of the DFTs of the two functions. By performing the DFT with the help of Fast Fourier Transform (FFT) algorithms, the over–all complexity of the discrete convolution is reduced to $\mathcal{O}(n \log n)$. We use the implementation of the FFT documented in [24].

Due to the non–periodicity of our data we have to extend the vector z by zeros. This technique of *zero–padding* avoids any end effects as described in [46, Chapter 12], but increases the size of the input data for the FFT in 2–d by a factor of four.

Once the DFTs of the K–blocks are given, the matrix–vector product Kz is computed by applying a 2–d FFT routine four times (two forward and two backward transforms). Since the input data is purely real we can take advantage of a special real–to–complex variant of the FFT improving speed and memory usage roughly by a factor of two.

Neither our special data structure (4.126), nor the zero padding technique affect the $\mathcal{O}(n \log n)$–behavior of the FFT: if n is a power of 2, the classical Cooley–Tukey FFT algorithm for n complex data requires asymptotically $\frac{n}{2} \log_2 n$ complex multiplications, whereas the real–to–complex FFT of n real data results in asymptotically $n \log_2 n$ real multiplications. So if $N = 2^\nu$ is the total number of triangles (i. e. we have $N/2$ lower and $N/2$ upper triangles), for each of the four FFTs the data–size is $n = 4 \cdot \frac{N}{2}$ (the factor 4 is due to zero–padding), which results in a total number of approximately $8N \log_2 N$ real multiplications in the computation of Kz. The number of multiplications in frequency space is of order N and thus asymptotically negligible.

In practice, so–called split–radix FFTs that rely on a combination of elementary 2–point and 4–point transforms are more efficient than pure radix–2 algorithms like the Cooley–Tukey.

4.8 $\mathcal{H}$–Matrices

The notion of $\mathcal{H}$–matrices (hierarchical matrices) was introduced in [28]. These matrices are *data–sparse*: they can be described by relatively few data. $\mathcal{H}$–matrices are natural approximations of fully populated stiffness matrices as they appear in finite element–based Galerkin discretization of non–local integral operators [32]. The use of $\mathcal{H}$–matrices reduces storage requirements and the complexity of matrix–vector multiplication to almost linear complexity $\mathcal{O}(N \log N)$.

The reliability of $\mathcal{H}$–matrices for the approximation of integral operators is based on the smoothness properties of the kernel. Typically, one should think of the kernel as a singular convolution kernel as in (2.6). Hence the kernel becomes singular only at the diagonal of the stiffness matrix K. Away from the diagonal one replaces submatrices of K by suitable low rank approximations. This is motivated by the fact that off–diagonal submatrices are numerically of low rank, i.e. the columns are nearly linearly dependent. The approximate matrix is then stored in a hierarchical data structure of size $\mathcal{O}(N \log N)$, thus allowing an evaluation of matrix–vector products in $\mathcal{O}(N \log N)$ time. This is a common strategy, particularly in boundary element methods and the n-body problem, leading to algorithms like the panel clustering technique [33] and the fast multipole method [26]. The basic idea can be summarized by the following recipe: The near–field component of the long range interaction is evaluated by direct computation whereas the far–field component is approximated using a hierarchical clustering of distant elements.

The complexity of the matrix–vector multiplication is further reduced to optimal complexity $\mathcal{O}(N)$ by a new class of hierarchical matrices, the so–called $\mathcal{H}^2$–matrices, introduced in [31]. Let us focus on interpolation–based low rank approximations: Polynomial interpolation in one argument of the kernel $k(.,.)$ leads to $\mathcal{H}$–matrix approximation, interpolation in both arguments leads to so–called *uniform* $\mathcal{H}$–matrices. The polynomial interpolation allows for a hierarchical change from the finite element basis to the cluster basis and vice versa; this is the $\mathcal{H}^2$–matrix approximation with optimal complexity in the matrix–vector multiplication. For a comparison of the different types of hierarchical matrices, see [30].

$\mathcal{H}^2$–matrices have already been applied in computational electromagnetism to deal with non–sparse matrices arising from Galerkin boundary element discretizations [5]. The first application of $\mathcal{H}^2$–matrices to 3–d and 2–d stray field computation in micromagnetics is given in [11]: in the 2–d case the $\mathcal{H}^2$–matrix method is applied on the 2–d Newtonian kernel $-\log|x|$, and effective numerical simulations are carried out. Further details on the $\mathcal{H}^2$–matrix approach in this context are presented in [45].

The $\mathcal{H}^2$–matrix method consists of a *setup phase*, i.e. the computation of the compressed matrix representation (which has to be done only once for a given triangulation), and an algorithm for fast matrix–vector multiplication.

We suppress all primes for the two–dimensional variables in this section.

4.8.1 Setup Phase

The setup phase starts with a rearrangement of the data structure. Let I denote the index set of the finite element basis. In our case, I just enumerates the triangles and has cardinality N.

- I is decomposed along a binary tree introducing clusters $\tau \subset I$, see Figure 4.10. The subset $T_\tau \subset \Omega$ is the union of the supports of the basis functions

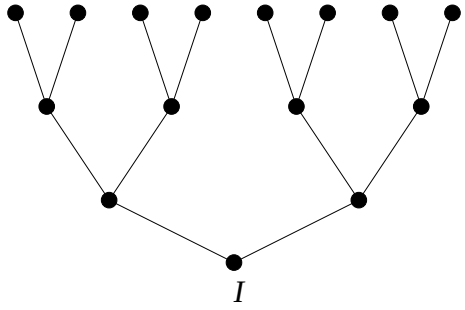

Figure 4.10: Cluster tree for I

χ_i, $i \in \tau$. In our case T_τ is just the union of the triangles T_i, $i \in \tau$, see Figure 4.11. The bounding box $B_\tau \subset \mathbb{R}^2$ is the smallest rectangle with axes in x_1 and

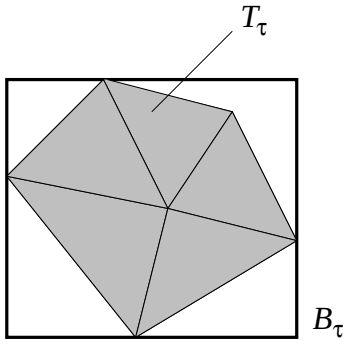

Figure 4.11: Bounding box B_τ for T_τ

x_2 direction which contains T_τ, see Figure 4.11. In order to generate the tree, we use a geometry–based algorithm:

– I is the root of the binary tree.

– For each cluster τ, we split the corresponding boundary box B_τ by bisection of its longer side. This defines the two son clusters.

– We stop when a cluster contains $\leq p^2$ triangles. This introduces a parameter p which we choose to be $p = 3$.

Notice that by construction on each level of the binary tree the bounding boxes are not too anisotropic in the sense of $\text{area}(B_\tau) \sim \text{diam}(B_\tau)^2$.

- A pair of clusters $\tau_1 \times \tau_2$ is called an *admissible block* if a geometric condition is satisfied that bounds the diameter of the clusters by their distance, i.e.

$$\max\{\text{diam}(B_{\tau_1}), \text{diam}(B_{\tau_2})\} \leq 2\eta \ \text{dist}(B_{\tau_1}, B_{\tau_2}) \ .$$

This introduces a parameter η. It has turned out in our experiments that a good value for the parameter η to choose here is $\eta = 0.5$. This defines a block (= pair of clusters) tree, which is a decomposition of $I \times I$, by the following algorithm:

– $I \times I$ is the root of the block tree.

– Recursively, each block $\tau_1 \times \tau_2$ is decomposed into the four sub–blocks (formed by the pairs of son clusters of τ_1, τ_2) until one of the following two termination criteria holds:

1. $\tau_1 \times \tau_2$ is admissible,
2. τ_1 or τ_2 is a leaf.

The leaves of this block tree induce a partitioning of $I \times I$, see Figure 4.12.

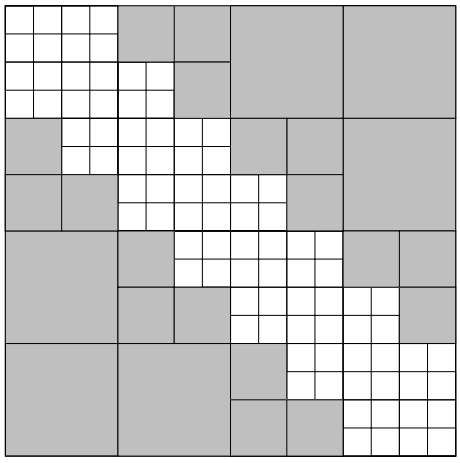

Figure 4.12: Block partitioning of $I \times I$

4.8.2 Low Rank Approximation of the Kernel

The block partitioning of $I \times I$ induces a block partitioning of the matrix K. The idea is to approximate the restriction of K on each admissible block $\tau_1 \times \tau_2$ (the shaded ones in Figure 4.12) by a matrix of fixed rank p^2. This is done by (tensor product) Chebyshev interpolation of the kernel $k(x, y)$, $(x, y) \in \Omega \times \Omega$, with polynomials of degree $(p-1)$ in both arguments. More precisely, for every cluster τ, let $(x_\iota^\tau)_\iota$ denote the p^2 interpolation points in the bounding box B_τ. They are given by the zeros of the Chebyshev polynomials. Let p_ι^τ be the corresponding Lagrange polynomials. For an admissible cluster $\tau_1 \times \tau_2$, the kernel function $k(x, y)$ is replaced by

$$\tilde{k}(x, y) = \sum_{\iota,\kappa=1}^{p^2} k(x_\iota^{\tau_1}, y_\kappa^{\tau_2}) p_\iota^{\tau_1}(x) p_\kappa^{\tau_2}(y) \tag{4.127}$$

for $(x, y) \in B_{\tau_1} \times B_{\tau_2}$. On the blocks which are not admissible (the non–shaded area in Figure 4.12), K remains unchanged. Notice that this in particular holds for the entries near the singular diagonal. Hence the approximation distinguishes between the far–field and near–field components of the long range interaction described by the kernel function k.

4.8.3 Matrix–Vector Multiplication

Consider the operator $\tilde{K}$ defined by the kernel $\tilde{k}$ in (4.127). Its matrix representation $(\tilde{K}_{ij})_{(i,j)\in I\times I}$ w. r. t. the canonical finite element basis is given by

$$\tilde{K}_{ij} = \sum_{\iota,\kappa} \int_{T_i} p_\iota^{\tau_1}(x)dx \; k(x_\iota^{\tau_1}, y_\kappa^{\tau_2}) \int_{T_j} p_\kappa^{\tau_2}(y)dy \; , \tag{4.128}$$

where $\tau_1 \times \tau_2$ is the unique block in the partitioning of $I \times I$ which contains (i, j). Remember that K_{ij} is only replaced by $\tilde{K}_{ij}$ if $\tau_1 \times \tau_2$ is an admissible block. We write this as

$$\tilde{K}_{ij} = \sum_{\iota,\kappa} V_{i\iota}^{\tau_1} S_{\iota\kappa}^{\tau_1\times\tau_2} V_{j\kappa}^{\tau_2} = \left[V^{\tau_1} S^{\tau_1\times\tau_2} (V^{\tau_2})^T\right]_{ij}, \tag{4.129}$$

where

$$S_{\iota\kappa}^{\tau_1\times\tau_2} := k(x_\iota^{\tau_1}, y_\kappa^{\tau_2}), \quad V_{i\iota}^{\tau_1} := \int_{T_i} p_\iota^{\tau_1}(x)dx$$

with the implicit understanding that $i \in \tau_1$. Notice that the action of V^{τ_1} can be interpreted as a transformation from the finite element basis (as enumerated by $i \in I$) to the cluster basis (as parametrized by all the clusters of the binary tree). We observe that each cluster corresponds to p^2 data. Hence the matrix–vector multiplication can be interpreted as a *forward transformation* V^T, a matrix–vector multiplication with S, and a *backward transformation* V.

The additional idea of $\mathcal{H}^2$–matrices is to organize the transformation V in a hierarchical way. It is based on the insight that the Lagrange polynomials $(p_\iota^\tau(x))_\iota$ for a

cluster τ can be expressed as a linear combination of $(p_\kappa^{\tau_1}(x))_\kappa$ for any other cluster τ_1, in particular one of the two son clusters of τ:

$$p_\iota^\tau(x) = \sum_\kappa p_\kappa^{\tau_1}(x) p_\iota^\tau(x_\kappa^{\tau_1}) \ .$$

This implies the hierarchical relationship

$$V_{i\iota}^\tau = \sum_\kappa V_{i\kappa}^{\tau_1} B_{\kappa\iota}^{\tau_1,\tau} = [V^{\tau_1} B^{\tau_1,\tau}]_{i\iota} \ , \tag{4.130}$$

provided $i \in \tau_1 \subset \tau$ where

$$B_{\kappa\iota}^{\tau_1,\tau} := p_\iota^\tau(x_\kappa^{\tau_1}) \ .$$

Hence the forward transformation requires an initial transformation from the finite element basis to the leaves of the cluster tree. Then one uses (4.130) to get recursively down the binary tree to the root.

4.8.4 Complexity of the Matrix–Vector Multiplication

Within the above geometry–based algorithm, the cluster tree (see Figure 4.10) is nearly balanced, which means

- it has approximately N/p^2 leaves and
- it has approximately N/p^2 internal nodes.

In our case, the generated block tree is well–behaved in the following sense:

- The number of blocks in the partitioning of $I \times I$ (see Figure 4.12) is approximately proportional to the number of leaves N/p^2, see Table 4.7 for a uniform triangulation and Tables 4.8 and 4.9 for a locally refined triangulation as described in Section 4.5. This property can be theoretically derived for any triangulation which is regular in the sense of 4.108, see [25, Lemma 4.5]. The prefactor depends on the type of the triangulation and, of course, on the parameter η.

From these data we conclude

- Each involved V– and B–matrix has $p^2 \cdot p^2 = p^4$ entries. The V–matrices are applied on the $\approx N/p^2$ leaves. Each time one moves from two son clusters to their father cluster, two B–matrices are involved. There are $\approx N/p^2$ internal nodes. Hence the forward transformation requires $\approx (p^4+2p^4)\cdot(N/p^2) = 3Np^2$ multiplications.
- The backward transformation likewise requires $\approx 3Np^2$ multiplications.
- Each S–matrix has p^4 entries. There is an S–matrix for each of the $\mathcal{O}(N/p^2)$ blocks in the partitioning of $I \times I$. Hence the matrix multiplication with S takes $\mathcal{O}(Np^2)$ multiplications.

N	#blocks	#blocks/(Np^2)
8192	24808	3.4e–1
32768	104530	3.5e–1
131072	430378	3.7e–1
524288	1744468	3.7e–1

Table 4.7: $\mathcal{H}^2$–matrix compression for uniform triangulations $\mathcal{Q}_h$. Here N is the number of triangles and the polynomial degree is $p = 3$. The last column reflects the expected complexity of the block tree.

h	N	#blocks	#blocks/(Np^2)
5.0e–1	2768	18684	7.5e–1
4.0e–1	5824	38038	7.3e–1
3.0e–1	15224	86482	6.3e–1
2.0e–1	50464	383446	8.4e–1
1.0e–1	416456	3215884	8.6e–1

Table 4.8: $\mathcal{H}^2$–matrix compression for locally refined triangulations $\mathcal{T}_h$ with $\alpha = 2/3$. These are the triangulations documented in Table 4.5. The last column reflects the expected complexity of the block tree.

h	N	#blocks	#blocks/(Np^2)
2.0e–1	3136	14260	5.1e–1
1.0e–1	15440	71956	5.2e–1
5.0e–2	72216	266554	4.1e–1
2.5e–2	328576	1149866	3.9e–1

Table 4.9: $\mathcal{H}^2$–matrix compression for locally refined triangulations $\mathcal{T}_h$ with $\alpha = 1/2$. These are the triangulations documented in Table 4.6. The last column reflects the expected complexity of the block tree.

4.8.5 Setup Time and Compression Rate

We notice that replacing the fully populated matrix K in (4.124) by the $\mathcal{H}^2$–matrix $\tilde{K}$ introduces an additional approximation error. A thorough error analysis in terms of the parameters η and p is presented in [29]. Here we test the quality of the $\mathcal{H}^2$–matrix compression numerically: we compute the self–energy of the unit square $\Omega = (0,1)^2$ on several $\mathcal{T}_h$–type triangulations and compare the numerical results with the exact value $I(\Omega)$ provided by Lemma 4.2. We consider the locally refined triangulations $\mathcal{T}_h$ with $\alpha = 2/3$ from Table 4.8, which are also used in the succeeding Section 4.9. Our numerical experiments show that the relative error in the computation of the self–energy does not exceed 1%.

The relative error in Table 4.10 is defined as

$$\sqrt{\left|\frac{I(\Omega) - z^T \tilde{K} z}{I(\Omega)}\right|} \tag{4.131}$$

with $z = (1, 1, .., 1)^T \in \mathbb{R}^N$. This expression for the relative error in stray field computations is justified in detail in the following section, see (4.132).

To conclude this section, we present in Table 4.11 the numerically observed setup time and compression rate of the $\mathcal{H}^2$–matrix $\tilde{K}$.

N	CPU (s)	relative error
2.8e+3	3.1e–2	9.7e–3
5.8e+3	7.5e–2	9.8e–3
1.5e+4	3.1e–1	1.0e–2
5.0e+4	7.0e–1	1.0e–2

Table 4.10: Computing the self–energy of the unit square via the $\mathcal{H}^2$–matrix method: N denotes the number of triangles (in scientific notation) of the triangulations discussed in Table 4.8. In the second column we document the CPU time (in seconds), the last column shows the relative error (4.131). All numerical experiments were done on a Pentium III processor running at 700 MHz.

N	setup (s)	compression
2.8e+3	5.5e+0	4.4e–2
5.8e+3	1.2e+1	2.2e–2
1.5e+4	5.6e+1	1.2e–2
5.0e+4	1.1e+2	1.7e–2

Table 4.11: In the second column we document the CPU time (in seconds) for the setup of the $\mathcal{H}^2$–matrix. The last column shows the compression rate, i. e. the ratio between the computer storage needed for the $\mathcal{H}^2$–matrix and the original fully populated matrix.

4.9 Numerical Results

We suppress all primes for the two–dimensional variables in this section.

We compare the performance of the FFT–based algorithm and the $\mathcal{H}^2$–matrix method for the square $\Omega = (0, 1)^2$ and external fields $H_{ext} = (0.2, 0.2)$ and $H_{ext} = (0.3, 0.1)$. Since we do not know the exact solution σ^* of (4.124), we derive a reliable approximation $E(\sigma^*)$ to the exact energy of σ^* as follows: we compute the charge

density σ_h by the FFT–based conjugate gradient method with relative residuum 10^{-12} for several values of h. Linear extrapolation to $h = 0$ then yields $E(\sigma^*)$, since $E(\sigma_h)$ depends almost linearly on h (see Theorem 4.2 with $\alpha = 0$). This process is illustrated by Figure 4.13 for the external field $H_{ext} = (0.2, 0.2)$.

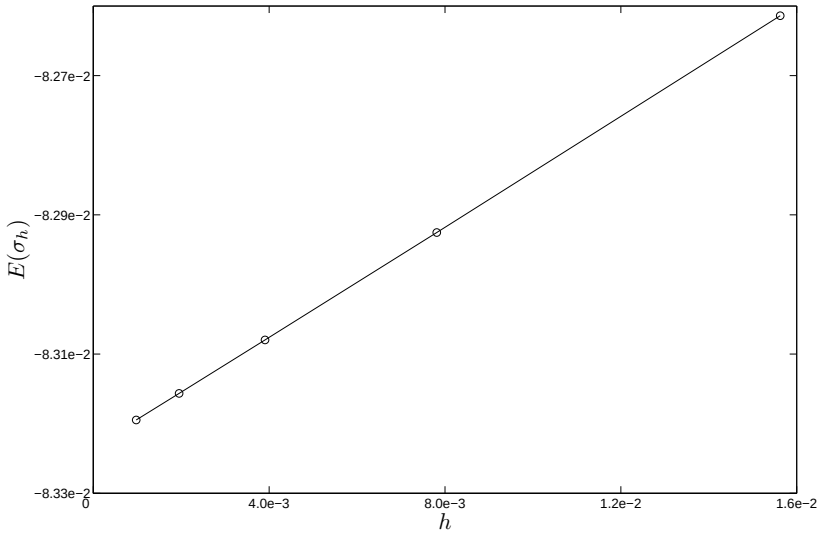

Figure 4.13: Tight approximation of $E(\sigma^*)$ by the extrapolation of $E(\sigma_h)$ on uniform triangulations $\mathcal{Q}_h$. We choose $h = 2^{-k}$ with $6 \leq k \leq 10$.

Then we start the FFT–based and the $\mathcal{H}^2$–based conjugate gradient method on triangulations $\mathcal{Q}_h$ and $\mathcal{T}_h$ respectively, and terminate the iteration when a prescribed error ϵ relative to σ^* is attained. Here ϵ denotes the relative error between the approximate solution σ_h and σ^* in the homogeneous part of the continuous $H^{-1/2}(\mathbb{R}^2)$–norm:

$$\epsilon := \frac{\left(\int_{\mathbb{R}^2} |(\nabla)^{-1/2}(\sigma^* - \sigma_h)|^2 dx\right)^{1/2}}{\left(\int_{\mathbb{R}^2} |(\nabla)^{-1/2}\sigma^*|^2 dx\right)^{1/2}} \ .$$

We can express ϵ in terms of the energies since E is the sum of a quadratic form and a linear functional

$$E(\sigma_h) \ = \ B(\sigma_h, \sigma_h) + L(\sigma_h),$$

where $B(\sigma_h, \sigma_h)$ is one half of the squared homogeneous part of the $H^{-1/2}(\mathbb{R}^2)$–norm of σ_h. Therefore we have

$$\begin{aligned} E(\sigma_h) - E(\sigma^*) &= B(\sigma_h + \sigma^*, \sigma_h - \sigma^*) + L(\sigma_h - \sigma^*) \\ &= B(\sigma_h - \sigma^*, \sigma_h - \sigma^*) + 2B(\sigma^*, \sigma_h - \sigma^*) + L(\sigma_h - \sigma^*) \\ &= B(\sigma_h - \sigma^*, \sigma_h - \sigma^*), \end{aligned}$$

since $2B(\sigma^*, \sigma_h - \sigma^*) + L(\sigma_h - \sigma^*) = 0$ is just the weak formulation of the Euler–Lagrange equation tested with $(\sigma_h - \sigma^*)$. So the relative error ϵ can be rewritten as

$$\epsilon \;=\; \sqrt{\frac{E(\sigma_h) - E(\sigma^*)}{E(\sigma^*)}}\;. \tag{4.132}$$

In particular, the notion of error is independent of the chosen grid. We notice that the conjugate gradient algorithm monotonically decreases the energy norm distance (4.132) to the solution σ^*, i. e. we have $E(\sigma^*) \leq E(\sigma_h^{(k+1)}) \leq E(\sigma_h^{(k)})$ for each iteration step k, see [46, Chapter 10.6]. We further stress that a stopping criterion based on the energy norm was already recommended in the classical introductory paper [34].

Table 4.12 and Table 4.13 show the CPU times in seconds for the prescribed relative error ϵ in the case $H_{ext} = (0.2, 0.2)$. Here N is the number of degrees of freedom, given in Table 4.12 for a triangulation $\mathcal{Q}_h$ and in Table 4.13 for a triangulation $\mathcal{T}_h$ (with the refinement rate $\alpha = 2/3$ a–priori predicted by the numerical analysis, see the discussion in Section 4.4). Cells of the table without entry indicate that the prescribed relative error is not attainable on the given triangulation. Since we want to test the performance of FFT–based versus $\mathcal{H}^2$–based matrix–vector products in the conjugate gradient iterations, we do not consider the CPU times for the setup phases and the computation of ϵ. In the case of triangulations $\mathcal{T}_h$ the conjugate gradient method is preconditioned by the diagonal matrix $D = \mathrm{diag}(K_{11}, ..., K_{NN})$. This simple preconditioning has absolutely no effect on the performance of the conjugate gradient method in case of triangulations $\mathcal{Q}_h$. Our numerical experiments show that both methods are comparable with respect to computation time at a relative error of the order of 10%, and reveal advantages in favor of the $\mathcal{H}^2$–matrix method at a relative error of the order of 5%.

In Tables 4.14 and 4.15 we document the number of iterations in the conjugate gradient method necessary to attain the prescribed relative error ϵ. Tables 4.16 up to 4.19 show the corresponding results for $H_{ext} = (0.3, 0.1)$.

In Figures 4.14 and 4.15 we display the minimal observed CPU times for given ϵ in our numerical experiments.

N \ ϵ	1.0e–1	7.0e–2	5.0e–2	3.0e–2
4608	1.4e–1	—	—	—
8192	8.7e–2	—	—	—
18432	1.9e–1	7.4e–1	—	—
32768	4.1e–1	7.0e–1	—	—
73728	8.9e–1	1.4e+0	3.3e+0	—
131072	1.9e+0	2.6e+0	4.2e+0	—
294912	4.4e+0	6.0e+0	9.6e+0	—
524288	8.2e+0	1.1e+1	1.5e+1	—
1179648	1.7e+1	2.4e+1	3.2e+1	7.8e+1
2097152	3.6e+1	4.9e+1	6.5e+1	1.1e+2

Table 4.12: CPU times in seconds for the FFT–based algorithm: N is the number of triangles of the uniform triangulation $\mathcal{Q}_h$, whereas ϵ denotes the prescribed relative error (4.132). The conjugate gradient method is used as iterative solver for (4.124), and the iteration is terminated when the prescribed relative error ϵ is attained. The external field is $H_{ext} = (0.2, 0.2)$.

N \ ϵ	1.0e–1	7.0e–2	5.0e–2	3.0e–2
2768	7.6e–2	1.8e–1	—	—
5824	1.8e–1	2.4e–1	8.6e–1	—
15224	7.2e–1	7.2e–1	1.3e+0	—
50464	1.7e+0	1.7e+0	2.8e+0	5.1e+0

Table 4.13: CPU times in seconds for the conjugate gradient method with $\mathcal{H}^2$–matrix compression. Notations as in Table 4.12

N \ ϵ	1.0e–1	7.0e–2	5.0e–2	3.0e–2
4608	18	—	—	—
8192	6	—	—	—
18432	6	19	—	—
32768	5	9	—	—
73728	5	8	18	—
131072	5	7	12	—
294912	5	7	11	—
524288	5	7	10	—
1179648	5	7	10	21
2097152	5	7	10	18

Table 4.14: The number of iterations in the conjugate gradient method corresponding to Table 4.12.

N \ ϵ	1.0e–1	7.0e–2	5.0e–2	3.0e–2
2768	2	6	—	—
5824	2	3	13	—
15224	2	2	4	—
50464	2	2	3	8

Table 4.15: The number of iterations in the conjugate gradient method corresponding to Table 4.13.

N \ ϵ	1.0e–1	7.0e–2	5.0e–2	3.0e–2
4608	1.3e–1	—	—	—
8192	8.8e–2	—	—	—
18432	1.9e–1	7.1e–1	—	—
32768	4.0e–1	7.0e–1	—	—
73728	8.9e–1	1.3e+0	3.1e+0	—
131072	2.0e+0	2.4e+0	4.1e+0	—
294912	4.4e+0	6.0e+0	9.5e+0	—
524288	8.2e+0	1.2e+1	1.6e+1	—
1179648	1.7e+1	2.2e+1	3.2e+1	6.2e+1
2097152	3.4e+1	5.1e+1	6.5e+1	8.6e+1

Table 4.16: The CPU times corresponding to Table 4.12, but with external field $H_{ext} = (0.3, 0.1)$.

N \ ϵ	1.0e–1	7.0e–2	5.0e–2	3.0e–2
2768	7.4e–2	2.0e–1	—	—
5824	2.0e–1	2.4e–1	8.0e–1	—
15224	7.1e–1	7.1e–1	1.3e+0	—
50464	1.7e+0	1.6e+0	2.7e+0	5.9e+0

Table 4.17: The CPU times corresponding to Table 4.13, but with external field $H_{ext} = (0.3, 0.1)$.

N \ ϵ	1.0e–1	7.0e–2	5.0e–2	3.0e–2
4608	17	—	—	—
8192	6	—	—	—
18432	6	17	—	—
32768	5	9	—	—
73728	5	8	16	—
131072	5	7	12	—
294912	5	7	11	—
524288	5	7	10	—
1179648	5	7	10	16
2097152	5	7	10	14

Table 4.18: The number of iterations in the conjugate gradient method corresponding to Table 4.16.

N \ ϵ	1.0e–1	7.0e–2	5.0e–2	3.0e–2
2768	2	7	—	—
5824	2	3	11	—
15224	2	2	4	—
50464	2	2	3	9

Table 4.19: The number of iterations in the conjugate gradient method corresponding to Table 4.17.

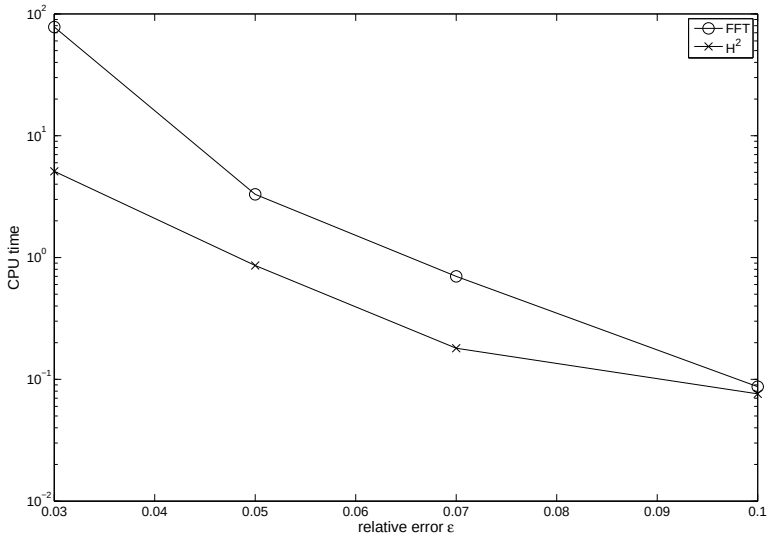

Figure 4.14: The plot shows the relation between the prescribed relative error ϵ and the minimal CPU time listed in Tables 4.12 and 4.13. The lower curve corresponds to the $\mathcal{H}^2$–matrix method, the upper one to the FFT–based algorithm. The CPU time (in seconds) is displayed logarithmically in the vertical axis.

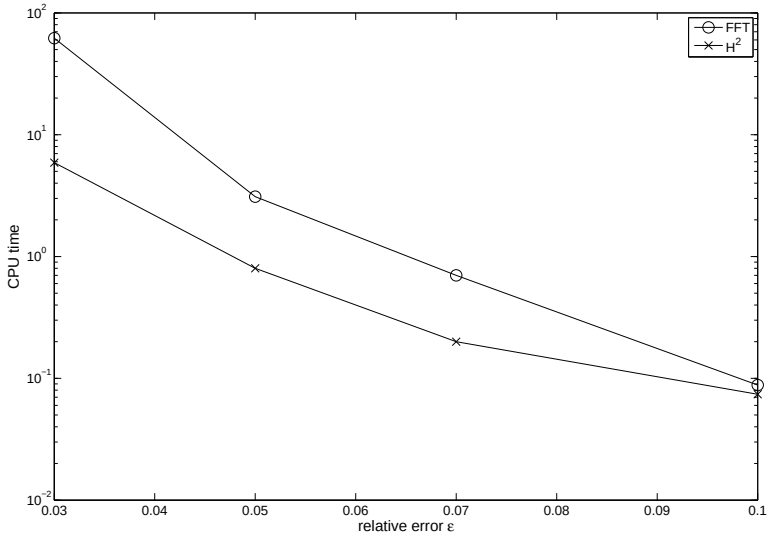

Figure 4.15: Relation between the prescribed relative error ϵ and the minimal CPU time listed in Tables 4.16 and 4.17. Notation as in Figure 4.14.

A further remark on the computation of ϵ must be added in the case of the $\mathcal{H}^2$–matrix method. Since in this method the evaluation of the energy E in (4.132) is based on the approximate matrix $\tilde{K}$, we actually calculate only an approximation $\tilde{\epsilon}$ to ϵ. To test the deviation numerically, we compute the exact energy norm distance ϵ of solutions σ_h to σ^* with the help of the full matrix K in the case of a prescribed relative error of 5% and $H_{ext} = (0.2, 0.2)$. Table 4.20 shows that the deviation does not exceed 1%, which coincides with our numerical results in Table 4.10.

N	ϵ	$\tilde{\epsilon}$
5824	9.1e–2	1.0e–1
15224	8.4e–2	9.5e–2
50464	7.4e–2	8.5e–2

Table 4.20: Comparison of the prescribed relative error ϵ and its approximation $\tilde{\epsilon}$ in the $\mathcal{H}^2$–matrix method: the deviation does not exceed 1%.

Figure 4.16 shows the graph of a solution σ_h on a triangulation $\mathcal{T}_h$ with $N = 5824$ and prescribed relative error of 5%. The external field is $H_{ext} = (0.2, 0.2)$. For the convenience of the reader the piecewise constant function σ_h has been linearly interpolated by the MATLAB PDE Toolbox.

In Figure 4.17 we compare the performance of a single matrix–vector multiplication Kz for the two matrix compression methods on triangulations $\mathcal{Q}_h$. As non–trivial vector z we take the solution of the FFT–based conjugate gradient method computed

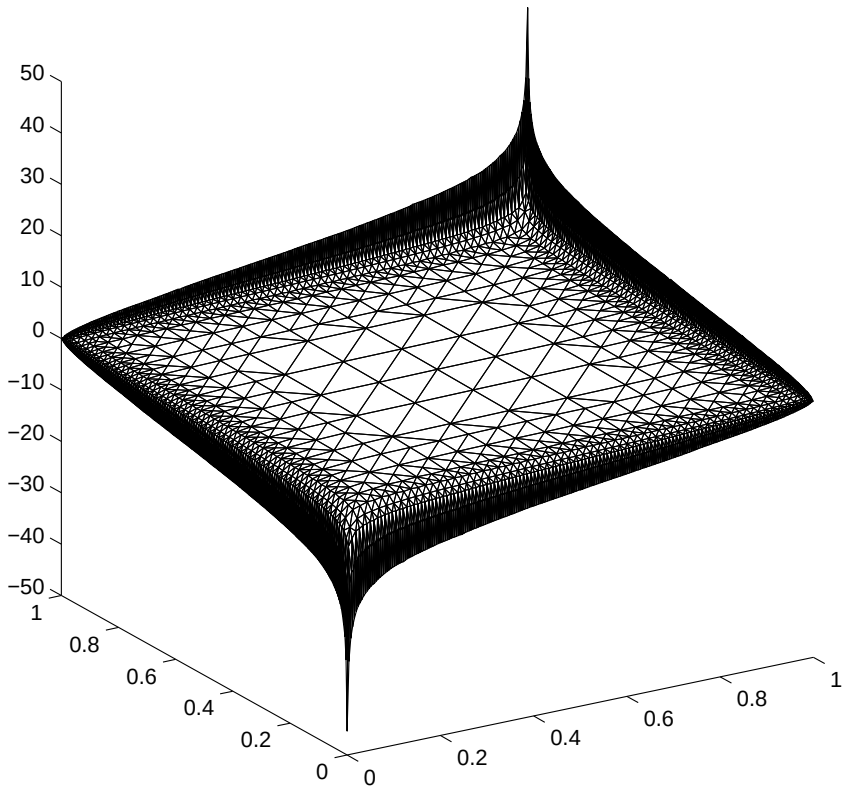

Figure 4.16: Graph of a solution σ_h (linearly interpolated) on triangulation $\mathcal{T}_h$. The number of triangles is $N = 5824$, the external field is $H_{ext} = (0.2, 0.2)$, and the prescribed relative error is 5%.

above (see Table 4.12). Here the FFT–based method is *exact* up to rounding errors, whereas the $\mathcal{H}^2$–matrix method computes an approximate solution $\tilde{K}z$. Figure 4.18 shows the relative error

$$\epsilon \;=\; \sqrt{\frac{z^T K z - z^T \tilde{K} z}{z^T K z}}$$

between the corresponding exact and approximate quadratic form evaluated on z. This is the value of interest in our applications since $z^T K z$ is the discretized version of the stray field energy.

As expected, the FFT–based method beats the $\mathcal{H}^2$–matrix method since for triangulations $\mathcal{Q}_h$ the Toeplitz–type structure is a much stronger property than the block structure of the $\mathcal{H}^2$–matrix induced by the (mesh–independent) self–similarity in the decay of the kernel function. Moreover, we take advantage of a highly optimized FFT implementation [24] achieving practically optimal complexity over the range accessible in our numerical experiments.

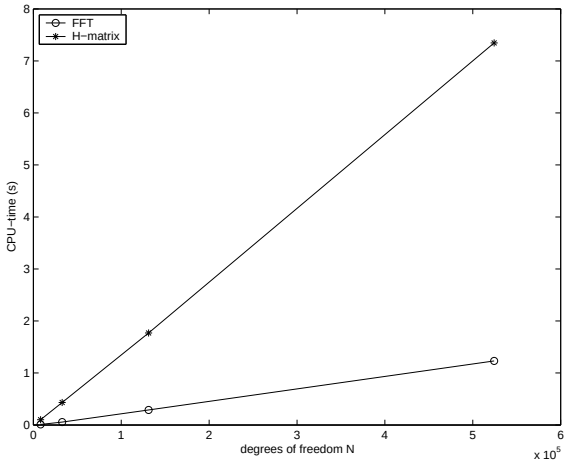

Figure 4.17: CPU time (in seconds) required for matrix–vector multiplication with the fully populated matrix K on triangulations of type $\mathcal{Q}_h$: here the FFT methods beats the $\mathcal{H}^2$–matrix method.

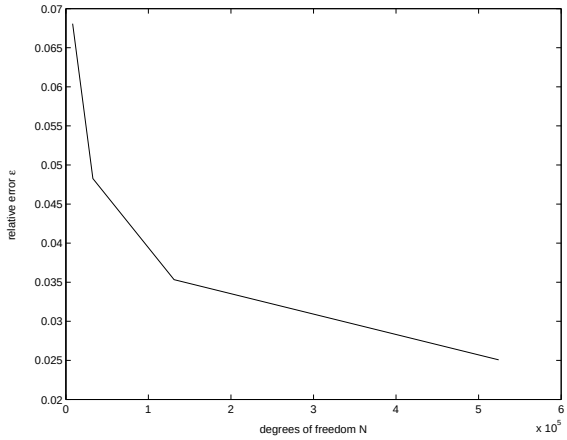

Figure 4.18: Relative error of $\mathcal{H}^2$ matrix–vector product corresponding to above Figure 4.17.

All numerical experiments were done on a Pentium III processor running at 700 MHz.

5 Computation of Minimizers

We suppress all primes for the two–dimensional variables in the following, since our considerations are restricted to the cross–section of the thin film.

5.1 Convex Programming Problems

In the field of mathematical programming, our problem of constrained minimization (3.26) belongs to the broad class of *convex programming problems*. For an elaborate introduction we refer the reader to the classical textbook [23, Chapter 6] and the recent monograph [44]. Here we briefly recall the basic notions, definitions and facts we need. The generic statement of a convex programming problem is as follows:

Let $f : \mathbb{R}^n \to \mathbb{R}$ be a convex function (the so–called *objective function*) and let the inequality constraints that restrict the acceptable arguments for f be given by a mapping $c : \mathbb{R}^n \to \mathbb{R}^k$, where each component function c_i, $i = 1, .., k$ is assumed to be concave. The *feasible region* $\mathcal{F}$ is then defined as

$$\mathcal{F} \ := \ \{x \in \mathbb{R}^n \mid c(x) \ \geq \ 0\} \ ,$$

where the relation $c(x) \geq 0$ is to be understood componentwise, i. e. we have $c_i(x) \geq 0$ for each $i = 1, .., k$. A point $x \in \mathcal{F}$ is called a *feasible point*.

The goal of convex programming is to find a feasible point $x^* \in \mathcal{F}$ such that

$$f(x^*) \ = \ \min_{x \in \mathcal{F}} f(x) \ . \tag{5.1}$$

Since the objective function is convex and the feasible region defines a convex set, every local minimum of f in $\mathcal{F}$ is a global minimum.

The *strictly feasible region* is given by

$$\text{strict}(\mathcal{F}) \ := \ \{x \in \mathbb{R}^n \mid c(x) \ > \ 0\} \ .$$

In most applications $\text{strict}(\mathcal{F})$ will be just the interior of $\mathcal{F}$, but there are examples where equality fails, e. g. consider the set $\mathcal{F} = \{(x_1, x_2) \in \mathbb{R}^2 \mid x_1^2 + x_2^2 \geq 0\}$.

A constraint c_i is called *active* at x^*, if $c_i(x^*) = 0$. In general, at least one constraint will be active at a minimizer x^* (otherwise it is not reasonable to state (5.1) as a constrained minimization problem at all) and so for generic minimizers we have $x^* \notin \text{strict}(\mathcal{F})$. This means that in general a solution to (5.1) will be a boundary point of $\text{strict}(\mathcal{F})$. From a geometrical point of view two basic strategies to solve (5.1) can be distinguished:

- approximate x^* by a sequence of iterates that lie on the boundary of $\text{strict}(\mathcal{F})$; for the case of linear f and c this leads to the famous *simplex method*;
- approximate x^* by a sequence of iterates that lie in the interior of $\text{strict}(\mathcal{F})$; this leads to the class of *interior point methods* (IPM).

Before discussing the definition and implementation of an interior point method in detail, we restate problem (3.26) in the language of convex programming. In our case the reduced micromagnetic energy E defined on $RT_{0,h}$ according to (3.24) takes the role of the objective function f.

In order to establish a *finite* number of constraints we will introduce a discrete subset $\mathcal{S}_h = \{x_1, .., x_k\} \subset \overline{\Omega}$.

Definition 5.1. *Let the set of* barrier points $\mathcal{S}_h = \{x_1, .., x_k\} \subset \overline{\Omega}$ *be given such that for any* $T \in \mathcal{T}_h$ *there exists at least one* $x_i \in \mathcal{S}_h$ *with* $x_i \in T$.

For each $i = 1, .., k$ we define the pointwise constraint function

$$c_i(m_h) \;=\; 1 - |m_h(x_i)|^2 \;. \tag{5.2}$$

Thus the feasible region $\mathcal{F}_h$ is given by

$$\mathcal{F}_h \;=\; \{m_h \in RT_{0,h} \mid c(m_h) \geq 0\} \tag{5.3}$$

and the strictly feasible region by

$$\text{strict}(\mathcal{F}_h) \;=\; \{m_h \in RT_{0,h} \mid c(m_h) > 0\} \;. \tag{5.4}$$

In our setting the convex programming problem (5.1) thus reads: find a feasible magnetization $m_h^* \in \mathcal{F}_h$ such that

$$E(m_h^*) \;=\; \min_{m_h \in \mathcal{F}_h} E(m_h) \;. \tag{5.5}$$

Lemma 5.1. *For any* $C > 0$ *and with* $\mathcal{S}_h$ *as in Definition 5.1, the level set*

$$\mathcal{L}_h(C) \;:=\; \{m_h \in \mathcal{F}_h \mid E(m_h) \leq C\}$$

is bounded. In particular, $\mathcal{L}_h(C)$ *is compact.*

Proof of Lemma 5.1.
For a fixed triangulation $\mathcal{T}_h$ (and fixed paramter $h > 0$) the boundedness of the energy $E(m_h)$ as defined in (3.24) implies the existence of a constant $C_1 \geq 0$, such that

$$|\nabla \cdot m_h| \;\leq\; C_1$$

for all $m_h \in \mathcal{L}_h(C)$. Here C_1 depends on h and C, but not on m_h. Moreover, for $\mathcal{S}_h$ as in Definition 5.1, there exists at least one point $x_T \in T$ for each triangle $T \in \mathcal{T}_h$, such that

$$|m_h(x_T)| \;\leq\; 1 \;.$$

From Lemma 3.1 it thus follows that

$$\sup_{x \in \Omega} |m_h(x)|^2 \;\leq\; \tfrac{1}{2} C_1^2 \,\text{diam}(\Omega)^2 + 2$$

for all $m_h \in \mathcal{L}_h(C)$. This proves that $\mathcal{L}_h(C)$ is bounded for any $C > 0$. □

Since the reduced energy E is degenerate with respect to the divergence of m_h, (5.5) is a convex programming problem with non–unique optima. Therefore it is convenient to define the following *optimality region* $\mathcal{F}_h^*$ in $\mathcal{F}_h$:

$$\mathcal{F}_h^* \;=\; \{m_h^* \in \mathcal{F}_h \mid E(m_h^*) = \min_{m_h \in \mathcal{F}_h} E(m_h)\} \;, \tag{5.6}$$

i. e. $\mathcal{F}_h^*$ is the set of all solutions to (5.5).

Definition 5.2. *A constraint function c_i, $i \in I = \{1, .., k\}$ is called* universally binding at optimality *if*

$$c_i(m_h^*) \;=\; 0 \qquad \textit{for all } m_h^* \in \mathcal{F}_h^* \;.$$

If there exists at least one constraint function that is universally binding at optimality, then we denote by I^* the subset of indices i for which c_i is universally binding at optimality, i. e. we have

$$c_i(m_h^*) \;=\; 0$$

for all $i \in I^*$ and all $m_h^* \in \mathcal{F}_h^*$. If there exists at least one constraint function that is not *universally binding at optimality, then we denote by I^+ the subset of indices i for which c_i is* not *universally binding at optimality. Obviously, $I = I^* \cup I^+$ and $I^* \cap I^+ = \emptyset$. By the shorthand notation $I = I^*$ we designate the case in which* all *constraint functions are universally binding at optimality. Otherwise we use the shorthand notation $I \neq I^*$. Furthermore, we denote by c^* the subvector of constraint functions c_i with $i \in I^*$, and by c^+ the subvector of constraint functions c_i with $i \in I^+$.*

Definition 5.3. *A solution m_h^* of* (5.5) *is called* strongly optimal *if the only active constraints at m_h^* are those which are universally binding at optimality, i. e. we are either in the case $I = I^*$ in the sense of Definition 5.2, or the subvector c^+ has strictly positive entries at m_h^*,*

$$c^+(m_h^*) \;>\; 0 \;.$$

Lemma 5.2. *For $\mathcal{S}_h$ as in Definition 5.1, the regions $\mathcal{F}_h$,* strict$(\mathcal{F}_h)$*, and $\mathcal{F}_h^*$ are nonempty. Furthermore, $\mathcal{F}_h^*$ is bounded.*

Proof of Lemma 5.2.
For the zero magnetization $m_h \equiv 0$ we have $m_h \in \mathcal{F}_h$ as well as $m_h \in$ strict$(\mathcal{F}_h)$, thus both regions are nonempty.

Since $0 \in \mathcal{F}_h$, and the reduced energy E vanishes for the zero magnetization, we have for the optimality region (5.6)

$$\mathcal{F}_h^* \;\subset\; \mathcal{L}_h(0) \;=\; \{\, m_h \in \mathcal{F}_h \mid E(m_h) \leq 0 \,\} \;\neq\; \emptyset \;.$$

Now the level set $\mathcal{L}_h(0)$ is bounded and compact by Lemma 5.1, and so there exists at least one solution to problem (5.5), i. e. $\mathcal{F}_h^* \neq \emptyset$.

Moreover, as we have just seen, the optimality region $\mathcal{F}_h^*$ is bounded. □

5.2 Constraint Qualifications

Convergence results for IPMs require additional conditions on the constraints:

Remark 5.1. *The property*

$$\text{strict}(\mathcal{F}_h) \neq \emptyset \tag{5.7}$$

is called Slater's constraint qualification *[40, Definition 5.4.3]. It allows to establish necessary and sufficient conditions for the solutions of* (5.5)*, which is the content of the* Kuhn–Tucker theorem*, Theorem 5.1 below.*

The derivative of a constraint function c_i at m_h acting on a basis function φ_h of $RT_{0,h}$ is computed as

$$Dc_i(m_h)\varphi_h \;=\; -2\, m_h(x_i) \cdot \varphi_h(x_i) \;.$$

Thus the gradient of c_i at m_h with respect to the basis $\{\varphi_h^{(j)}\}_{j=1,..,n}$ of $RT_{0,h}$ is given as the vector $\nabla c_i(m_h)$ with components

$$(\,\nabla c_i(m_h)\,)_j \;=\; Dc_i(m_h)\varphi_h^{(j)} \;, \qquad j = 1,..,n \;.$$

Let us further define the $n \times k$–matrix A of the constraint gradients at m_h by

$$A(m_h) \;=\; \tfrac{1}{2}\,(\,\nabla c_1(m_h)\;\nabla c_2(m_h)\;..\;\nabla c_k(m_h)\,) \;. \tag{5.8}$$

Theorem 5.1. *[51, Theorem 6.6.5] The feasible point $m_h^* \in \mathcal{F}_h$ is a solution to* (5.5) *if and only if there exists a vector $\lambda^* \in \mathbb{R}^k$ with $\lambda^* \geq 0$ such that the following* Kuhn–Tucker conditions *hold:*

$$\lambda^{*T} c(m_h^*) \;=\; 0 \quad \textit{and} \tag{5.9}$$

$$\nabla E(m_h^*) \;=\; A(m_h^*)\lambda^* \;. \tag{5.10}$$

The complementarity condition (5.9) means that for each $i = 1,..,k$ at least one of the two corresponding components $c_i(m_h^*)$ and λ_i^* vanishes. In particular, if the ith constraint is inactive at m_h^*, then λ_i^* must be zero. Thus $\nabla E(m_h^*)$ is a linear combination of the active constraint gradients and we can rewrite (5.10) as

$$\nabla E(m_h^*) \;=\; \hat{A}(m_h^*)\lambda^* \;,$$

where the matrix $\hat{A}(m_h^*)$ originates from the original matrix $A(m_h^*)$ by cancelling those columns $\nabla c_i(m_h^*)$ with $c_i(m_h^*) > 0$.

For *strictly* feasible points the Kuhn–Tucker Theorem therefore reduces to:

Corollary 5.1. *A strictly feasible point $m_h^* \in \text{strict}(\mathcal{F}_h)$ is a solution to* (5.5) *if and only if it satisfies*

$$\nabla E(m_h^*) \;=\; 0 \;.$$

The Lagrange multiplier λ^* is in general not unique, since the columns of the matrix $\hat{A}(m_h^*)$ are not necessarily linear independent at a minimizer m_h^*. This is illustrated by the following example.

Consider the patch of triangles in Figure 5.1. The volume of each triangle is given by $|T| = h^2/4$. If we set $a_0 = a_4$ and $a_5 = a_1$, then the evaluation of the basis functions $\varphi_h^{(i)}$ at the barycenters x_i, $i = 1, .., 4$, gives

$$\varphi_h^{(i)}(x_i) \;=\; \frac{2}{h^2}\,(x_i - a_{i-1}) \;\; .$$

For the magnetization $m_h|_{T_i} = m_h(x_i) = \frac{1}{h}(a_i - a_{i-1})$ we thus get

$$\varphi_h^{(i)}(x_i) \cdot m_h(x_i) \;=\; \frac{2}{h^3}\,(x_i - a_{i-1}) \cdot (a_i - a_{i-1}) \;=\; \frac{1}{h}$$

for all $i = 1, .., 4$. Analogously one computes

$$\varphi_h^{(i)}(x_{i+1}) \cdot m_h(x_{i+1}) \;=\; \frac{1}{h} \;\; ,$$

if we set $x_5 = x_1$. Thus $\det \hat{A}(m_h) = 0$, since $\hat{A}(m_h)$ has the form

$$\hat{A}(m_h) \;=\; -h^{-1} \begin{pmatrix} 1 & 1 & 0 & 0 \\ 0 & 1 & 1 & 0 \\ 0 & 0 & 1 & 1 \\ 1 & 0 & 0 & 1 \end{pmatrix} \;\; .$$

It is easily checked that $m_h \in RT_{0,h}$, and so this example shows that the Lagrange multiplier is in general not unique.

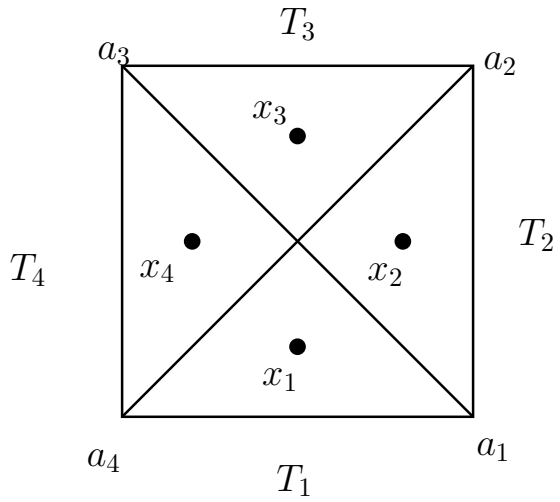

Figure 5.1: On this patch we discuss the role of above constraint qualifications.

5.3 The Interior Point Method

We compute a solution to (5.5) by an *interior point method* (IPM). The main idea of an interior point algorithm is to convert the constrained minimization (5.5) into a sequence of unconstrained minimization problems. For this purpose we introduce the composite functions

$$E_t(m_h) \;:=\; E(m_h) + tB(m_h)\;, \tag{5.11}$$

defined for every real parameter $t > 0$. Here B denotes a so–called *barrier*, i. e. a function on $\mathcal{F}_h$ that exhibits a positive singularity at the boundary of strict($\mathcal{F}_h$). So the composite functions E_t balance the minimization of E as well as the impact of the constraints. When the so–called *barrier parameter* t is reduced, the weighting of the barrier is decreased and the minimizers of the composite functions can approach the boundary. Thus we expect the unconstrained minimizers to converge to a solution of the constrained problem as t is reduced to zero, in particular

$$\lim_{t\downarrow 0} \min E_t \;=\; \min_{\mathcal{F}_h} E\;. \tag{5.12}$$

Such a convergence result can be established under rather mild conditions, see Theorem 5.2.

For our concrete problem we choose a logarithmic barrier, i. e. for each $x_i \in \mathcal{S}_h \cap T$ we define the pointwise barrier function

$$B_i(m_h) \;=\; -\tfrac{1}{2}|T| \log c_i(m_h) \;=\; -\tfrac{1}{2}|T| \log(1 - |m_h(x_i)|^2)\;,$$

and summation over all $i = 1, .., k$ gives the global barrier

$$B(m_h) = \sum_{i=1}^{k} B_i(m_h)\;. \tag{5.13}$$

One easily computes the first derivatives

$$DB_i(m_h)u_h \;=\; |T|\;\frac{m_h(x_i)\cdot u_h(x_i)}{1 - |m_h(x_i)|^2} \tag{5.14}$$

and the second derivatives

$$\frac{1}{|T|}D^2B_i(m_h)(u_h, v_h) \;=\; \frac{u_h(x_i)\cdot v_h(x_i)}{1 - |m_h(x_i)|^2} \;+\; 2\;\frac{m_h(x_i)\cdot u_h(x_i)}{(1 - |m_h(x_i)|^2)^2}\; m_h(x_i)\cdot v_h(x_i)\;, \tag{5.15}$$

where $u_h, v_h \in RT_{0,h}$ are test functions and the dot $\cdot$ denotes the euclidean scalar product in $\mathbb{R}^2$. By inserting the basis functions $\varphi_h^{(i)}$ of $RT_{0,h}$ as test functions we get the gradient and the Hessian of the barrier. So $\nabla B(m_h)$ is the vector with components

$$(\,\nabla B(m_h)\,)_i \;=\; DB(m_h)\varphi_h^{(i)}\;, \qquad i = 1, .., n\;, \tag{5.16}$$

and $\mathrm{Hess}B(m_h)$ is the matrix with entries

$$(\,\mathrm{Hess}B(m_h)\,)_{ij} \;=\; D^2B(m_h)(\varphi_h^{(i)},\varphi_h^{(j)})\;. \tag{5.17}$$

Notice that $\mathrm{Hess}B(m_h)$ is a sparse $n\times n$ matrix due to the locality of the basis functions.

Obviously, the composite function E_t is defined only in $\mathrm{strict}(\mathcal{F}_h)$ since the barrier B becomes singular at the boundary of $\mathrm{strict}(\mathcal{F}_h)$.

In correspondence to the definitions (3.31),(3.32),(5.16) and (5.17) we have

$$\nabla E_t(m_h) \;=\; \nabla E(m_h) + t\;\nabla B(m_h)$$

and

$$\mathrm{Hess}E_t(m_h) \;=\; \mathrm{Hess}E + t\;\mathrm{Hess}B(m_h)\;.$$

Notice that $\mathrm{Hess}E_t(m_h)$ differs from $\mathrm{Hess}E$ only by the additional term $t\,\mathrm{Hess}B(m_h)$, but since $\mathrm{Hess}B(m_h)$ depends explicitly on m_h, so does $\mathrm{Hess}E_t(m_h)$. Furthermore, $\mathrm{Hess}E_t(m_h)$ is a fully populated matrix.

5.4 The Primal Path

Lemma 5.3. *For every $m_h\in\mathrm{strict}(\mathcal{F}_h)$ and any $t>0$, the matrix $\mathrm{Hess}E_t(m_h)$ is positive definite. In particular, for fixed $t>0$ the function E_t is strictly convex and has a unique minimizer $m_h(t)$ on $\mathrm{strict}(\mathcal{F}_h)$.*

Proof of Lemma 5.3.
For $\mathcal{S}_h$ given as in Definition 5.1 there exists at least one point $x_T\in\mathcal{S}_h\cap T$ for each triangle $T\in\mathcal{T}_h$. In particular, for every $u_h\in RT_{0,h}$ we have by Lemma 3.1 the estimate

$$\sup_{x\in T}|u_h(x)|^2 \;\le\; \tfrac{1}{2}|(\nabla\cdot u_h)(T)|^2\,\mathrm{diam}(T)^2 + 2|u_h(x_T)|^2\;, \tag{5.18}$$

where $(\nabla\cdot u_h)(T)$ denotes the uniquely defined value of the piecewise constant function $\nabla\cdot u_h$ on T.

Since the matrix K in (3.27) is positive definite, there exists a constant $C>0$ such that

$$D^2E(m_h)(u_h,u_h) \;\ge\; C\sum_{T\in\mathcal{T}_h}|(\nabla\cdot u_h)(T)|^2 \tag{5.19}$$

for all $u_h, m_h\in RT_{0,h}$. Due to the additional assumption $m_h\in\mathrm{strict}(\mathcal{F}_h)$ we get from (5.15) the inequality

$$D^2B(m_h)(u_h,u_h) \;\ge\; \sum_{T\in\mathcal{T}_h}|T|\;|u_h(x_T)|^2\;, \tag{5.20}$$

since for any $i=1,..,k$ there holds

$$\frac{1}{|T|}D^2B_i(m_h)(u_h,u_h) \;\ge\; |u_h(x_i)|^2 + 2|m_h(x_i)\cdot u_h(x_i)|^2 \;\ge\; |u_h(x_i)|^2\;.$$

Combining (5.19) and (5.20) yields

$$D^2E_t(m_h)(u_h,u_h) \;\geq\; C\sum_{T\in\mathcal{T}_h}|(\nabla\cdot u_h)(T)|^2 + t\sum_{T\in\mathcal{T}_h}|T|\;|u_h(x_T)|^2\;.$$

Now let $t>0$ be fixed. By (5.18) we conclude that there exists a constant $\tilde{C}>0$ that depends not on m_h or u_h, such that

$$D^2E_t(m_h)(u_h,u_h) \;\geq\; \tilde{C}\sum_{T\in\mathcal{T}_h}\sup_{x\in T}|u_h(x)|^2\;.$$

(We note that for a fixed triangulation $\mathcal{T}_h$ the diameter and the area of all triangles $T\in\mathcal{T}_h$ is bounded from below by a positive constant.) Therefore $\mathrm{Hess}E_t(m_h)$ is positive definite. □

Since $\{E_t\}_{t>0}$ is a family of strictly convex and coercive functions which depends continuously on the barrier parameter $t>0$, the family of unique minimizers $m_h(t)$ given by Lemma 5.3 itself depends continuously on $t>0$. Thus we can interpret the set $\{m_h(t)\}_{t>0}$ geometrically as a kind of trajectory, which we call in the following the *primal path*.

The intuitive basis of IPM presented so far is justified by a convergence result due to [23, Theorem 25], which takes the following form in view of Lemma 5.3:

Theorem 5.2. *Let $E_t : \mathrm{strict}(\mathcal{F}_h)\to\mathbb{R}$ be defined as in (5.11) with the barrier B given by (5.13). Then the primal path $\{m_h(t)\}_{t>0}$ defined by Proposition 5.3 has the following properties:*

1. $\lim_{t\downarrow 0}E(m_h(t)) = \lim_{t\downarrow 0}E_t(m_h(t)) = \min_{\mathcal{F}_h}E$;
2. *every accumulation point of $m_h(t)$ for $t\downarrow 0$ solves the convex programming problem (5.5);*
3. *$E_t(m_h(t))$ is a monotonically decreasing function in $t>0$;*
4. *$E(m_h(t))$ is a monotonically decreasing function in $t>0$;*
5. *$B(m_h(t))$ is a monotonically increasing function in $t>0$.*

5.5 The Analytic Center

Theorem 5.2 guarantees only the convergence of the function values $E(m_h(t))$ and $E_t(m_h(t))$, but it does not make any prediction about the convergence of the primal path $\{m_h(t)\}_{t>0}$ itself. If the optimality region $\mathcal{F}_h^*$ would consist only of a single point, convergence of the primal path for $t\downarrow 0$ would follow directly from Theorem 5.2. But since there exist multiple optimal solutions to our problem (5.5), the following two questions arise:

- does a unique limit of the primal path $\{m_h(t)\}_{t>0}$ exist, and if so,

- how can we characterize that particular optimal solution to (5.5)?

These questions were answered in [41], based on the notion of *analytic centers of the optimality region.* We present these results and the related proofs in some detail, since the concept of analytic centers allows us to proof a stability estimate for weak external fields in the succeeding section.

Lemma 5.4. *Let $\underline{m}_h, \overline{m}_h \in \mathrm{strict}(\mathcal{F}_h)$ be given with $\underline{m}_h \neq \overline{m}_h$. If*

$$\log c_i(\lambda\overline{m}_h + (1-\lambda)\underline{m}_h) \;=\; \lambda \log c_i(\overline{m}_h) + (1-\lambda)\log c_i(\underline{m}_h) \tag{5.21}$$

for all $0 < \lambda < 1$ and a constraint function c_i, then $c_i(\lambda\overline{m}_h + (1-\lambda)\underline{m}_h)$ is constant as a function of $\lambda \in \mathbb{R}$.

Proof of Lemma 5.4.
Since $c_i(\underline{m}_h) > 0$ for $\underline{m}_h \in \mathrm{strict}(\mathcal{F}_h)$, (5.21) implies

$$c_i(\lambda\overline{m}_h + (1-\lambda)\underline{m}_h) \;=\; \left(\frac{c_i(\overline{m}_h)}{c_i(\underline{m}_h)}\right)^{\lambda} c_i(\underline{m}_h) \;=\; c_i(\underline{m}_h) e^{\lambda \log\left(\frac{c_i(\overline{m}_h)}{c_i(\underline{m}_h)}\right)} \;. \tag{5.22}$$

Now c_i is a positive concave function on $\mathrm{strict}(\mathcal{F}_h)$, but the exponential function on the righthand side of (5.22) is convex in λ. Thus we must have

$$\frac{c_i(\overline{m}_h)}{c_i(\underline{m}_h)} \;=\; 1 \;,$$

and $c_i(\lambda\overline{m}_h+(1-\lambda)\underline{m}_h)$ is constant for $0 < \lambda < 1$. But since $\lambda \mapsto c_i(\lambda\overline{m}_h+(1-\lambda)\underline{m}_h)$ is an analytic function, it is constant for all $\lambda \in \mathbb{R}$. □

Lemma 5.5. *If $I = I^*$ in the sense of Definition 5.2, then $\mathcal{F}_h^*$ consists of a single point.*

Proof of Lemma 5.5.
We argue by contradiction. Let us assume that there exist $\underline{m}_h, \overline{m}_h \in \mathcal{F}_h^*$ with $\underline{m}_h \neq \overline{m}_h$. Since $\mathcal{F}_h^*$ is convex, we have $[\underline{m}_h, \overline{m}_h] \subset \mathcal{F}_h^*$ for the line segment

$$[\underline{m}_h, \overline{m}_h] \;:=\; \{\lambda\overline{m}_h + (1-\lambda)\underline{m}_h \mid 0 \leq \lambda \leq 1\} \;.$$

In particular, E is constant on $[\underline{m}_h, \overline{m}_h]$ and $c^* = c$ vanishes on $[\underline{m}_h, \overline{m}_h]$ by assumption. But since E and c^* are analytic, this means that E is constant and $c^* = c$ vanishes on the unbounded line

$$L \;:=\; \{\lambda\overline{m}_h + (1-\lambda)\underline{m}_h \mid \lambda \in \mathbb{R}\} \;.$$

Therefore $L \subset \mathcal{F}_h^*$, but this contradicts the boundedness of the optimality region $\mathcal{F}_h^*$ due to Lemma 5.2. □

Due to Lemma 5.5, we may concentrate on the case $I \neq I^*$. By introducing the shorthand notation

$$B(m_h) \;=\; -\tfrac{1}{2}\sum |T| \log c(m_h) \tag{5.23}$$

for the logarithmic barrier defined in (5.13), we may split in view of Definition 5.2 the contributions to the summation in (5.23),

$$B(m_h) \;=\; B^*(m_h) + B^+(m_h) \;,$$

where

$$B^*(m_h) \;:=\; -\tfrac{1}{2}\sum |T| \log c^*(m_h) \quad \text{and} \quad B^+(m_h) \;:=\; -\tfrac{1}{2}\sum |T| \log c^+(m_h) \;,$$

provided both subvectors exist and $m_h \in \text{strict}(\mathcal{F}_h)$. Note that $B^+(m_h)$ is also well–defined if $m_h \in \mathcal{F}_h^*$ is a *strongly* optimal solution in the sense of Definition 5.3. If c^+ is not strictly positive at m_h, i. e. $c^+(m_h)$ has vanishing entries, then we set

$$B^+(m_h) \;:=\; +\infty \;.$$

Lemma 5.6. *If $I \neq I^*$ in the sense of Definition 5.2, then there exists at least one $m_h \in \mathcal{F}_h^*$, such that*

$$B^+(m_h) \;<\; +\infty \;.$$

Proof of Lemma 5.6.
In view of Definition 5.2, for every $i \in I^+$ there exists $m_h^{(i)} \in \mathcal{F}_h^*$, such that

$$c_i(m_h^{(i)}) \;>\; 0 \;.$$

Now we set

$$m_h \;:=\; \frac{1}{\#I^+} \sum_{i \in I^+} m_h^{(i)} \;,$$

where $\#I^+$ denotes the cardinality of I^+. We have $m_h \in \mathcal{F}_h^*$ since $\mathcal{F}_h^*$ is convex, and $c^+(m_h) > 0$ since c^+ is concave. Thus $B^+(m_h) < +\infty$. □

Definition 5.4. *If $I \neq I^*$ in the sense of Definition 5.2, then we call any solution to the following minimization problem*

$$\min_{m_h \in \mathcal{F}_h^*} B^+(m_h) \tag{5.24}$$

an analytic center of the optimality region.

Lemma 5.7. *Let us assume $I \neq I^*$. Then the optimality region $\mathcal{F}_h^*$ of the convex programming problem* (5.5) *has a unique analytic center m_h^*. In particular, we have $c^+(m_h^*) > 0$.*

Proof of Lemma 5.7.
By Lemma 5.6 there exists $m_h \in \mathcal{F}_h^*$, such that

$$B^+(m_h) \;=:\; B_0 \;<\; +\infty \;.$$

Since the function B^+ is convex, the sublevel set

$$\mathcal{B}_h \;:=\; \{m_h \in \mathcal{F}_h^* \mid B^+(m_h) \leq B_0\}$$

is also convex. In particular, $\mathcal{B}_h \subset \mathcal{F}_h^*$ is compact, and therefore B^+ attains its minimum on $\mathcal{B}_h$.

If $\mathcal{B}_h$ consists of a single point, then there is nothing else to show. Now let us assume that there exist at least two solutions $\underline{m}_h, \overline{m}_h \in \mathcal{B}_h$ to the minimization problem (5.24) with $\underline{m}_h \neq \overline{m}_h$. Since $\mathcal{B}_h$ is convex, we have $[\underline{m}_h, \overline{m}_h] \subset \mathcal{B}_h \subset \mathcal{F}_h^*$ for the line segment

$$[\underline{m}_h, \overline{m}_h] \ := \ \{\lambda \overline{m}_h + (1-\lambda)\underline{m}_h \mid 0 \leq \lambda \leq 1\} \ .$$

In particular, E is constant on $[\underline{m}_h, \overline{m}_h]$ and c^* vanishes on $[\underline{m}_h, \overline{m}_h]$. But this means that $E \equiv const$ and $c^* \equiv 0$ on the unbounded line

$$L \ := \ \{\lambda \overline{m}_h + (1-\lambda)\underline{m}_h \mid \lambda \in \mathbb{R}\} \ .$$

It remains to consider the constraints c^+. Since $\underline{m}_h$ and $\overline{m}_h$ are minimizers of the convex function B^+ on the convex set $\mathcal{B}_h$, the function B^+ is constant on the line segment $[\underline{m}_h, \overline{m}_h]$. But if the sum of convex functions is constant, then each individual function must be linear, thus the functions $\log c_i^+$ are linear on $[\underline{m}_h, \overline{m}_h]$ for each $i \in I^+$. But Lemma 5.4 implies, that these functions are indeed constant on the line L, therefore also the function B^+.

But this would imply $L \subset \mathcal{B}_h \subset \mathcal{F}_h^*$, which contradicts the boundedness of the optimality region $\mathcal{F}_h^*$. □

Theorem 5.3. *The primal path $\{m_h(t)\}_{t>0}$ converges to the unique analytic center m_h^* of the optimality region $\mathcal{F}_h^*$.*

Proof of Theorem 5.3.
We know from Lemma 5.7 that there exists a unique analytic center m_h^* of the optimality region $\mathcal{F}_h^*$. Moreover, m_h^* is strongly optimal, i. e. we have $c^+(m_h^*) > 0$. Now consider a sequence of barrier parameters $\{t_j\}_{j\in\mathbb{N}}$ with $t_j \downarrow 0$ as $j \to +\infty$. Applying Theorem 5.2, we may assume that (after eventually extracting a subsequence) $m_h(t_j)$ converges to the point $u_h^* \in \mathcal{F}_h^*$ as $j \to +\infty$.

Let us assume that $m_h^* \neq u_h^*$. Then we define for every j

$$v_h(t_j) \ := \ m_h(t_j) + m_h^* - u_h^* \ .$$

Since $m_h(t_j) \to u_h^*$ for $j \to +\infty$, we have

$$v_h(t_j) \ \to \ m_h^* \quad \text{as } j \to +\infty \ .$$

Moreover, by continuity of the constraint vectors c and c^+, it follows that

$$c^+(v_h(t_j)) \ > \ 0 \tag{5.25}$$

for j large enough. Since $\mathcal{F}_h^*$ is convex, we have $[u_h^*, m_h^*] \subset \mathcal{F}_h^*$ for the line segment

$$[u_h^*, m_h^*] \ := \ \{\lambda u_h^* + (1-\lambda) m_h^* \mid 0 \leq \lambda \leq 1\} \ .$$

In particular, E is constant on $[u_h^*, m_h^*]$ and c^* vanishes on $[u_h^*, m_h^*]$. But this means that $E \equiv const$ and $c^* \equiv 0$ on the unbounded line

$$L \ := \ \{\lambda u_h^* + (1-\lambda) m_h^* \mid \lambda \in \mathbb{R}\} \ .$$

Since $v_h(t_j) - m_h(t_j) = m_h^* - u_h^*$ by definition, the line segment $[m_h(t_j), v_h(t_j)]$ is parallel to $[u_h^*, m_h^*]$ for every j. According to Lemma 3.4 there holds

$$E(v_h(t_j)) \ = \ E(m_h(t_j)) \tag{5.26}$$

and

$$c^*(v_h(t_j)) \ = \ c^*(m_h(t_j)) \tag{5.27}$$

for every j. In particular, due to (5.25) and (5.27) we have $v_h(t_j) \in \text{strict}(\mathcal{F}_h)$ for j large enough, so the values of the barrier functions $B(v_h(t_j))$, $B^+(v_h(t_j))$ and $B^*(v_h(t_j))$ are well–defined for those indices j, and we can write

$$\begin{aligned}
& t_j B^+(v_h(t_j)) - t_j B^+(m_h(t_j)) \\
\overset{(5.27)}{=} \ & t_j B(v_h(t_j)) - t_j B(m_h(t_j)) \\
\overset{(5.26)}{=} \ & E(v_h(t_j)) - E(m_h(t_j)) + t_j B(v_h(t_j)) - t_j B(m_h(t_j)) \\
= \ & E_{t_j}(v_h(t_j)) - E_{t_j}(m_h(t_j)) \\
\geq \ & 0 \ .
\end{aligned}$$

In the last step we have used the fact that $m_h(t_j)$ is the minimizer of the strictly convex function E_{t_j} for each j.

Since $t_j > 0$ for every j, it follows that

$$B^+(v_h(t_j)) \geq B^+(m_h(t_j)) \ .$$

Due to the continuity of B^+, we get in the limit $j \to +\infty$

$$B^+(m_h^*) \geq B^+(u_h^*) \ .$$

But since m_h^* is the unique minimizer of B^+ on $\mathcal{F}_h^*$, we must have $m_h^* = u_h^*$, which completes the proof. □

5.6 A Stability Estimate

In the following, we assume that the set of barrier points $\mathcal{S}_h$ in Definition 5.1 is the set of all vertices of the triangulation $\mathcal{T}_h$. We denote this choice by

$$\mathcal{S}_h \ = \ \mathcal{S}_h^v \ . \tag{5.28}$$

This ensures the estimate

$$||m_h||_\infty \ < \ 1 \tag{5.29}$$

for every strictly feasible magnetization $m_h \in \text{strict}(\mathcal{F}_h)$. Note that in this case any vertex $x_0 \in \mathcal{S}_h$ has to be counted with multiplicity: since the elements of the finite element space $RT_{0,h}$ are in general not continuous at the vertices of the triangulation, we have to implement a total number of constraint functions c_i at x_0 that equals the number of triangles meeting there.

The following result is an immediate consequence of Corollary 5.1 and Definition 5.24.

Corollary 5.2. *The analytic center m_h^* satisfies the strict inequality*

$$||m_h^*||_\infty \ < \ 1$$

if and only if m_h^* solves the equality–constrained optimization problem

$$B(m_h^*) \ = \ \min_{\{m_h \in RT_{0,h} \ | \ \nabla E(m_h)=0\}} B(m_h) \tag{5.30}$$

with $B(m_h^*) < +\infty$.

Next we proof a type of stability estimate that ensures that the analytic center m_h^* is strictly feasible for sufficiently weak external field H_{ext}. The purpose of this statement is twofold: first, it justifies our assumption in Section 4.2 that for sufficiently weak external field H_{ext} the computation of the minimal energy E and the corresponding charge density σ_h reduces to the Dirichlet screen problem; second, it allows for a consistency check of the numerical results in Section 5.11 concerning our IPM implementation.

Lemma 5.8. *We assume* (5.28). *For every triangulation $\mathcal{T}_h$ there exists a positive constant $\delta > 0$, such that the analytic center m_h^* satisfies the strict inequality*

$$||m_h^*||_\infty \ < \ 1 \tag{5.31}$$

for all external fields $H_{ext} \in \mathbb{R}^2$ with $|H_{ext}| < \delta$.

Proof of Lemma 5.8.
We show that for sufficiently weak external H_{ext} there always exists a solution m_h to (5.5) that is strictly feasible. Inequality (5.31) then follows from the characterization of the analytic center in Definition 5.24. We start by taking a closer look at the optimality region $\mathcal{F}_h^*$.

From Lemma 3.3 we know that the quotient function $\tilde{E}$ is a strictly convex and coercive function on the quotient space $RT_{0,h}/\text{Ker}(\nabla\cdot)$. Based on the definition of the feasible region $\mathcal{F}_h$ in (5.3) we may now introduce a corresponding region

$$\tilde{\mathcal{F}}_h \ \subset \ RT_{0,h}/\text{Ker}(\nabla\cdot) \ ,$$

by demanding that for every equivalence class $\tilde{m}_h \in \tilde{\mathcal{F}}_h$ there exists at least one feasible $m_h \in \tilde{m}_h$ with $m_h \in \mathcal{F}_h$. By construction, $\tilde{\mathcal{F}}_h$ is convex. Thus $\tilde{E}$ has

a unique minimizer $\tilde{m}_h^*$ on $\tilde{\mathcal{F}}_h$. In particular, the optimality region (5.6) can be characterized as

$$\mathcal{F}_h^* \;=\; \mathcal{F}_h \cap \tilde{m}_h^* \;. \tag{5.32}$$

Since $\tilde{E}$ depends continuously on H_{ext}, so does $\tilde{m}_h^*$, where the induced topology of the quotient space $RT_{0,h}/\mathrm{Ker}(\nabla\cdot)$ is given for any norm $||\cdot||$ on $RT_{0,h}$ via the distance

$$|||\tilde{u}_h - \tilde{v}_h||| \;:=\; \min\{||u_h - v_h|| \mid u_h \in \tilde{u}_h,\; v_h \in \tilde{v}_h\} \tag{5.33}$$

for all $\tilde{u}_h, \tilde{v}_h \in RT_{0,h}/\mathrm{Ker}(\nabla\cdot)$.

We continue by considering the linear subspaces $\{m_h \in RT_{0,h} \mid \nabla E(m_h) = 0\}$ appearing in (5.30). According to (3.29), the condition $\nabla E(m_h) = 0$ is equivalent to

$$\int_{\mathbb{R}^2}\int_{\mathbb{R}^2} \nabla\cdot m_h(x) \frac{1}{4\pi|x-y|} \nabla\cdot m_h(y)\; dy\; dx \;=\; \int_\Omega H_{ext}\cdot m_h\; dx\;,$$

which in turn gives the estimate

$$||\nabla\cdot m_h||_V^2 \;\le\; ||m_h||_\infty\; |H_{ext}|\; |\Omega|\;.$$

Here we remind the definition of the V–norm in (2.5). Since the mapping $\tilde{m}_h \mapsto ||\nabla\cdot m_h||_V$, for any $m_h \in \tilde{m}_h$, is a well–defined norm on the finite–dimensional quotient space $RT_{0,h}/\mathrm{Ker}(\nabla\cdot)$, we conclude

$$|||\tilde{m}_h|||_\infty^2 \;\lesssim\; ||\nabla\cdot m_h||_V^2 \;\le\; ||m_h||_\infty\; |H_{ext}|\; |\Omega|\;,$$

where $|||\cdot|||_\infty$ has to be understood in the sense of (5.33). Since this inequality holds for any $m_h \in \tilde{m}_h$, we may choose m_h in view of (5.33) such that $|||\tilde{m}_h|||_\infty = ||m_h||_\infty$, and thus

$$||m_h||_\infty^2 \;\lesssim\; ||m_h||_\infty\; |H_{ext}|\; |\Omega|\;.$$

For sufficiently weak external field $|H_{ext}| \ll 1$ we therefore have

$$m_h \in \mathrm{strict}(\mathcal{F}_h) \quad \text{and} \quad \nabla E(m_h) = 0\;.$$

But in view of Corollary 5.1 this means that m_h is a solution to the convex programming problem (5.5), i. e.

$$m_h \;\in\; \mathcal{F}_h^*.$$

In particular, none of the constraint functions c_i is universally binding in the sense of Definition 5.2, so the subvector c^+ coincides with the total constraint vector c. By Lemma 5.7 the unique analytic center is therefore strictly feasible. □

5.7 The Dual Path

In this Section we introduce an a–priori bound for the deviation $E(m_h(t)) - E(m_h^*)$ for any given $t > 0$. We follow [23, Chapter 6.3].

From Lemma 5.3 we know that for each $t > 0$ the composite function E_t has a unique minimizer $m_h(t) \in \text{strict}(\mathcal{F}_h)$. Since the individual functions E and B are differentiable in $\text{strict}(\mathcal{F}_h)$, the minimizer solves the equation

$$\nabla E(m_h(t)) + t\,\nabla B(m_h(t)) \;=\; 0\ . \tag{5.34}$$

With (5.14) and (5.8) we get

$$\nabla E(m_h(t)) \;=\; \tfrac{1}{2}t \sum_{i=1}^{k} |T_i| \frac{\nabla c_i(m_h)}{c_i(m_h)} \;=\; A(m_h(t))\lambda(t)\ , \tag{5.35}$$

where $\lambda(t) \in \mathbb{R}^k$ is defined as the vector with components

$$(\lambda(t))_i \;:=\; \frac{t}{c_i(m_h(t))}|T_i| \;>\; 0\ . \tag{5.36}$$

We call $\{\lambda(t)\}_{t>0}$ the *dual path* that corresponds to the primal path $\{m_h(t)\}_{t>0}$. Modern IPMs are commonly based on the so–called primal–dual formulation [41]: the dual parameter λ is introduced as an additional independent variable and for fixed $t > 0$ one attempts to compute a point (m_h, λ), for which the Kuhn–Tucker conditions (5.9) and (5.10) hold:

$$\lambda^T c(m_h) \;=\; 0\ , \tag{5.37}$$

$$\text{grad}E(m_h) \;=\; A(m_h)\lambda\ . \tag{5.38}$$

Primal–dual methods show in general better performance than purely primal methods. If the columns of the matrix $A(m_h)$ are linearly independent for every $m_h \in \text{strict}(\mathcal{F}_h)$, the system (5.37), (5.38) is obviously equivalent to (5.34). But as we have seen at the end of Section 5.2, this condition on A is not fulfilled and the system (5.37), (5.38) is ill–conditioned. Thus we stay with the classical primal path method based on (5.34).

Nonetheless, (5.37) and (5.38) motivate the introduction of a Lagrangian function $L : RT_{0,h} \times \mathbb{R}^k \to \mathbb{R}$, defined as

$$L(m_h, \lambda) \;:=\; E(m_h) - \tfrac{1}{2}\lambda^T c(m_h)\ . \tag{5.39}$$

For each Lagrange multiplier vector $\lambda \in \mathbb{R}^k$ with $\lambda > 0$, the function

$$m_h \;\mapsto\; L(m_h, \lambda) \tag{5.40}$$

is convex and smooth on $RT_{0,h}$, and we have

$$L(m_h, \lambda) \;\to\; +\infty \quad \text{as} \quad ||m_h||_\infty \;\to\; +\infty\ .$$

Since

$$\nabla E(m_h) \;=\; A(m_h)\lambda$$

is the corresponding Euler–Lagrange equation to (5.40) and $m_h(t)$ is the unique solution to the equation (5.35), we have

$$L(m_h(t), \lambda(t)) \;\leq\; L(u_h, \lambda(t))$$

for all $u_h \in RT_{0,h}$ and all $t > 0$. In particular, if m_h^* denotes the unique analytic center of the optimality region defined in (5.24), then we have the estimate

$$L(m_h(t), \lambda(t)) \;\leq\; L(m_h^*, \lambda(t)) \;.$$

With the definition of the Lagrangian (5.39) this gives

$$\begin{aligned} 0 \;\leq\; E(m_h(t)) - E(m_h^*) \;&\leq \tfrac{1}{2}\lambda(t)^T c(m_h(t)) - \tfrac{1}{2}\lambda(t)^T c(m_h^*) \\ &\leq \tfrac{1}{2}\lambda(t)^T c(m_h(t)) \\ &\overset{(5.36)}{=} \tfrac{3}{2} t|\Omega| \;. \end{aligned} \tag{5.41}$$

Thus the absolute deviation of $E(m_h(t))$ from the minimum is bounded from above by $\frac{3}{2}t|\Omega|$. The factor $\frac{3}{2}$ is due to the choice (5.28) as set of barrier points.

An a–priori bound for the corresponding *relative* deviation is less easy to find. Nevertheless, our numerical experiments in Section 5.11 show, that the above bound is helpful in defining a suitable stopping criterion.

5.8 The Role of Newton's Method

From Lemma 5.3 we know that for each $t > 0$ the composite function E_t has a unique minimizer $m_h(t) \in \text{strict}(\mathcal{F}_h)$. Since the individual functions E and B are differentiable in the open set $\text{strict}(\mathcal{F}_h)$, the minimizer solves the Euler–Lagrange equation

$$\nabla E(m_h(t)) + t\,\nabla B(m_h(t)) \;=\; 0 \;. \tag{5.42}$$

We apply Newton's method to solve the nonlinear equation (5.42) approximately. It is well known that Newton's method exhibits asymptotically quadratic convergence and shows globally superlinear convergence in many practical problems if it is combined with a globalizing linesearch. In our interior point method the linesearch has to guarantee in particular the feasibility of the Newton iterates.

The starting point of our discussion is the genuine formulation of the *exact* Newton method. For fixed $t > 0$ we attempt to approach the unique minimizer of the composite function E_t by iterates

$$m_h^{(j+1)} \;=\; m_h^{(j)} + \alpha_j p_h^{(j)} \qquad j = 0, 1, 2, .. \;, \tag{5.43}$$

where $p_h^{(j)} \in RT_{0,h}$ denotes the Newton direction at $m_h^{(j)}$ and has the following representation in the basis $\{\varphi_h^{(i)}\}_{i=1,..,n}$ of $RT_{0,h}$:

$$p_h^{(j)} \;=\; \sum_{i=1}^{n} \gamma_i^{(j)} \varphi_h^{(i)}, \quad \gamma^{(j)} \in \mathbb{R}^n \;. \tag{5.44}$$

Here the coefficients $\gamma^{(j)}$ solve the large system of linear equations

$$\mathrm{Hess}E_t(m_h^{(j)})\gamma^{(j)} \;=\; -\nabla E_t(m_h^{(j)}) \;. \tag{5.45}$$

The scalars $0 < \alpha_j < 1$ define the step length such that $\{E_t(m_h^{(j)})\}_{j=0,1,2,..}$ becomes a monotonically decreasing sequence. A precise definition of α_j will be given in Section 5.10.

The choice $\alpha_j = 1$ in (5.43) leads to a *pure* Newton step. An iteration that is solely based on pure Newton steps is what we call a "classical" Newton method. It is known that the latter one exhibits quadratic convergence at least locally (in a neighborhood of the solution) if the Hessian is nonsingular. But in the context of a barrier method the pure Newton step may be infeasible, i. e. it may happen that $m_h^{(j+1)} \notin \mathrm{strict}(\mathcal{F}_h)$ and the interior point algorithm breaks down.

In [53] two basic reduction strategies for the barrier parameter are compared which lead to so–called "short–step" and "long–step" interior point algorithms. In short–step IPM only a single pure Newton step is performed for each t, which is then multiplied by a factor less than but very close to one. This careful reduction indeed ensures feasibility of the Newton step. Though short–step algorithms are preferable to prove theoretical complexity results for IPM, they are not reasonable in practical implementations, since the number of outer iterations becomes too large. Instead, we implement a long–step method. This allows for a factor of 0.1 in the reduction of the barrier parameter, although one has to perform several Newton steps for each unconstrained minimization problem, some of them involving a step length in (5.43) considerably less than one.

5.9 The Inexact Newton Step

Since $\mathrm{Hess}E_t(m_h)$ is a fully–populated matrix, direct methods in solving (5.45) are prohibitive due to the complexity consdiderations in Section 4.6. Instead, we apply an iterative method based on the $\mathcal{H}^2$–matrix compression for fast matrix–vector products: due to the factorization $\mathrm{Hess}E = W^T K W$ introduced in (3.34), the multiplication of $\mathrm{Hess}E_t(m_h)$ with a vector $\gamma \in \mathbb{R}^n$ involves three multiplications of a vector with a sparse matrix and one multiplication of a vector with an $\mathcal{H}^2$–matrix:

$$\mathrm{Hess}E_t(m_h)\gamma \;=\; W^T K W\gamma + t\;\mathrm{Hess}B(m_h)\gamma \;.$$

We also notice that entries of $\mathrm{Hess}B(m_h)$ may converge to $+\infty$ when m_h approaches the boundary of $\mathrm{strict}(\mathcal{F}_h)$, since then $|m_h(x_i)|^2$ is close to 1 in (5.15) for constraints c_i which are nearly active at m_h. Indeed it was shown by [43] that the Hessian of a composite function like E_t becomes increasingly ill–conditioned as t decreases to zero and is singular in the limit. This behavior is also revealed by our numerical experiments in Section 5.11.

We solve the linear subproblems (5.45) approximately by the conjugate gradient method and replace the exact Newton step in (5.43) by an inexact one, i. e. we look

for an approximate solution γ to (5.45) satisfying the condition

$$||\nabla E_t(m_h^{(j)}) + \mathrm{Hess}E_t(m_h^{(j)})\gamma^{(j)}||_2 \;\leq\; \eta_j||\nabla E_t(m_h^{(j)})||_2 \;, \tag{5.46}$$

where $||\cdot||_2$ denotes the euclidean norm in $\mathbb{R}^n$. Here the scalar parameters $0 < \eta_j < 1$, the so–called *forcing terms*, determine how accurately the Newton system (5.45) is to be solved.

The forcing terms η_j affect the efficiency of the inexact Newton method. On the one hand, the efficiency may suffer by demanding too much subproblem accuracy away from the minimizer $m_h(t)$, since this requires a relatively large number of matrix–vector multiplications in the conjugate gradient method. On the other hand, considerable accuracy may be appropriate in the vicinity of the minimizer $m_h(t)$ in order to realize the quadratic local convergence of the exact Newton method.

A number of options for the *forcing terms* η_j are proposed in the literature. We apply the choice suggested in [21], i. e. we set

$$\eta_j \;=\; \min\left\{\eta_{j-1}, \left(\frac{||\nabla E_t(m_h^{(j)})||_2}{||\nabla E_t(m_h^{(j-1)})||_2}\right)^2\right\} \tag{5.47}$$

with initial value $\eta_0 = 0.1$.

As a suitable initial guess $m_h^{(0)} \in \mathrm{strict}(\mathcal{F}_h)$ in (5.43) we take the approximate minimizer of $E_{t'}$ computed for some greater $t' > t$. Since we apply a long–step IPM, this might be a poor guess for the minimizer $m_h(t)$. In particular, this starting point may not lie in the range of quadratic convergence for Newton's method. Even worse, the matrix $\mathrm{Hess}E_t$ becomes increasingly ill–conditioned as $t \downarrow 0$, from which Newton's method may severely suffer [18, Chapter 2.3]. This behavior is also revealed by our numerical experiments in Section 5.11.

5.10 The Linesearch Procedure

Since we have to deal with fully–populated matrices in the evaluation of the composite function E_t, the linesearch in (5.43) should require as few matrix–vector products as possible. For fixed m_h and p_h we have

$$E_t(m_h + \alpha p_h) \;=\; d_2\alpha^2 + d_1\alpha + d_0 + tB(m_h + \alpha p_h) \;, \tag{5.48}$$

where

$$\begin{aligned}
d_2 &= \int_{\mathbb{R}^2}\int_{\mathbb{R}^2} \nabla\cdot p_h(x)\frac{1}{4\pi|x-y|}\nabla\cdot p_h(y)\; dy\; dx \quad , \\
d_1 &= 2\int_{\mathbb{R}^2}\int_{\mathbb{R}^2} \nabla\cdot m_h(x)\frac{1}{4\pi|x-y|}\nabla\cdot p_h(y)\; dy\; dx \;- 2\int_\Omega H_{ext}\cdot p_h\; dx \;, \\
d_0 &= E(m_h) \;.
\end{aligned}$$

Thus the function $\phi(\alpha) := E_t(m_h + \alpha p_h)$ consists of a quadratic term in α, where the coefficients have to be computed only once for given m_h and p_h, and the barrier term $B(m_h + \alpha p_h)$, which has to be evaluated for each given α. The computation of the coefficients d_0, d_1, and d_2, involves the two $\mathcal{H}^2$–matrix–vector products $K\nabla \cdot m_h$ and $K\nabla \cdot p_h$, whereas the the computation of the barrier term only involves the evaluation of k logarithms.

We apply an *Armijo* or *pure backtracking* linesearch, which is farely easy to implement: we generate trial steps $\alpha_j^{(0)}, \alpha_j^{(1)}, \alpha_j^{(2)}, ...$, where each trial step is taken as a fixed fraction τ of the previous one (we choose $\tau = 2$ and $\alpha_j^{(0)} = 1$ as initial step), and this process is terminated once the new iterate $m_h^{(j+1)}$ in (5.43) satisfies the monotonicity condition

$$E_t(m_h^{(j+1)}) < E_t(m_h^{(j)}) \ . \tag{5.49}$$

In particular, this guarantees the feasibility of the Newton step.

5.11 Implementation and Numerical Results

Now we present the formal algorithm for solving the Euler–Lagrange equation (5.42) with given $t > 0$. This is the variant of Newton's method described in detail in Sections 5.8, 5.9, and 5.10.

procedure Newton(m_h, t, tol_{Newton})
$\eta \leftarrow 0.1$;
while $||\nabla E_t(m_h)||_2 > tol_{Newton}$
  compute $\gamma \in \mathbb{R}^n$ such that
  $||\nabla E_t(m_h) + \mathrm{Hess} E_t(m_h)\gamma||_2 \leq \eta ||\nabla E_t(m_h)||_2$
    (by the conjugate gradient method, starting from $0 \in \mathbb{R}^n$) ;
  $\gamma \in \mathbb{R}^n$ defines $p_h \in RT_{0,h}$ by (5.44) ;
  $\alpha \leftarrow 1$;
  while $m_h + \alpha p_h$ is infeasible or $E_t(m_h + \alpha p_h) > E_t(m_h)$
    $\alpha \leftarrow 0.5\,\alpha$;
  end
  $\eta_{new} \leftarrow (||\nabla E_t(m_h + \alpha p_h)||_2 \ / \ ||\nabla E_t(m_h)||_2)^2$;
  if $\eta_{new} < \eta$
    $\eta \leftarrow \eta_{new}$;
  $m_h \leftarrow m_h + \alpha p_h$;
end
return m_h .

With the above subroutine for Newton's method, the formal algorithm for the IPM reduces to:

```
procedure IPM(m_h, t, iterates)
for i = 1 to iterates
    m_h ← Newton(m_h, t, 1.0e–3) ;
    t ← 0.1 t ;
end
return m_h .
```

Here we choose the strictly feasible initial value $m_h \equiv 0$. The barrier parameter is initialized by $t = 1$. The a–priori bound 5.41 suggests the choice $iterates = 4$.

We test our implementation of the barrier method on a $\mathcal{T}_h$–type triangulation of $\Omega = (0,1)^2$ that is refined towards the boundary as described in Section 4.5. In view of the numerical results in Section 4.9 we choose $h = 3.0\text{e–}1$. Since our computations now involve not only the charge density σ_h but also the magnetization m_h, we rely on a slight modification of the algorithm to generate $\mathcal{T}_h$ introduced in Section 4.5: we start from a uniform triangulation $\mathcal{Q}_\lambda$ of mesh size $\lambda = 2^{-5}$ and apply the refinement rule (4.107) with $h = 3.0\text{e–}1$ and $\alpha = 2/3$. This guarantees that the triangulation $\mathcal{T}_h$ becomes fine enough in the interior of Ω, and leads to a triangulation with $N = 1.3\text{e+}4$ triangles. The $\mathcal{H}^2$–matrix method takes 43 seconds for the setup phase and allows for a compression rate of 9.8e–3. (Reference values can be found in Section 4.8.5.)

We do not have a rigorous numerical analysis at hand as in [11] to judge the quality of our finite element solution m_h^* in terms of a–priori (and a–posteriori) error estimates. However, the results on the Dirichlet screen problem in Section 4.4 combined with the stability result in Lemma 5.8 allow for a reliable consistency check: for the external fields $H_{ext} = (0.2, 0.2)$ and $H_{ext} = (0.3, 0.1)$ the barrier is not active. We compare the tight approximation of the energy $E(\sigma^*)$ in the Dirichlet screen problem (as introduced at the beginning of Section 4.9 and illustrated in Figure 4.13) with the corresponding value for $E(m_h(t))$, $t = 1.0\text{e–}3$, computed by our IPM implementation above. This consistency check allows us to consider $m_h(1.0\text{e–}3)$ as a suitable approximation to the analytic center m_h^*: Table 5.1 shows that the relative error

$$\epsilon \;=\; \sqrt{\frac{E(m_h(1.0\text{e–}3)) - E(\sigma^*)}{-E(\sigma^*)}} \;,$$

introduced in Section 4.9, is of the order 5%.

We continue our numerical experiments by considering external fields H_{ext} applied along the diagonal of the square $\Omega = (0,1)^2$. The external fields are of the form

$$H_{ext} \;=\; \tfrac{1}{\sqrt{2}}\,|H_{ext}|\,(1.0, 1.0) \;.$$

In Table 5.2 we document for each field strength $|H_{ext}|$ the energy $E(m_h(1.0\text{e–}3))$, the supremum $||m_h(1.0\text{e–}3)||_\infty$, the CPU time measured in seconds, and the total

H_{ext}	(0.2,0.2)	(0.3,0.1)
$E(\sigma^*)$	-8.32368e–2	-1.03991e–1
$E(m_h(1.0e{-}3))$	-8.31364e–2	-1.03739e–1
ϵ	3.47e–2	4.92e–2

Table 5.1: A consistency check with the results on the Dirichlet screen problem promotes $m_h(1.0e{-}3)$ as a suitable approximation to m_h^*. The relative error with respect to energy does not exceed 5%.

number of $\mathcal{H}^2$–matrix–vector products required. Figures 5.2 up to 5.6 illustrate these results with additional comments. All numerical experiments were done on a Pentium III processor running at 700 MHz.

To break down the data of Table 5.2 into more details, we also document the results for each single barrier step in Tables 5.4 and 5.5.

$\lvert H_{ext}\rvert$	CPU (s)	$\mathcal{H}^2$–products	$E(m_h(1.0e{-}3))$	$\lvert\lvert m_h(1.0e{-}3)\rvert\rvert_\infty$
1.4e–1	3.6e+2	6.4e+2	–2.07841e–2	1.82e–1
2.8e–1	3.5e+2	6.3e+2	–8.31364e–2	3.58e–1
4.2e–1	7.1e+2	1.2e+3	–1.87057e–1	5.22e–1
5.7e–1	8.6e+2	1.5e+3	–3.32544e–1	6.81e–1
7.1e–1	1.2e+3	2.1e+3	–5.19592e–1	8.40e–1
8.5e–1	2.3e+3	3.9e+3	–7.47736e–1	9.84e–1
9.9e–1	3.5e+3	6.0e+3	–9.98965e–1	9.93e–1
1.1e+0	1.1e+4	1.9e+4	–1.25627e+0	9.96e–1
1.3e+0	8.4e+3	1.5e+4	–1.51641e+0	9.98e–1
1.4e+0	9.9e+3	1.7e+4	–1.77837e+0	9.99e–1

Table 5.2: An overview of the most important IPM data in our numerical experiments with external fields H_{ext} applied along the diagonal of the square $\Omega = (0,1)^2$.

$\|H_{ext}\|$	CPU (s)	$\mathcal{H}^2$–products	$E(m_h(1.0\text{e}{-3}))$	$\|\|m_h(1.0\text{e}{-3})\|\|_\infty$
0.1	2.8e+3	1.2e+3	–5.32876e–2	2.13e–1
0.2	3.9e+3	1.5e+3	–2.13150e–1	4.17e–1
0.3	4.4e+3	1.7e+3	–4.79585e–1	6.17e–1
0.4	9.5e+3	3.7e+3	–8.52577e–1	8.11e–1
0.5	1.2e+4	4.6e+3	–1.33143e+0	9.81e–1
0.6	9.7e+3	3.9e+3	–1.88052e+0	9.98e–1
0.7	2.4e+4	1.0e+4	–2.45032e+0	9.99e–1
0.8	3.0e+4	1.2e+4	–3.03101e+0	9.99e–1
0.9	4.3e+4	1.7e+4	–3.61867e+0	9.99e–1
1.0	5.0e+4	2.0e+4	–4.21120e+0	9.99e–1

Table 5.3: An overview of the most important IPM data in our numerical experiments with external fields H_{ext} applied along the horizontal axis on a circular domain Ω, as depicted in Figures 5.7 and 5.8.

To test our IPM implementation for more general geometries, we consider a convex polygon Ω with boundary $\partial\Omega$ that approximates pointwise the circle $\partial B_1(0) \subset \mathbb{R}^2$. We used the MATLAB PDE Toolbox to generate the triangulation shown in Figure 5.7. Then we apply the refinement rule (4.107) with $h = 3.0\text{e}{-1}$ and $\alpha = 2/3$, which leads to the triangulation illustrated in Figure 5.8. On this geometry we apply our IPM implementation with external fields H_{ext} in direction $(1.0, 0.0)$. The numerical results are presented in Table 5.3 and Figures 5.9 up to 5.13.

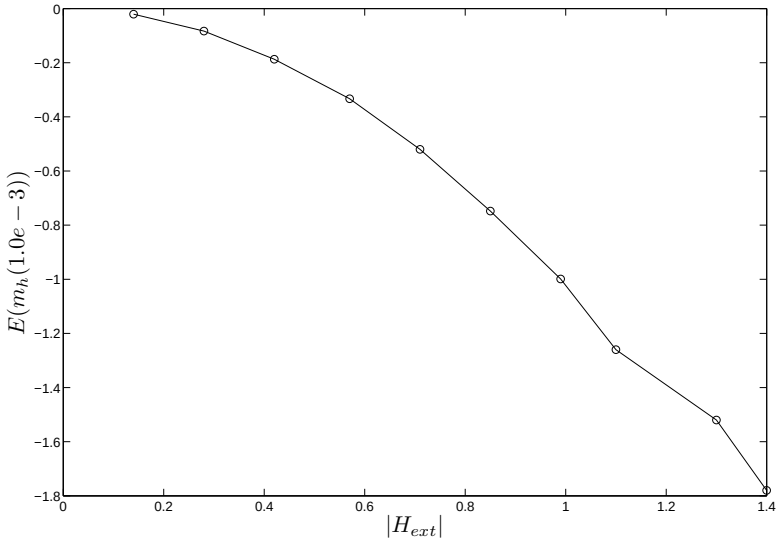

Figure 5.2: We plot the energy of m_h(1.0e–3) against $|H_{ext}|$ as the horizontal scale. The domain is $\Omega = (0,1)^2$. The case $H_{ext} = 0$ is trivial since the analytic center is given by $m_h^* \equiv 0$ for zero external field.

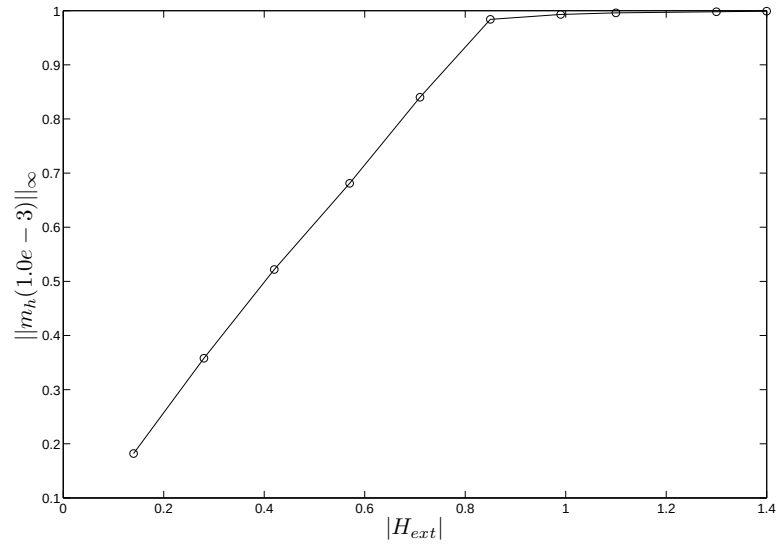

Figure 5.3: We plot $||m_h(1.0e{-}3)||_\infty$ against $|H_{ext}|$ as the horizontal scale. The domain is $\Omega = (0,1)^2$. This illustrates some important feature of the analytic center m_h^* (as approximated by m_h(1.0e–3)): if $|H_{ext}|$ is sufficiently small, the barrier is not active and $||m_h^*||_\infty < 1$ according to Lemma 5.8. This behavior is also evident from the 3–d plots in Figures 5.5 and 5.6.

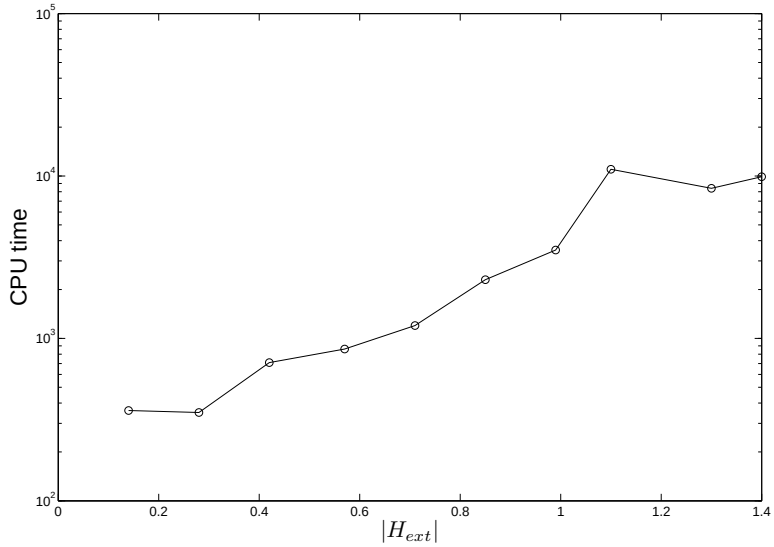

Figure 5.4: We plot the CPU time (in seconds, and displayed logarithmically) against $|H_{ext}|$ as the horizontal scale. The domain is $\Omega = (0,1)^2$. This reveals the ill–conditioning of our IPM implementation at field strengths where the barrier becomes active.

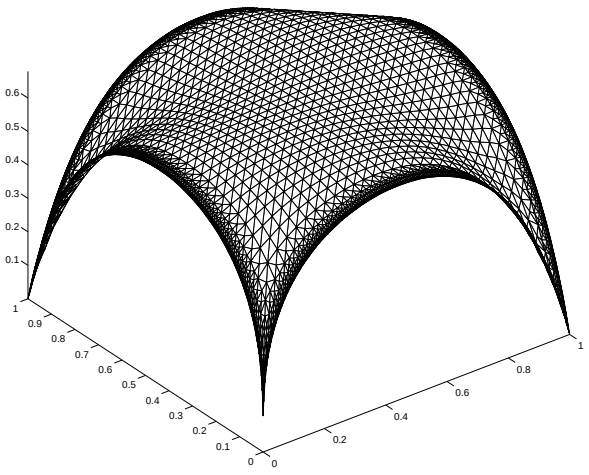

Figure 5.5: A MATLAB PDE Toolbox plot of $|m_h(1.0\text{e}{-3})|$ on $\mathcal{T}_h$ for external field $H_{ext} = (0.4, 0.4)$, i. e. we have $|H_{ext}| = 5.7\text{e}{-1}$. The domain of consideration is $\Omega = (0,1)^2$, the barrier is not active.

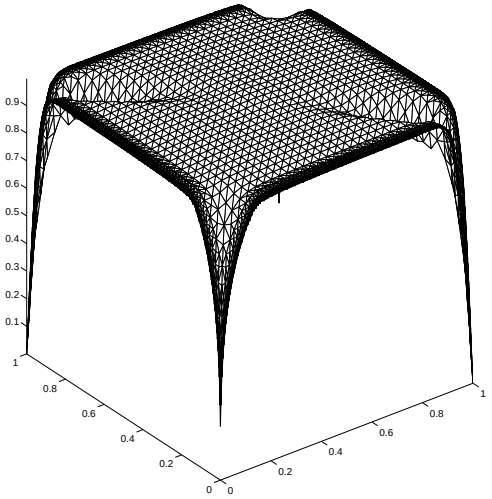

Figure 5.6: A MATLAB PDE Toolbox plot of $|m_h(1.0\text{e}{-3})|$ on $\mathcal{T}_h$ for external field $H_{ext} = (1.0, 1.0)$, i. e. we have $|H_{ext}| = 1.4\text{e}{+0}$. The domain of consideration is $\Omega = (0,1)^2$, the barrier is active.

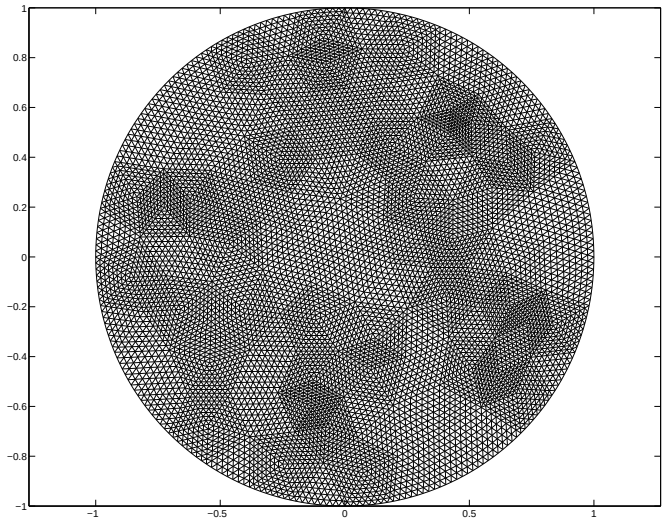

Figure 5.7: A triangulated polygon approximating a circular domain, generated by the PDE Toolbox of MATLAB. The number of triangles is 1.6e+4, each triangle is of diameter strictly less than 2^{-5}, the maximal diameter occuring in the triangulation of the square domain in the numerical experiments above.

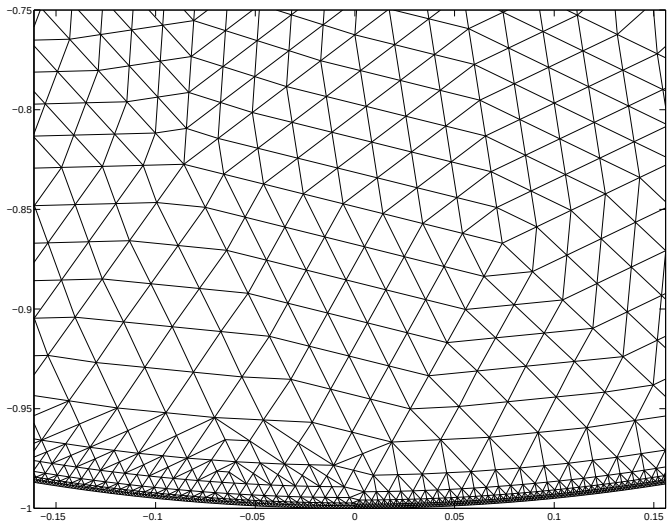

Figure 5.8: Applying the refinement rule (4.107) with $h = 3.0\text{e}{-1}$ and $\alpha = 2/3$ on the circular triangulation in Figure 5.7, leads to a mesh refined towards the boundary as illustrated here. The number of triangles becomes 3.9e+4, the setup phase for the $\mathcal{H}^2$–matrix method takes 135 seconds and the compression rate is 1.0e–2.

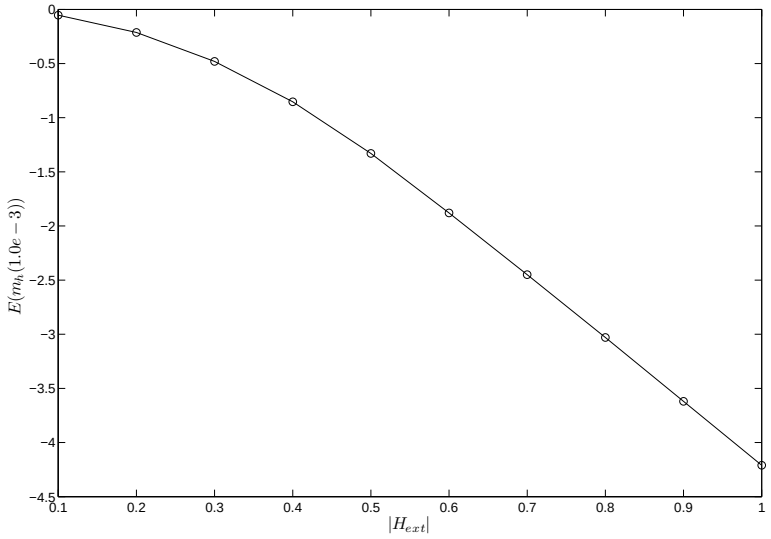

Figure 5.9: Results on the circular domain Ω. We plot the energy of $m_h(1.0\text{e}{-3})$ against $|H_{ext}|$ as the horizontal scale. The case $H_{ext} = 0$ is trivial since the analytic center is given by $m_h^* \equiv 0$ for zero external field.

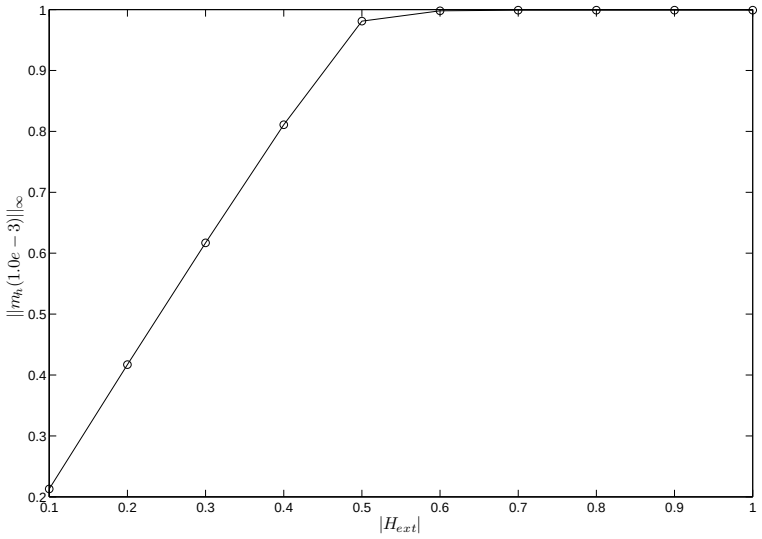

Figure 5.10: Results on the circular domain Ω. We plot $||m_h(1.0\text{e}{-}3)||_\infty$ against $|H_{ext}|$ as the horizontal scale. This illustrates some important feature of the analytic center m_h^* (as approximated by $m_h(1.0\text{e}{-}3)$): if $|H_{ext}|$ is sufficiently small, the barrier is not active and $||m_h^*||_\infty < 1$ according to Lemma 5.8. This behavior is also evident from the 3–d plots in Figures 5.12 and 5.13.

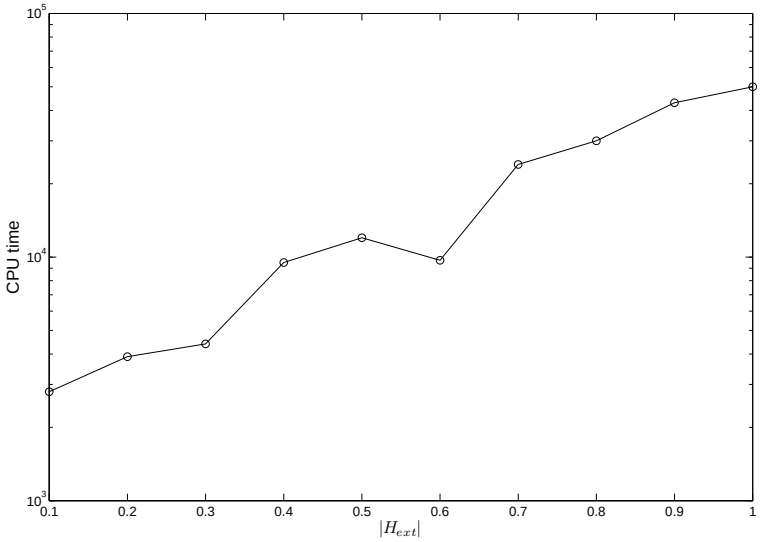

Figure 5.11: Results on the circular domain Ω. We plot the CPU time (in seconds, and displayed logarithmically) against $|H_{ext}|$ as the horizontal scale. This reveals the ill–conditioning of our IPM implementation at field strengths where the barrier becomes active.

t	$E(m_h(t))$	CPU (s)	$\mathcal{H}^2$–products	# Newton
1.0e+0	–1.24913e–2	7.1e+1	125	2
1.0e–1	–2.03146e–2	1.2e+2	207	2
1.0e–2	–2.07778e–2	1.6e+2	275	2
1.0e–3	–2.07841e–2	1.8e+1	33	1
1.0e+0	–4.97225e–2	6.9e+1	125	2
1.0e–1	–8.10740e–2	1.1e+2	194	2
1.0e–2	–8.31068e–2	1.5e+2	273	2
1.0e–3	–8.31364e–2	1.9e+1	33	1
1.0e+0	–1.10986e–1	6.8e+1	123	2
1.0e–1	–1.81568e–1	3.1e+2	547	3
1.0e–2	–1.86968e–1	1.8e+2	300	2
1.0e–3	–1.87057e–1	1.5e+2	256	2
1.0e+0	–1.95144e–1	1.6e+2	290	3
1.0e–1	–3.20296e–1	2.4e+2	421	3
1.0e–2	–3.32293e–1	2.1e+2	367	2
1.0e–3	–3.32544e–1	2.5e+2	434	2
1.0e+0	–3.00756e–1	1.5e+2	274	3
1.0e–1	–4.94171e–1	2.5e+2	428	3
1.0e–2	–5.18717e–1	5.2e+2	886	3
1.0e–3	–5.19592e–1	2.8e+2	469	2

Table 5.4: A detailed protocol of the barrier steps $t = 1.0, 1.0\text{e–}1, 1.0\text{e–}2, 1.0\text{e–}3$, related to Table 5.2. The blocks of data presented here correspond to the upper five rows in Table 5.2; the remaining blocks follow in Table 5.5. The block on the top of this page gives therefore the detailed data for $H_{ext} = (0.1, 0.1)$, whereas the bottom one presents that for $H_{ext} = (0.5, 0.5)$. In particular, we document the number of Newton steps in the last column. Our experiments show that, as long as the barrier is not active, the number of Newton steps remains almost constant with decreasing t.

6 Minimizers of Unit Length

We suppress all primes for the two–dimensional variables in the following, since our considerations are restricted to the cross–section of the thin film.

6.1 Hamilton–Jacobi Equations and Viscosity Solutions

In the preceeding sections we have considered solutions m_h^* to the minimization problem (3.26) that are uniquely characterized as the analytic center of the optimality region. In the following, we aim at a different type of minimizer: a solution m_h that is of unit length.

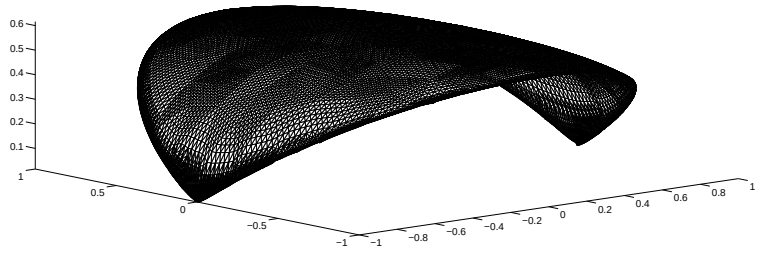

Figure 5.12: A MATLAB PDE Toolbox plot of $|m_h(1.0\text{e}{-3})|$ on the circular domain Ω for external field $H_{ext} = (0.3, 0.0)$. The barrier is not active.

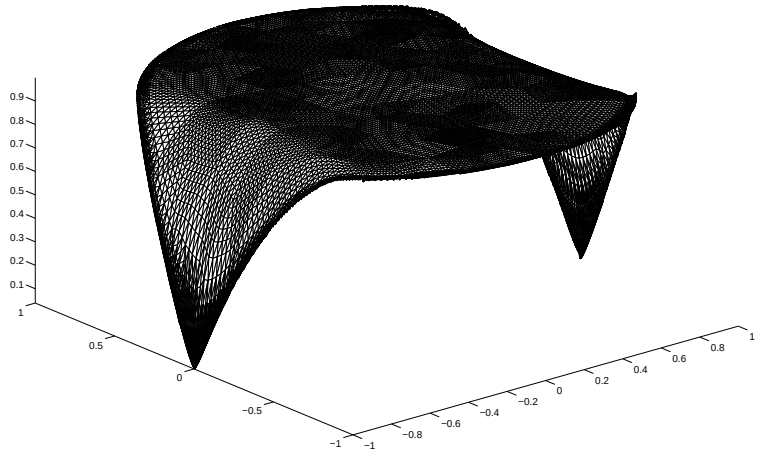

Figure 5.13: A MATLAB PDE Toolbox plot of $|m_h(1.0\text{e}{-3})|$ on the circular domain Ω for external field $H_{ext} = (1.0, 0.0)$. The barrier is active.

t	$E(m_h(t))$	CPU (s)	$\mathcal{H}^2$–products	# Newton
1.0e+0	–4.26126e–1	1.4e+2	246	3
1.0e–1	–6.97885e–1	3.0e+2	520	4
1.0e–2	–7.43504e–1	7.7e+2	1344	5
1.0e–3	–7.47736e–1	1.1e+3	1827	6
1.0e+0	–5.69434e–1	1.2e+2	217	3
1.0e–1	–9.24132e–1	3.4e+2	588	5
1.0e–2	–9.92370e–1	6.2e+2	1066	5
1.0e–3	–9.98965e–1	2.4e+3	4129	11
1.0e+0	–7.28840e–1	1.1e+2	183	3
1.0e–1	–1.16544e+0	3.9e+2	683	5
1.0e–2	–1.24904e+0	8.9e+2	1523	7
1.0e–3	–1.25627e+0	9.8e+3	17033	15
1.0e+0	–9.02426e–1	1.7e+2	290	4
1.0e–1	–1.41612e+0	4.2e+2	721	5
1.0e–2	–1.50902e+0	1.1e+3	1877	9
1.0e–3	–1.51641e+0	6.7e+3	11964	15
1.0e+0	–1.08857e+0	1.4e+2	233	4
1.0e–1	–1.67266e+0	3.1e+2	527	4
1.0e–2	–1.77101e+0	1.1e+3	1957	9
1.0e–3	–1.77837e+0	8.3e+3	14357	16

Table 5.5: Continuation of Table 5.4; these blocks correspond to the last five rows in Table 5.2. For the external fields $H_{ext} = (0.6, 0.6)$ up to $H_{ext} = (1.0, 1.0)$ the barrier becomes active, thus the number of Newton steps increases distinctly as t tends to zero.

We have already observed that the reduced micromagnetic energy E of problem 3.5 is degenerate in the sense that minimizers are not unique. Only the charge density $\sigma = \nabla \cdot m$ and the stray field $-\nabla u$ are uniquely determined. If we consider e. g. the case of vanishing external field $H_{ext} = 0$ and circular domain $\Omega = \{x \in \mathbb{R}^2 \mid |x| \leq 1\}$, there are at least two admissible minimizers, namely the trivial magnetization $m = 0$ and the vortex field $m(x) = (-x_2, x_1)/|x|$. But even if we reimpose the nonconvex constraint $|m| = 1$, uniqueness is not guaranteed as we shall see in the following.

Having identified a minimizer m^* of the convex variational problem (3.5) with length $|m^*| \leq 1$, we may construct a solution m of unit length in the domain Ω by considering the following boundary value problem:

$$|\nabla \psi(x) - (m^*)^\perp(x)|^2 \;=\; 1 \quad \text{for } x \in \Omega, \quad \psi(x) \;=\; 0 \quad \text{for } x \in \partial\Omega \,. \tag{6.1}$$

Here the rotated magnetization $(m^*)^\perp$ is defined as $(m^*)^\perp = (-m_2^*, m_1^*)$. Corre-

spondingly, we set $\nabla^\perp\psi = (-\partial\psi/\partial x_2, \partial\psi/\partial x_1)$. Then

$$m \;:=\; \nabla^\perp\psi + m^* \tag{6.2}$$

yields an admissible minimizer of E with $|m| = 1$, since we have $\nabla\cdot\nabla^\perp\psi = 0$ and therefore $E(m) = E(m^*)$. The zero boundary condition ensures that $\nabla^\perp\psi(x)\cdot\nu(x) = 1$ holds for all $x \in \partial\Omega$, and so the normal component of m vanishes at $\partial\Omega$.

We notice that (6.1) states a boundary value problem for a Hamilton–Jacobi equation with Hamiltonian

$$H(x,p) \;=\; |\,p - (m^*)^\perp(x)\,|^2 - 1\;. \tag{6.3}$$

For topological reasons there exists no classical solution to (6.1) that is everywhere smooth in Ω. Moreover, (6.1) allows for infinitely many weak solutions, and so we have to single out a weak solution of practical relevance. We will consider the *viscosity solution* to (6.1), which is introduced in Definition 6.1. The choice of the viscosity solution appears to single out a minimizer with as few walls as possible. Moreover, it is the same as the one proposed in [10].

The notion of viscosity solution was first introduced in [14] for scalar nonlinear first order partial differential equations. Viscosity solutions are continuous but need not be differentiable anywhere. They represent a class of suitable generalized solutions if crossing characteristics occur. The concept of viscosity solutions allows to derive several uniqueness and existence results.

We recall the basic definitions and results referred to in the succeeding sections. The considerate reader will observe that the results outlined hold for continuous Hamiltonians, whereas the function H in (6.3) may exhibit discontinuities in the space variable x. However, the notion of viscosity solutions serves as a *motivation* for the numerical schemes introduced later, although we are not able to establish convergence results for these schemes.

Definition 6.1. *Let $H : \Omega \times \mathbb{R}^2 \to \mathbb{R}$ be a continuous function. A function $\psi \in C^{0,1}(\overline{\Omega})$ is a* viscosity subsolution *of the first order equation*

$$H(x, \nabla\psi(x)) \;=\; 0\;, \qquad x \in \Omega \tag{6.4}$$

if for all test functions $\phi \in C_0^\infty(\Omega)$ the following condition holds: if $\psi - \phi$ attains a local maximum at $x_0 \in \Omega$, then

$$H(x_0, \nabla\psi(x_0)) \;\le\; 0\;. \tag{6.5}$$

A function $\psi \in C^{0,1}(\overline{\Omega})$ is a viscosity supersolution *of (6.4) if for all test functions $\phi \in C_0^\infty(\Omega)$ the following condition holds: if $\psi - \phi$ attains a local minimum at $x_0 \in \Omega$, then*

$$H(x_0, \nabla\psi(x_0)) \;\ge\; 0\;. \tag{6.6}$$

If ψ is simultaneously a viscosity sub– and supersolution, then it is called a viscosity solution *of (6.4).*

The notions of viscosity and classical solutions are consistent in the following sense [13]:

Theorem 6.1. *If $\psi \in C^1(\overline{\Omega})$ is a classical solution to (6.4), i. e.*

$$H(x, \nabla\psi(x)) \;=\; 0 \qquad \forall x \in \Omega \;,$$

then ψ is a viscosity solution.

In particular, any classical solution to (6.4) satisfies the inequalities (6.5) and (6.6). For topological reasons the minimizer m defined by (6.2) can not be of class $C^1(\overline{\Omega})$ since the normal component of m vanishes at the boundary of Ω. Due to [13] we have the following partial result:

Theorem 6.2. *If $\psi \in C^{0,1}(\overline{\Omega})$ is a viscosity solution of (6.4) which is differentiable at some $x_0 \in \Omega$, then we have*

$$H(x_0, \nabla\psi(x_0)) \;=\; 0 \;.$$

Thus in regions of Ω where the viscosity solution ψ is smooth, it coincides with a classical solution. The existence of viscosity solutions is guaranteed under suitable conditions [39, Theorem 5.3]:

Theorem 6.3. *Let the Hamiltonian $H : \overline{\Omega} \times \mathbb{R}^2 \to \mathbb{R}$ satisfy the following assumptions:*

1. *$H \in C^0(\overline{\Omega} \times \mathbb{R}^2)$;*
2. *$p \mapsto H(x,p)$ is convex in p for all $x \in \overline{\Omega}$;*
3. *H is coercive in p, i. e. $H(x,p) \to \infty$ as $|p| \to \infty$ uniformly in $x \in \overline{\Omega}$;*
4. *the Hamiltonian is compatible in the sense that $H(x,0) \leq 0$ for all $x \in \overline{\Omega}$.*

Then the Dirichlet problem

$$\begin{aligned} H(x, \nabla\psi(x)) \;&=\; 0 \qquad && \text{for } x \in \Omega \;, \\ \psi(x) \;&=\; \phi(x) \qquad && \text{for } x \in \partial\Omega \;, \end{aligned}$$

has a viscosity solution if and only if the boundary values ϕ satisfy the compatibility condition

$$\phi(x) - \phi(y) \;\leq\; \delta(x,y) \qquad \text{for all } x, y \in \partial\Omega \;. \tag{6.7}$$

Here δ denotes the optical distance given by

$$\delta(x,y) \;=\; \inf\left\{ \int_0^1 \rho(\xi(t), -\xi'(t))dt \mid \xi \in C^{0,1}([0,1], \overline{\Omega}), \xi(0) = x, \xi(1) = y \right\} \;, \tag{6.8}$$

where $\rho(x,q) := \max_{H(x,p)=0} p \cdot q$. Provided ϕ fulfills (6.7), a specific viscosity solution can be represented by the Hopf–Lax formula

$$\psi(x) \;=\; \inf_{y \in \partial\Omega} \left(\phi(y) + \delta(x,y)\right) \;. \tag{6.9}$$

To establish a uniqueness result, we need a slightly stronger compatibility condition on the Hamiltonian which allows for the following comparison principle [38].

Theorem 6.4. *Let H fulfill the assumptions of Theorem 6.3 together with the strict inequality*

$$H(x,0) \;<\; 0 \qquad \text{for all } x \in \Omega \;.$$

Let further $u, v \in C^{0,1}(\overline{\Omega})$ be viscosity sub– and supersolutions of (6.4), respectively. Then the following comparison principle holds: If $u \leq v$ on $\partial\Omega$ then $u \leq v$ on $\overline{\Omega}$.

The uniqueness of the viscosity solution (6.9) is now a direct consequence of the previous theorem.

6.2 Discretization

We recall the discrete de Rham complex (3.21) introduced in Section 3.7, namely

$$0 \;\xrightarrow{\subset}\; P^1_{0,h} \;\xrightarrow{\nabla^\perp}\; RT_{0,h} \;\xrightarrow{\nabla\cdot}\; P^0_{0,h} \;\longrightarrow\; 0 \;. \tag{6.10}$$

The corresponding discrete version of problem (6.1) may now be stated as follows:

$$\begin{gathered}\text{Given } m_h^* \in RT_{0,h}, \text{ find } \psi_h \in P^1_{0,h} \text{ such that the field} \\ \nabla^\perp \psi_h + m_h^* \;\in\; RT_{0,h} \\ \text{is approximately of unit length.}\end{gathered} \tag{6.11}$$

This ansatz leaves the reduced micromagnetic energy unchanged, i. e. we have

$$E(m_h^*) \;=\; E(\nabla^\perp \psi_h + m_h^*) \;. \tag{6.12}$$

We can not expect that the new minimizer $\nabla^\perp \psi_h + m_h^*$ is of unit length everywhere, since $\nabla^\perp \psi_h$ is a piecewise constant field whereas m_h^* is in general not. Moreover, we observe that the corresponding Hamiltonian

$$H(x,p) \;=\; |\, p - (m_h^*)^\perp(x) \,|^2 - 1$$

is discontinuous in the space variable x for generic $m_h^* \in RT_{0,h}$. Therefore the results on viscosity solutions outlined in the preceeding section are not directly applicable to our setting. However, they serve as a promising *motivation* for numerical schemes which compute minimizers close to unit length with as few walls as possible.

The interest in numerical techniques for solving time–dependent as well as stationary Hamilton–Jacobi equations is promoted by the success of *level set methods* and *fast marching methods* in various areas of application, including geometry, fluid mechanics, combustion, seismology, and computer vision; see [50] for an introduction. The most fundamental objection to these numerical methods in our setting is the accuracy of the schemes: since the viscosity solution is continuous but not differentiable everywhere, robuste schemes guarantee only first order accuracy on all of Ω.

This conflicts with definition (6.2) that involves the gradient of the viscosity solution. However, the actual accuracy observed in practice increases in those regions of Ω where the viscosity solution is smooth; we refer to [50, Chapter 8.8.1] for a detailed discussion.

In case of problem (6.11) the transition to an alternative triangulation turns out to be beneficial: let $\mathcal{T}_\lambda$ be a regular triangulation of Ω with typical mesh size $\lambda > 0$. We do not presume that $\mathcal{T}_\lambda$ results from $\mathcal{T}_h$ by any kind of mesh generating procedure. In particular, m_h^* may not be interpretable as a finite element function on the triangulation $\mathcal{T}_\lambda$. Let $P^1_{0,\lambda}$ denote the space of continuous, piecewise affine functions on $\mathcal{T}_\lambda$ with zero boundary values on $\partial\Omega$. We consider the following variant of problem (6.11):

$$\begin{gathered} \text{Given } m_h^* \in RT_{0,h}, \text{ find } \psi_\lambda \in P^1_{0,\lambda} \text{ such that the field} \\ \nabla^\perp \psi_\lambda + \Pi^t_\lambda m_h^* \ \in \ (P^0_\lambda)^2 \\ \text{is approximately of unit length.} \end{gathered} \tag{6.13}$$

Here $\Pi^t_\lambda : (L^2)^2 \to (P^0_\lambda)^2$ denotes the interpolation operator onto the space of piecewise constant fields on $\mathcal{T}_\lambda$. For $m_h^* \in RT_{0,h}$ and triangles $T \in \mathcal{T}_\lambda$ with barycenter x_T it is given by

$$\Pi^t_\lambda m_h^*|_T \ = \ m_h^*(x_T) \ .$$

We stress that the field (6.13) is generally not even an admissible magnetization for the reduced model (3.5). However, since ψ_λ is continuous on Ω, we may project this function on the original finite element space $P^1_{0,h}$ by setting

$$\psi_h \ := \ \Pi^v_h \psi_\lambda \ , \tag{6.14}$$

where Π^v_h denotes the standard interpolation operator introduced in Section 3.5. The function ψ_h turns out to be a suitable solution to problem (6.11).

In the particular case of rectangular domains Ω we replace the alternative triangulation $\mathcal{T}_\lambda$ by a Cartesian grid, since numerical schemes based on finite difference approximations are easy to implement and show high degrees of accuracy in practice. For fixed mesh size $\lambda > 0$ the Cartesian grid consists of a set of nodal points

$$x_{ij} \ = \ (i\lambda, j\lambda) \ \in \ \Omega \ . \tag{6.15}$$

We reinterpret the data m_h^* on this grid by evaluation at x_{ij} and construct an approximate viscosity solution Ψ given by its values Ψ_{ij} at the nodal points. The Cartesian grid is then interpreted as a triangulation of type $\mathcal{Q}_\lambda$ (see Section 3.4 for the precise definition) with mesh size $\lambda > 0$ and corresponding solution $\psi_\lambda \in P^1_{0,\lambda}$, which is projected thereafter as in (6.14).

The concept for approximating minimizers of unit length introduced so far may be generalized even further: we let $\mathcal{T}_\nu$ denote a triangulation of typical mesh size $0 < \nu < h$ that results from a refinement of the triangulation $\mathcal{T}_h$. In particular, we have

$$P^1_{0,h} \subset P^1_{0,\nu} \quad \text{ and } \quad RT_{0,h} \subset RT_{0,\nu}$$

for the corresponding finite element spaces. Applying the standard interpolation operator of $RT_{0,\nu}$ on the magnetization m_h^* yields the identity

$$m_h^* \;=\; \Pi_\nu^e m_h^* \;. \tag{6.16}$$

(We refer to Section 3.6.3 for the precise definition of the interpolation operator on Raviart–Thomas spaces.) We stress that m_h^* is in general *not* a minimizer on $RT_{0,\nu}$. Next we consider any solution ψ_λ to (6.13). We replace the projection (6.14) by

$$\psi_\nu \;:=\; \Pi_\nu^v \psi_\lambda \;,$$

and introduce the new magnetization $m_\nu \in RT_{0,\nu}$ by setting

$$m_\nu \;:=\; \nabla^\perp \psi_\nu + \Pi_\nu^e m_h^* \;. \tag{6.17}$$

Here $\nabla^\perp \psi_\nu$ defines a divergence–free field of class $RT_{0,\nu}$, i. e. we have

$$\nabla \cdot \nabla^\perp \psi_\nu \;=\; 0 \;. \tag{6.18}$$

Again, m_ν is in general not a minimizer of the finite element space $RT_{0,\nu}$, but it has the same energy as m_h^*:

$$\begin{aligned} E(m_\nu) \quad &= \quad E(\nabla^\perp \psi_\nu + \Pi_\nu^e m_h^*) \\ &\overset{(6.18)}{=} \quad E(\Pi_\nu^e m_h^*) \\ &\overset{(6.16)}{=} \quad E(m_h^*) \;. \end{aligned}$$

To recapitulate the various triangulations introduced in this section, we summarize:

- $\mathcal{T}_h$ denotes the triangulation on which the analytic center m_h^* is defined;
- $\mathcal{T}_\lambda$ is introduced for the computation of the piecewise continuous function ψ_λ in (6.13);
- $\mathcal{T}_\nu$ is an optional triangulation that allows for a magnetization m_ν with the same energy as m_h^* but defined on a finer grid.

6.3 Implementation and Results on Cartesian Grids

We start with the concept for approximating minimizers of unit length on Cartesian grids, such as (6.15) in the preceeding section.

We apply the scheme presented in [48] for solving numerically the shape–from–shading problem. This ansatz is also recommended as the method of choice for computing viscosity solutions on Cartesian grids in [50, Chapter 8].

We assume that Ω is a rectangular domain of $\mathbb{R}^2$. For simplicity we consider the case $\Omega = (0,1)^2$. For given mesh size $\lambda = 1/N$, with $N \in \mathbb{N}$, we introduce the nodal

points $x_{ij} = (i\lambda, j\lambda)$, $i, j = 0, .., N$. The value of our numerical approximation Ψ at x_{ij} is denoted by Ψ_{ij}.

We notice that for any given point $x \in \Omega$ the identity (6.1), i. e.

$$|\nabla\psi(x) - m^{\perp}(x)|^2 \;=\; 1 \;,$$

holds if and only if

$$\max_{q\in S^1}(\nabla\psi(x)\cdot q - m^{\perp}(x)\cdot q) \;=\; 1 \;. \tag{6.19}$$

The ansatz of [48] is to establish an *implicit* first–order finite difference scheme to approximate (6.19), which is then used to propose an *explicit* scheme that can be implemented efficiently. To do so, we define the following difference quotients: for $x_{ij} \in \Omega$ we set

$$\begin{aligned} D_1^+\Psi_{ij} &= \tfrac{1}{\lambda}(\Psi_{i+1\,j} - \Psi_{ij}) \;, \\ D_2^+\Psi_{ij} &= \tfrac{1}{\lambda}(\Psi_{i\,j+1} - \Psi_{ij}) \;, \\ D_1^-\Psi_{ij} &= \tfrac{1}{\lambda}(\Psi_{ij} - \Psi_{i-1\,j}) \;, \\ D_2^-\Psi_{ij} &= \tfrac{1}{\lambda}(\Psi_{ij} - \Psi_{i\,j-1}) \;. \end{aligned}$$

We evaluate m_h^* at the nodal points x_{ij} by setting

$$\begin{pmatrix} u_{ij} \\ v_{ij} \end{pmatrix} \;=\; (m_h^*)^{\perp}(x_{ij}) \;.$$

Next, we introduce a function $g_{ij} : \mathbb{R}^4 \to \mathbb{R}$ for every grid point $x_{ij} \in \Omega$ and all $a, b, c, d \in \mathbb{R}$ by

$$g_{ij}(a,b,c,d) \;=\; \max((a-u_{ij})^+, (b-u_{ij})^-)^2 + \max((c-v_{ij})^+, (d-v_{ij})^-)^2 - 1 \;,$$

where, as usual, $\xi^+ = \max(\xi, 0)$ and $\xi^- = \min(\xi, 0)$ for any $\xi \in \mathbb{R}$. With these notations, an implicit approximation scheme for (6.19) is given by

$$\begin{cases} g_{ij}(D_1^-\Psi_{ij}, D_1^+\Psi_{ij}, D_2^-\Psi_{ij}, D_2^+\Psi_{ij}) \;=\; 0 & \text{for } x_{ij} \in \Omega \;, \\ \Psi_{ij} \;=\; 0 & \text{for } x_{ij} \in \partial\Omega \;. \end{cases} \tag{6.20}$$

Based on the implicit scheme (6.20), we now turn over to an *explicit* algorithm that computes the approximate solution Ψ.

The proposed explicit scheme is defined by a Gauss–Seidel iteration; we do not attempt to advance it to a fast marching method as in [50, Chapter 8], since the computation of the analytic center m_h^* dominates our numerics with respect to CPU time. To specify the stopping criterion we introduce the mean value,

$$\bar{g} \;:=\; N^{-2}\sum_{i,j=1}^{N} |g_{ij}(D_1^-\Psi_{ij}, D_1^+\Psi_{ij}, D_2^-\Psi_{ij}, D_2^+\Psi_{ij})|^2 \;.$$

The formal algorithm now reads:

initialize $\Psi_{ij} = 0$ for all $i, j = 1, .., N$
while $\bar{g} \geq$ 5.0e−3
  for $i, j = 1$ **to** N
    compute Ψ_{zero} as the upper zero of the function
      $\Psi_{ij} \mapsto g_{ij}(D_1^- \Psi_{ij}, D_1^+ \Psi_{ij}, D_2^- \Psi_{ij}, D_2^+ \Psi_{ij})$
    (we apply Newton's method for this purpose,
     with a fixed number of 20 iterations);
    replace Ψ_{ij} by Ψ_{zero}.
  end
end

For our numerical experiments on the square $\Omega = (0,1)^2$ we choose $N = 255$. As outlined in Section 6.2 we interpret the Cartesian grid as a triangulation of type $\mathcal{Q}_\lambda$ with $\lambda = 1/255$. The values Ψ_{ij} at the nodal points x_{ij} then define in a unique way a finite element function $\psi_\lambda \in P^1_{0,\lambda}$. In order to advance the resolution of the constructed magnetization, we refine the original triangulation $\mathcal{T}_h$ to $\mathcal{T}_\nu$ such that $|T| \leq$ 5.0e–3 holds for all triangles $T \in \mathcal{T}_\nu$. The new magnetization m_ν is then given by (6.17).

The advantage of projecting ψ_λ onto the finer triangulation $\mathcal{T}_\nu$ instead of the original triangulation $\mathcal{T}_h$ is illustrated in Figures 6.3 and 6.4: the contour plot of $\psi_\nu = \Pi_\nu^v \psi_\lambda$ exhibits a reduction of grid effects as compared to $\psi_h = \Pi_h^v \psi_\lambda$.

To measure the deviation from unit length of the resulting magnetization m_ν, we introduce the following average value:

$$H_{dev} \;=\; |\Omega|^{-1} \sum_{T \in \mathcal{T}_\nu} |T| \left(1 - |m_\nu(x_T)|^2\right)^2 \;. \tag{6.21}$$

We note that in this definition $m_\nu(x_T)$ is nothing but the mean value of the field m_ν on T,

$$m_\nu(x_T) \;=\; |T|^{-1} \int_T m_\nu(x)\, dx \;.$$

We also introduce the extremal values

$$\max |m_T| \;:=\; \max_{T \in \mathcal{T}_\nu} |m_\nu(x_T)| \;, \quad \text{and} \quad \min |m_T| \;:=\; \min_{T \in \mathcal{T}_\nu} |m_\nu(x_T)| \;. \tag{6.22}$$

In Table 6.3 we document for each field strength $|H_{ext}|$ the average deviation from unit length, the number of Gauss–Seidel iterations required, and the CPU time in seconds. The external fields H_{ext} are applied along the diagonal of $\Omega = (0,1)^2$, and the analytic center m_h^* is computed in advance by the IPM algorithm of Section 5.11. All numerical experiments were done on a Pentium III processor running at 700 MHz.

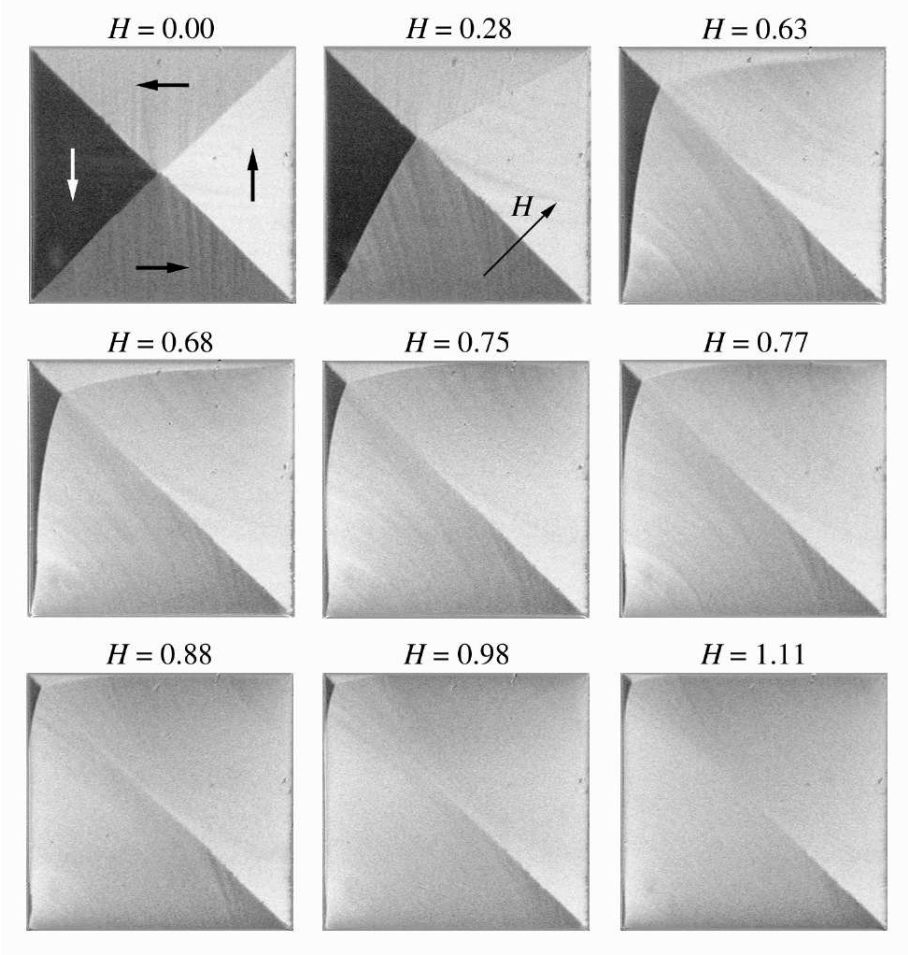

Figure 6.1: Experimental pictures of ac–demagnetized Permalloy ($Ni_{81}Fe_{19}$, $J_s = 1.0$ T). The square samples are of edge length 60 μm and thickness 230 nm in a digitally enhanced Kerr microscope. The external magnetic field H_{ext} is applied in–plane along the diagonal of the square samples. The various field strengths are denoted by $H = |H_{ext}|$, scaled as in (6.23). The pictures show regions of nearly constant magnetization, the *domains*, separated by thin layers, the *walls*. The pictures document the response of the thin film to the external field: the magnetization tends to align to H_{ext}, a deformation of domains is thus observed. At a critical field strength (here at about $H = 0.77$), walls are expelled from the sample. All pictures courtesy of R. Schäfer and first published in [17].

To visualize the solution m_ν, we present in Figure 6.2 a grayscale plot of the vertical component of $m_\nu(x_T)$, $T \in \mathcal{T}_\nu$, generated by the PDE Toolbox of MATLAB. We confront our numerical plots with experimental pictures of Permalloy films published in [17]. The experimental pictures in Figure 6.1 show ac–demagnetized Permalloy ($Ni_{81}Fe_{19}$, $J_s = 1.0$ T) square samples of edge length $L = 60\mu$m and thickness $D = 230$ nm in a digitally enhanced Kerr microscope. The experimental field strength h_{ext}, measured in Tesla, is scaled according to

$$|H_{ext}| \;=\; H \;=\; \frac{Lh_{ext}}{DJ_s}\;. \tag{6.23}$$

$\lvert H_{ext}\rvert$	sweeps	CPU (s)	H_{dev}	$\max \lvert m_T\rvert - 1$	$\min \lvert m_T\rvert$	IPM (s)
0.28	255	179	1.58e–3	4.43e–3	1.90e–1	3.5e+2
0.63	250	175	1.90e–3	8.73e–3	2.15e–1	9.0e+2
0.68	245	170	1.99e–3	5.44e–3	3.94e–1	9.5e+2
0.75	254	178	2.20e–3	8.70e–3	2.96e–1	1.5e+3
0.77	255	180	2.45e–3	1.09e–2	6.41e–2	1.8e+3
0.88	251	176	2.57e–3	1.00e–2	5.54e–2	2.5e+3
0.98	255	180	2.45e–3	5.21e–2	4.76e–2	3.4e+3
1.11	250	176	2.65e–3	2.27e–2	5.22e–2	1.1e+4

Table 6.1: Our simple finite difference scheme on $\Omega = (0,1)^2$ shows high degrees of accuracy in practice: here "sweeps" denotes the number of Gauss–Seidel iterations, the CPU time is documented in seconds. The following three columns reveal that the deviation from unit length is predominantly due to magnetization vectors that vanish on Ω. In the last column we recall the CPU time (in seconds) for the preprocessing IPM of Section 5.11; the IPM algorithm provides the analytic center m_h^*. The case $|H_{ext}| = 0$ is trivial, since then $m_h^* \equiv 0$ and ψ_λ is just the distance function w. r. t. $\partial\Omega$.

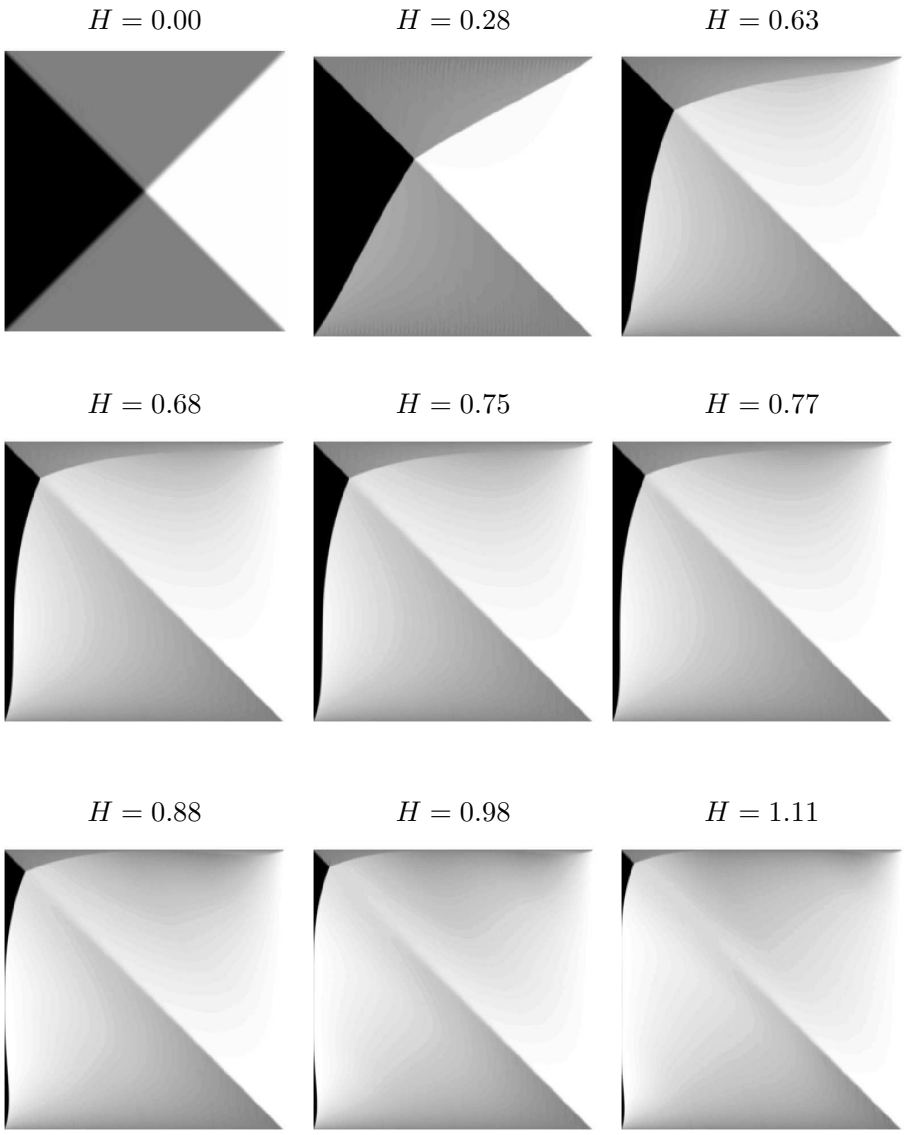

Figure 6.2: Grayscale plots of the vertical component of $m_\nu(x_T)$ on $\mathcal{T}_\nu$, generated by the MATLAB PDE Toolbox. These plots correspond to the numerical simulations documented in Table 6.3. Our numerical results are in good agreement with the experimental observations of Figure 6.1, though the critical field strength at which wall expulsion occurs is apparently higher in our simulations (at about $H = 0.88$).

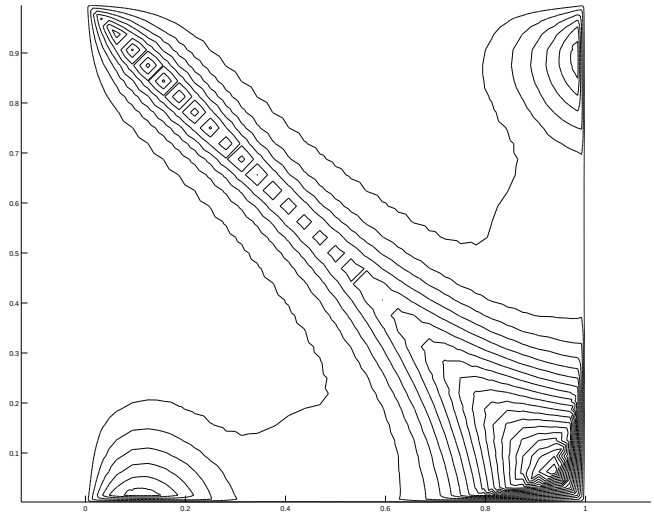

Figure 6.3: A contour plot of $\Pi_h^v \psi_\lambda$ with 20 lines for the external field $H_{ext} = (0.7, 0.7)$. It reveals considerable grid effects along the diagonal from the upper left to the lower right.

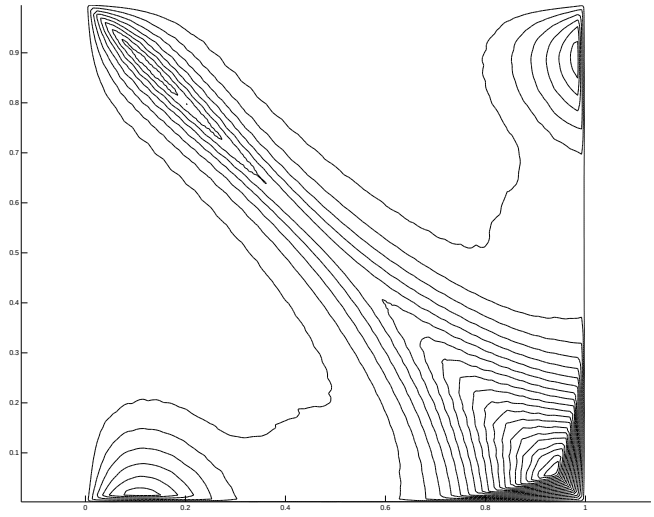

Figure 6.4: A contour plot of $\Pi_\nu^v \psi_\lambda$ with 20 lines for the external field $H_{ext} = (0.7, 0.7)$. Grid effects are reduced. Moreover, the corresponding magnetization m_ν is of the same energy as m_h^*.

6.4 Implementation and Results on General Triangulations

We apply a two–step algorithm to solve problem (6.11) for arbitrary shaped domains Ω: the first part is based on a scheme approximating viscosity solutions as introduced in [6], and is followed by a postprocessing step that adjusts the length of the resulting magnetization.

We consider the alternative triangulation $\mathcal{T}_\lambda$ and its vertices $\mathcal{V}_\lambda$. Let $\mathcal{V}_\lambda^\circ$ denote the subset of vertices that lie in the interior of Ω, and let $\partial\mathcal{V}_\lambda$ denote the set of those vertices that lie on the boundary $\partial\Omega$. Therefore we have $\mathcal{V}_\lambda^\circ \cup \partial\mathcal{V}_\lambda = \mathcal{V}_\lambda$ and $\mathcal{V}_\lambda^\circ \cap \partial\mathcal{V}_\lambda = \emptyset$. A function $\psi_\lambda \in P^1_{0,\lambda}$ is uniquely determined by its values on $\mathcal{V}_\lambda^\circ$. For any $x_\lambda \in \mathcal{V}_\lambda^\circ$ we define the simplicial neighborhood $\omega_\lambda(x_\lambda)$ of x_λ as the union of all triangles $T \in \mathcal{T}_\lambda$ with $x_\lambda \in \overline{T}$, see Figure 6.5.

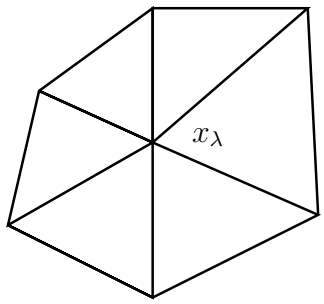

Figure 6.5: The patch $\omega_\lambda(x_\lambda)$ is defined as the simplicial neighborhood of $x_\lambda \in \mathcal{V}_h^\circ$.

The main idea in [6] is to construct a solution ψ_λ to (6.13) that is defined implicitly by a fixed point equation of the kind

$$\psi_\lambda \;=\; \Lambda_\lambda \psi_\lambda \;, \tag{6.24}$$

where the operator $\Lambda_\lambda : P^1_{0,\lambda} \to P^1_{0,\lambda}$ is based on a local version of the Hopf–Lax formula (6.9) as restricted to patches $\omega_\lambda(x_\lambda)$. Then we solve (6.24) explicitly by the fixed point iteration

$$\psi_\lambda^{n+1} \;=\; \Lambda_\lambda \psi_\lambda^n \;, \qquad n = 0, 1, 2, .. \;, \tag{6.25}$$

with the initial choice $\psi_\lambda^0 \equiv 0$. This nonlinear version of a Jacobi iteration is replaced in practice by a corresponding Gauss–Seidel iteration as in the finite difference scheme of [48] that we presented in the preceeding section.

Provided the Hamiltonian H is continuous, the operator Λ_λ is defined in [6] by setting

$$(\Lambda_\lambda \psi_\lambda)(x_\lambda) \;=\; \min_{y \in \partial\omega_\lambda(x_\lambda)} \left(\psi_\lambda(y) + \rho(x_\lambda, x_\lambda - y)\right) \qquad \text{for all } x_\lambda \in \mathcal{V}_\lambda^\circ \;. \tag{6.26}$$

The "freezing" of the x–dependence in the support function ρ is necessary to guarantee that the optical distance from x_λ to a boundary point y of $\omega_\lambda(x_\lambda)$ is given by

$$\delta(x_\lambda, y) \;=\; \rho(x_\lambda, x_\lambda - y) \;, \tag{6.27}$$

which implies that the infimum in (6.8) is attained for the straight line joining x_λ and y. This observation is crucial in constructing an explicit solution scheme for (6.24), since otherwise we would have to consider the generally nontrivial variational problem (6.8) on each patch $\omega_\lambda(x_\lambda)$. Moreover, the choice (6.26) allows for rigorous first order convergence results as proven in [6].

The situation is more delicate in case of problem (6.11): for the Hamiltonian $H(x,p) = |p - m_h^\perp(x)|^2 - 1$ the support function ρ of the zero–level set is given by

$$\rho(x,q) \;=\; \max_{H(x,p)=0} p\cdot q \;=\; |q| + m_h^\perp(x)\cdot q \;. \tag{6.28}$$

This Hamiltonian H is *not* continuous in the space variable x for generic $m_h \in RT_{0,h}$. Therefore we have to modify the definition (6.26) of Λ_λ.

To simplify our notation, we set for any given triangle $T \in \mathcal{T}_\lambda$ with barycenter x_T

$$m_T^\perp \;:=\; (m_h^*)^\perp(x_T) \;=\; \left(\Pi_\lambda^t m_h^*\right)^\perp \;.$$

Next we introduce a solution scheme for problem (6.13): for given $x_\lambda \in \mathcal{V}_\lambda^\circ$ we let $e_1,..,e_m$ denote the triangle edges that make up the boundary of the patch $\omega_\lambda(x_\lambda)$ and define

$$\psi_i \;:=\; \min_{y\in e_i}(\psi_\lambda(y) + |x_\lambda - y| + m_T^\perp\cdot(x_\lambda - y)) \;. \tag{6.29}$$

The operator Λ_λ is then defined by setting

$$(\Lambda_\lambda\psi_\lambda)(x_\lambda) \;=\; \min_{1\le i\le m}\psi_i \;. \tag{6.30}$$

We notice that (6.29) constitutes a convex optimization problem since ψ_λ is affine and $y \mapsto |x_\lambda - y| + m_T^\perp\cdot(x_\lambda - y)$ is convex. For vanishing $m_h^* \equiv 0$ the boundary value problem (6.1) reduces to

$$|\nabla\psi(x)|^2 \;=\; 1 \quad \text{for } x\in\Omega \quad \text{and} \quad \psi(x) \;=\; 0 \quad \text{for } x\in\partial\Omega \;, \tag{6.31}$$

the corresponding problem for the *eikonal equation*. The operator (6.26) then reduces to

$$(\Lambda_\lambda\psi_\lambda)(x_\lambda) \;=\; \min_{y\in\partial\omega_\lambda(x_\lambda)}(\psi_\lambda(y) + |x_\lambda - y|) \qquad \text{for all } x_\lambda\in\mathcal{V}_\lambda^\circ \;,$$

and both defintions (6.26) and (6.30) coincide, since the update (6.29) is now given by

$$\psi_i \;:=\; \min_{y\in e_i}(\psi_\lambda(y) + |x_\lambda - y|) \;.$$

This ψ_i can be determined explicitly as shown in [6]: we consider a triangle $T \in \mathcal{T}_\lambda$ with vertices x_λ, y_λ and z_λ, and denote the angles at y_λ and z_λ by α and β, respectively. See Figure 6.6.

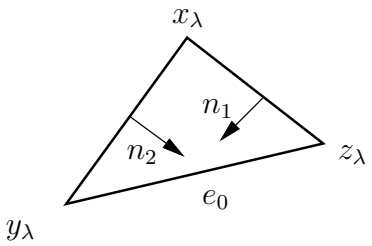

Figure 6.6: A single triangle T of the patch $\omega_\lambda(x_\lambda)$.

For $\psi_\lambda \in P^1_{0,\lambda}$ we define the slope

$$D \;:=\; \frac{\psi_\lambda(z_\lambda) - \psi_\lambda(y_\lambda)}{|z_\lambda - y_\lambda|} \;,$$

and if $|D| \leq 1$ we introduce the parameter δ given by $\cos\delta = D$. Then we have

$$\begin{aligned} \psi_i \;&=\; \min_{y\in[y_\lambda,z_\lambda]} (\psi_\lambda(y) + |x_\lambda - y|) \;=\; \psi_\lambda(y_\lambda) + \min_{y\in[y_\lambda,z_\lambda]} (D|y-y_\lambda| + |x_\lambda - y|) \qquad (6.32) \\ &=\; \begin{cases} \psi_\lambda(y_\lambda) + |x_\lambda - y_\lambda| & \cos\alpha \leq D \\ \psi_\lambda(y_\lambda) + \cos(\delta-\alpha)|x_\lambda - y_\lambda| & \alpha \leq \delta \leq \pi - \beta \\ \psi_\lambda(z_\lambda) + |x_\lambda - z_\lambda| & D \leq \cos(\pi-\beta) \;. \end{cases} \end{aligned}$$

For an efficient implementation of formula (6.32) we refer to [6].

The local variational problem (6.29) requires to minimize edgewise in y the function

$$\psi_\lambda(y) + |x_\lambda - y| + m_T^\perp \cdot (x_\lambda - y) \;,$$

where

$$\begin{aligned} m_T^\perp \cdot (x_\lambda - y) \;&=\; m_T^\perp \cdot (x_\lambda - y_\lambda) - m_T^\perp \cdot (y - y_\lambda) \\ &=\; m_T^\perp \cdot (x_\lambda - y_\lambda) - \frac{m_T^\perp \cdot (z_\lambda - y_\lambda)}{|z_\lambda - y_\lambda|}|y - y_\lambda| \;. \end{aligned}$$

However, since the restriction of ψ_λ on edges results in an affine function, we have

$$\psi_\lambda(y) \;=\; \psi_\lambda(y_\lambda) + \frac{\psi_\lambda(z_\lambda) - \psi_\lambda(y_\lambda)}{|z_\lambda - y_\lambda|}|y - y_\lambda| \;,$$

and the combination of the preceeding two equations yields

$$\begin{aligned} &\psi_\lambda(y) + |x_\lambda - y| + m_T^\perp \cdot (x_\lambda - y) \\ &=\; \psi_\lambda(y_\lambda) + m_T^\perp \cdot (x_\lambda - y_\lambda) + |x_\lambda - y| + \frac{\psi_\lambda(z_\lambda) - \psi_\lambda(y_\lambda) - m_T^\perp \cdot (z_\lambda - y_\lambda)}{|z_\lambda - y_\lambda|}|y - y_\lambda| \;. \end{aligned}$$

Thus the update (6.29) can be written as

$$\begin{aligned}\psi_i &= \min_{y\in[y_\lambda,z_\lambda]} \big(\psi_\lambda(y) + |x_\lambda - y| + m_T^\perp \cdot (x_\lambda - y)\big) \\ &= \psi_\lambda(y_\lambda) + m_T^\perp \cdot (x_\lambda - y_\lambda) + \min_{y\in[y_\lambda,z_\lambda]} (D|y-y_\lambda| + |x_\lambda - y|) \ , \end{aligned} \tag{6.33}$$

where now

$$D := \frac{\psi_\lambda(z_\lambda) - \psi_\lambda(y_\lambda) - m_T^\perp \cdot (z_\lambda - y_\lambda)}{|z_\lambda - y_\lambda|} \ .$$

Since the first two terms in (6.33) do not depend on y, this update ψ_i is also given explicitly by formula (6.32). Thus we compute an approximate solution to

$$\left.\begin{array}{rc} \psi_\lambda & \overset{(6.24)}{=} \Lambda_\lambda \psi_\lambda \\ (\Lambda_\lambda\psi_\lambda)(x_\lambda) & \overset{(6.30)}{=} \min_{1\le i\le m} \psi_i \\ \psi_i & \overset{(6.29)}{=} \min_{y\in e_i}(\psi_\lambda(y) + |x_\lambda - y| + m_T^\perp \cdot (x_\lambda - y)) \end{array}\right\} \tag{6.34}$$

by the Gauss–Seidel algorithm in [6]. We apply a fixed number of 100 Gauss–Seidel iterations, i. e. every vertex $x_\lambda \in \mathcal{V}_\lambda^\circ$ is reached exactly 100 times; we do not have any advanced stopping criterion at hand yet that guarantees a comparable quality of the approximate solution without slowing down the algorithm considerably.

Our final numerical solution to problem (6.13) depends on some postprocessing, a length–correcting algorithm based on the following observation:

Lemma 6.1. *Let the triangle $T \in \mathcal{T}_\lambda$ be given with notations as in Figure 6.6. Let us further assume that the function $\psi_\lambda \in P^1_{0,\lambda}$ satisfies*

$$\psi_\lambda(x_\lambda) = \min_{y\in e_0} \big(\psi_\lambda(y) + |x_\lambda - y| + m_T^\perp \cdot (x_\lambda - y)\big) \ . \tag{6.35}$$

Then the gradient $\nabla\psi_\lambda$ fulfills on T the condition

$$|\nabla\psi_\lambda - m_T^\perp|^2 = 1 \tag{6.36}$$

if and only if

$$(\nabla\psi_\lambda - m_T^\perp)\cdot n_1 \le 0 \quad \textit{and} \quad (\nabla\psi_\lambda - m_T^\perp)\cdot n_2 \le 0 \ . \tag{6.37}$$

Proof of Lemma 6.1.
Let $y^* \in [y_\lambda, z_\lambda]$ denote the point on edge e_0 where the right hand side of (6.35) attains its minimum. Then we have

$$\psi_\lambda(x_\lambda) = \psi_\lambda(y^*) + |x_\lambda - y^*| + m_T^\perp \cdot (x_\lambda - y^*) \ ,$$

or rather

$$\frac{\psi_\lambda(x_\lambda) - \psi_\lambda(y^*)}{|x_\lambda - y^*|} - \frac{m_T^\perp \cdot (x_\lambda - y^*)}{|x_\lambda - y^*|} = 1 \ .$$

Since $\psi_\lambda \in P^1_{0,\lambda}$, we may rewrite the last equation as

$$\left(\nabla\psi_\lambda - m_T^\perp\right) \cdot \frac{x_\lambda - y^*}{|x_\lambda - y^*|} \;=\; 1 \;. \tag{6.38}$$

Thus, if (6.36) holds, (6.38) enforces the identity

$$\nabla\psi_\lambda - m_T^\perp \;=\; \frac{x_\lambda - y^*}{|x_\lambda - y^*|} \;,$$

and this implies the normal condition (6.37). It remains to proof the converse statement: for that purpose, let condition (6.37) be satisfied. Then there exists a point $\tilde{y} \in e_0$ such that

$$\frac{\nabla\psi_\lambda - m_T^\perp}{|\nabla\psi_\lambda - m_T^\perp|} \;=\; \frac{x_\lambda - \tilde{y}}{|x_\lambda - \tilde{y}|} \;. \tag{6.39}$$

Now if $\tilde{y} \neq y^*$, by (6.38) there follows

$$\begin{aligned} 1 \;&<\; |\nabla\psi_\lambda - m_T^\perp|^2 \\ &=\; \left(\nabla\psi_\lambda - m_T^\perp\right) \cdot \frac{x_\lambda - \tilde{y}}{|x_\lambda - \tilde{y}|} \\ &=\; \frac{\psi_\lambda(x_\lambda) - \psi_\lambda(\tilde{y})}{|x_\lambda - \tilde{y}|} - \frac{m_T^\perp \cdot (x_\lambda - \tilde{y})}{|x_\lambda - \tilde{y}|} \;. \end{aligned}$$

Taking into account the definition of y^* this implies

$$\begin{aligned} \psi_\lambda(x_\lambda) \;&>\; \psi_\lambda(\tilde{y}) + |x_\lambda - \tilde{y}| + m_T^\perp \cdot (x_\lambda - \tilde{y}) \\ &\geq\; \psi_\lambda(y^*) + |x_\lambda - y^*| + m_T^\perp \cdot (x_\lambda - y^*) \\ &=\; \psi_\lambda(x_\lambda) \;. \end{aligned}$$

So we have $\tilde{y} = y^*$ by contradiction, and (6.36) is a consequence of (6.39) and (6.38).

□

Lemma 6.1 indicates a connection between the normal condition (6.37) and the unit length property (6.36) for approximate solutions of (6.24). We are not able yet to prove a deeper result; however, the normal condition (6.37) is well–known from numerical schemes for *time–dependent* Hamilton–Jacobi equations on triangulated domains, see [2] for details. There one defines numerical Hamiltonians for arguments $\psi_\lambda \in P^1_{0,\lambda}, x_\lambda \in \mathcal{V}^\circ_\lambda$, and $\psi^+ \in \mathbb{R}$ by

$$H_\alpha(\psi_\lambda, x_\lambda, \psi^+) \;:=\; \max_{T \subset \omega_\lambda(x_\lambda)} \alpha_T \left(|\nabla\psi^+_\lambda - m_T^\perp|^2 - 1\right) \;,$$

where

$$\alpha_T \;:=\; \begin{cases} 1 & \text{if} \qquad \psi^+_\lambda \text{ satisfies (6.37) on } T \;, \\ 0 & \text{else} \quad . \end{cases}$$

Here ψ^+_λ denotes the $P^1_{0,\lambda}$–function resulting from ψ_λ by replacing the value $\psi_\lambda(x_\lambda)$ by $\psi^+ \in \mathbb{R}$ and leaving all other nodal values unchanged.

The function H_α is convex but not differentiable with respect to the variable $\psi^+ \in \mathbb{R}$. Thus for fixed $(\psi_\lambda, x_\lambda)$ we compute the upper zero of $\psi^+ \mapsto H_\alpha(\psi_\lambda, x_\lambda, \psi^+)$ by the bisection method.

This motivates the following two–step algorithm:

initialize $\psi_\lambda^0 \equiv 0$
for $n = 1$ **to** 100
    $\psi_\lambda^{n+1} = \Lambda_\lambda \psi_\lambda^n$,
    where Λ_λ is defined in (6.30)
    and evaluated by the implementation [6] of (6.32);
end
for $n = 100$ **to** 110
    sweep through all $x_\lambda \in \mathcal{V}_\lambda^\circ$
        compute the upper zero ψ_{zero}^+ of
            $\psi^+ \mapsto H_\alpha(\psi_\lambda^n, x_\lambda, \psi^+)$
        by the bisection method (fixed number of 30 iterations);
        $\psi_\lambda^{n+1}(x_\lambda) \ := \ \psi_{zero}^+$;
    end
end

In our numerical experiments we choose as $\mathcal{T}_\lambda$ the approximate circular triangulation in Figure 5.7. The function $\psi_\lambda := \psi_\lambda^{110}$ computed by the above algorithm is projected thereafter as in (6.14), i. e. $\psi_h = \Pi_h^v \psi_\lambda$. Here $\mathcal{T}_h$ denotes the refined circular triangulation illustrated in Figure 5.8. With the analytic center m_h^* computed by the IPM in Section 5.11, this yields a magnetization

$$m_h \ = \ \nabla^\perp \psi_h + m_h^* \tag{6.40}$$

close to unit length. We document and comment on the results of the above algorithm in Table 6.2. As in the preceeding section, we measure the average deviation from unit length by

$$H_{dev} \ = \ |\Omega|^{-1} \ \sum_{T \in \mathcal{T}_h} |T| \left(1 - |m_h(x_T)|^2 \ \right)^2 \ . \tag{6.41}$$

We also introduce the extremal values

$$\max |m_T| \ := \ \max_{T \in \mathcal{T}_h} |m_h(x_T)| \ , \quad \text{and} \quad \min |m_T| \ := \ \min_{T \in \mathcal{T}_h} |m_h(x_T)| \ . \tag{6.42}$$

All numerical experiments were done on a Pentium III processor running at 700 MHz.

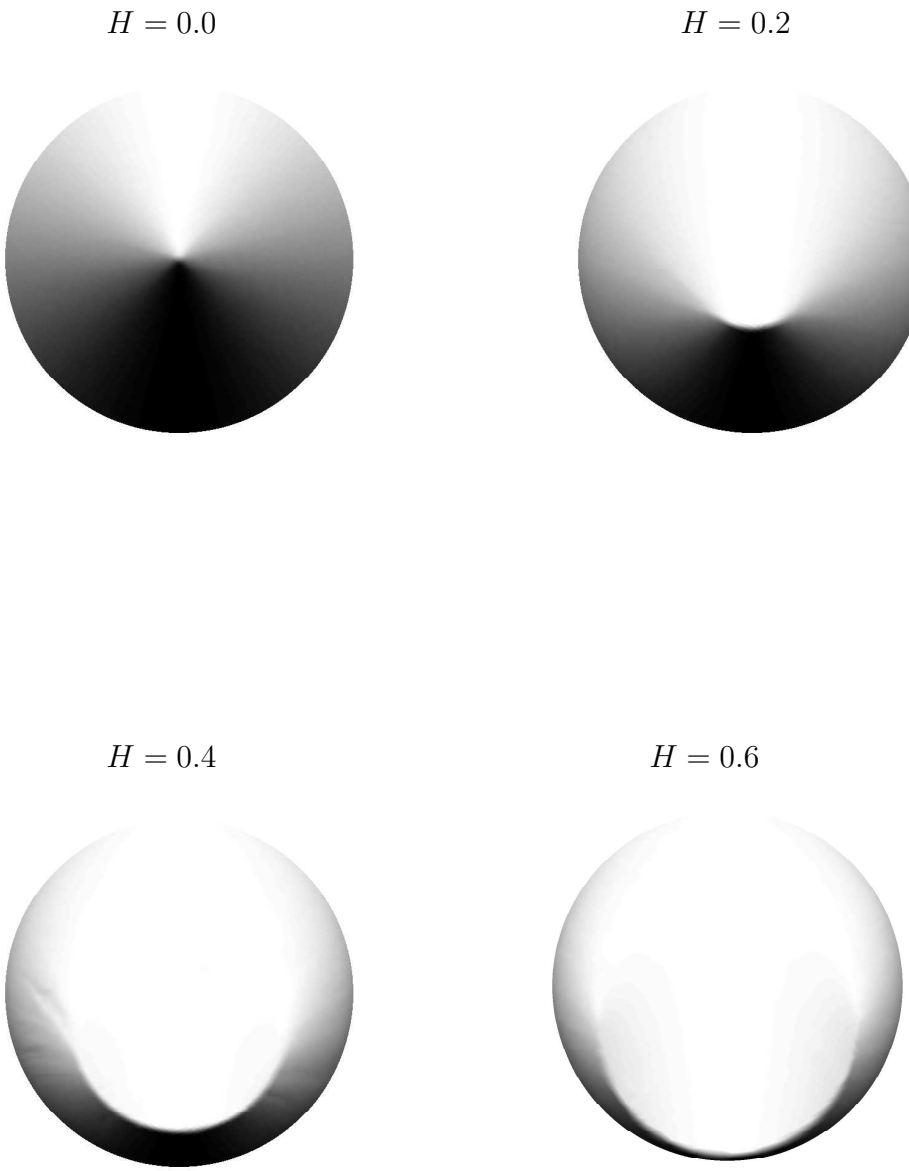

Figure 6.7: Numerical simulations on a circular, polygonal domain approximating $B_1(0) \subset \mathbb{R}^2$. A vortex, visible at the center $(0, 0)$ for $H = 0.0$, is deformed under external field into a wall approaching the boundary. The physical setting is quasi–stationary, no time–dependence is included. The external field H_{ext} is directed along the horizontal axis, the field strength is denoted by $H = |H_{ext}|$. These numerical simulations coincide with predictions of the ad hoc model [10]. Experimental observations in [36] confirm the simulations qualitatively.

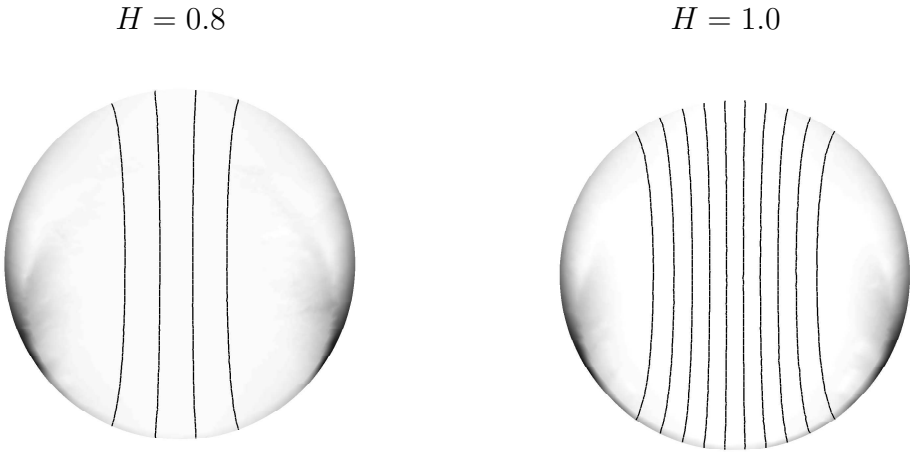

Figure 6.8: Additional numerical simulations on the circular domain. At a critical field strength ($H > 0.6$) the external field is not compensated by the stray field anymore: it penetrates the sample. These predictions go beyond [10]. The reduced model [16] considered here holds also for non–vanishing fields $-\nabla u + H_{ext}$, lines show the level curves of the corresponding potential. Here the potential takes values around zero in $(-0.4, 0.4)$ and differs by 0.05 at neighboring lines.

In Figures 6.9 and 6.10 we provide contour plots of the approximate viscosity solutions $\psi_\lambda = \psi_\lambda^{110}$ for two different external fields. To take a closer look at the features of our two–step algorithm, a contour plot of the interim solution ψ_λ^{100} is provided in Figure 6.11: distinct grid effects are visible near the boundary $\partial\Omega$. The corrections by the postprocessing step are evident from Figure 6.10. This bisection step on the discrete Hamiltonian H_α is not a suitable numerical scheme on its own for the approximation of the viscosity solution: when started with initial value $\psi_\lambda^0 \equiv 0$, the iterates fail to grow towards the viscosity solution in the interior of Ω; see Figure 6.12.

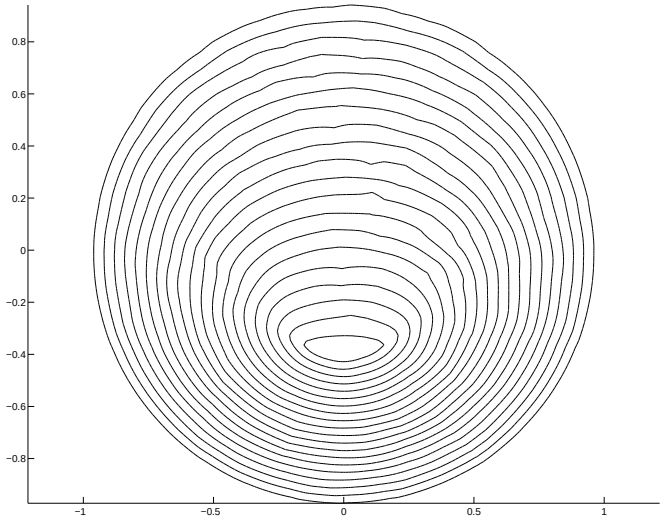

Figure 6.9: A contour plot of ψ_λ with 20 lines for the external field $H_{ext} = (0.2, 0.0)$. We have $0 \leq \psi_\lambda \leq 0.83$.

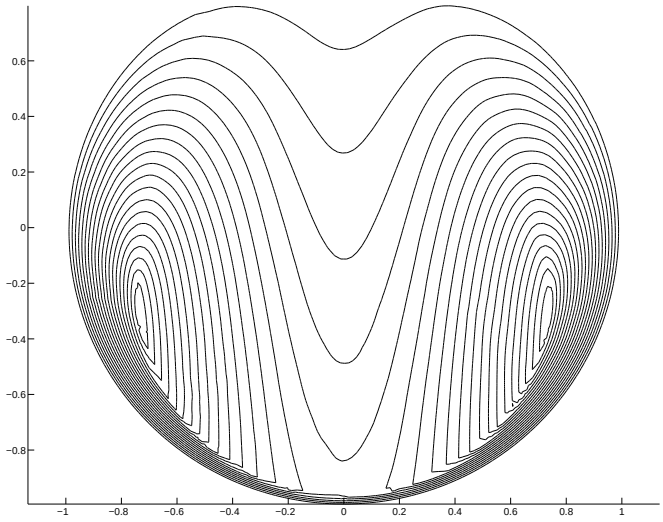

Figure 6.10: A contour plot of ψ_λ with 20 lines for the external field $H_{ext} = (0.6, 0.0)$. We have $0 \leq \psi_\lambda \leq 0.24$.

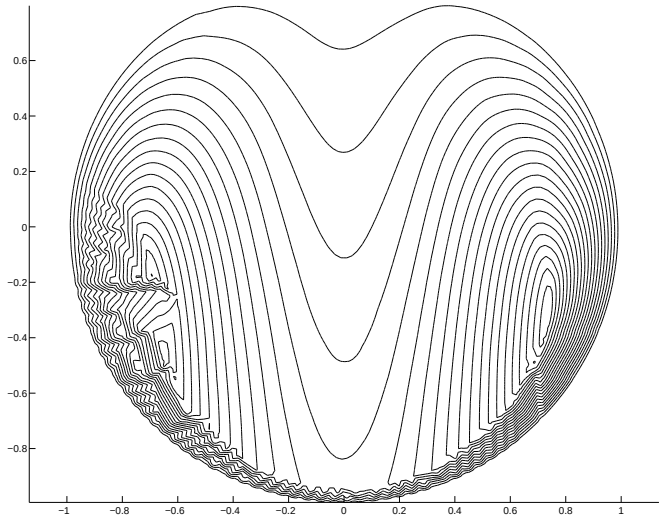

Figure 6.11: A contour plot of ψ_λ^{100} with 20 lines for the external field $H_{ext} = (0.6, 0.0)$. We have also $0 \leq \psi_\lambda^{100} \leq 0.24$, but grid effects are visible on the left. The result is not improved even if we raise the number of iterations up to 1000. Thus a postprocessing step is necessary.

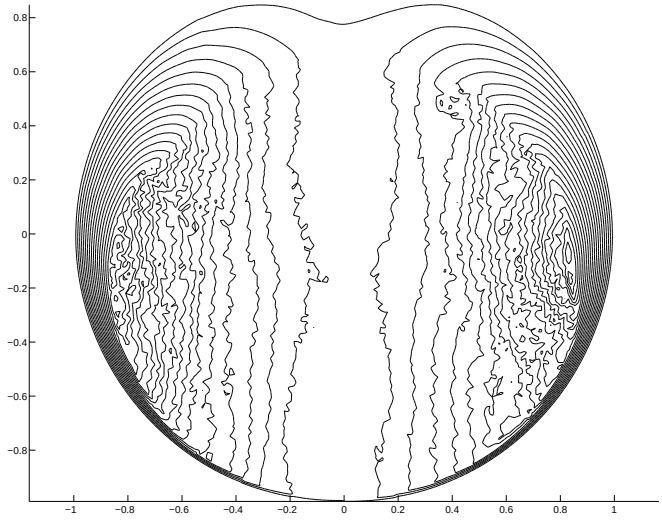

Figure 6.12: A contour plot of ψ_λ when only the postprocessing step is applied on initial choice $\psi_\lambda^0 \equiv 0$; with 20 lines for the external field $H_{ext} = (0.6, 0.0)$. We have only $0 \leq \psi_\lambda \leq 0.15$. The result is not improved even if we raise the number of iterations from 10 to 100.

Further, in Figures 6.7 and 6.8, we provide grayscale plots of the vertical component of $m_h(x_T)$, just as we did in Figure 6.2 before. So far, we do not have corresponding pictures from physical experiments at hand to confront with. However, our numerical simulations reveal a qualitative behavior of circular thin films under external field that is also observed in practice: a vortex is expelled from a circular thin film by an external field via domain wall formation.

$\lvert H_{ext}\rvert$	CPU 1	CPU 2	H^1_{dev}	H^2_{dev}	$\max \lvert m_T\rvert - 1$	$\min \lvert m_T\rvert$
0.2	12	59	3.7e–2	3.4e–3	2.2e–1	2.0e–2
0.4	13	55	5.8e–2	4.9e–3	3.8e–1	2.5e–2
0.6	11	57	3.2e–2	3.3e–3	1.9e–1	1.8e–3
0.8	12	61	6.1e–2	4.1e–3	3.1e–1	1.0e–3
1.0	12	60	2.2e–2	4.8e–3	4.0e–1	1.2e–3

Table 6.2: We document the CPU times in seconds for both steps of the above algorithm; "CPU 1" denotes the time for the fixed point iteration, whereas "CPU 2" denotes that of the postprocessing bisection method on the discrete Hamiltonian H_α. We notice that the bisection method slows down the algorithm considerably. However, it guarantees a sufficient decrease in the average deviation from unit length, from H^1_{dev} for the fixed point iteration, to H^2_{dev} due to the postprocessing. The last two columns show that the pointwise deviation from unit length exceeds that of the finite difference scheme on rectangular samples, see Table 6.3 in the preceeding section. The case $|H_{ext}| = 0$ is trivial, since then $m_h = \Pi^e_h m$ with $m(x) = (-x_2, x_1)/|x|$.

7 Appendix: The Self–Energy of T_{ref}

Here we present the derivation of the self–energy $I(T_{ref})$ for the reference triangle in Lemma 4.1.

The following one–dimensional integrations will be helpful. They are based on antiderivatives listed in the succeeding Lemma 7.2.

Lemma 7.1. *We have*

$$\int_{a=0}^{a=1} a(1-a)\log(1-a+\sqrt{a^2+(1-a)^2})\;da = -\tfrac{2}{9} - \tfrac{5}{24}\sqrt{2}\log(-1+\sqrt{2}), \quad (7.1)$$

$$\int_{a=0}^{a=1} (1-a)^2\log(\pm a+\sqrt{a^2+(1-a)^2})\;da = -\tfrac{1}{9} \pm \tfrac{1}{12} \mp \tfrac{1}{24}\sqrt{2}\log(-1+\sqrt{2}). \quad (7.2)$$

Proof of Lemma 7.1.
By partial integration we conclude

$$\begin{aligned}
&\int_{a=0}^{a=1} a(1-a)\log(1-a+\sqrt{a^2+(1-a)^2})\;da \\
= &-\int_{a=0}^{a=1} (\tfrac{1}{2}a^2-\tfrac{1}{3}a^3)\tfrac{1}{1-a+\sqrt{a^2+(1-a)^2}}\left(\tfrac{2a-1}{\sqrt{a^2+(1-a)^2}}-1\right)\;da \\
= &\int_{a=0}^{a=1} \frac{\frac{1}{2}a^2-\frac{1}{3}a^3}{1-a+\sqrt{a^2+(1-a)^2}} - \frac{(\frac{1}{2}a^2-\frac{1}{3}a^3)(2a-1)}{(1-a+\sqrt{a^2+(1-a)^2})\sqrt{a^2+(1-a)^2}}\;da\;.
\end{aligned}$$

The first integral yields

$$\begin{aligned}
\int_{a=0}^{a=1} \frac{\frac{1}{2}a^2-\frac{1}{3}a^3}{1-a+\sqrt{a^2+(1-a)^2}}\;da &= \int_{a=0}^{a=1} (\tfrac{1}{3}a-\tfrac{1}{2})(1-a-\sqrt{a^2+(1-a)^2})\;da \\
&\overset{(7.9),(7.10)}{=} -\tfrac{1}{36}-\tfrac{1}{12}\sqrt{2}\log(-1+\sqrt{2})\;. \quad (7.3)
\end{aligned}$$

The second integral gives

$$\begin{aligned}
&\int_{a=0}^{a=1} \frac{(\frac{1}{2}a^2-\frac{1}{3}a^3)(2a-1)}{(1-a+\sqrt{a^2+(1-a)^2})\sqrt{a^2+(1-a)^2}}\;da \\
= &\int_{a=0}^{a=1} \frac{(\frac{1}{3}a-\frac{1}{2})(2a-1)(1-a-\sqrt{a^2+(1-a)^2})}{\sqrt{a^2+(1-a)^2}}\;da \\
= &\int_{a=0}^{a=1} \frac{(\frac{1}{3}a-\frac{1}{2})(2a-1)(1-a)}{\sqrt{a^2+(1-a)^2}}\;da - \int_{a=0}^{a=1} (\tfrac{1}{3}a-\tfrac{1}{2})(2a-1)\;da \\
= &\tfrac{1}{4}+\tfrac{1}{9}\sqrt{2}\log(-1+\sqrt{2})-\tfrac{1}{18}\;, \quad (7.4)
\end{aligned}$$

where we have used the easily checked formula

$$\begin{aligned}
&\frac{d}{d\xi}\left(-\tfrac{1}{16}\sqrt{2}\,\mathrm{arsinh}(2\xi-1)-\tfrac{1}{9}\xi^2\sqrt{\xi^2+(1-\xi)^2}+\tfrac{13}{36}\xi\sqrt{\xi^2+(1-\xi)^2}-\tfrac{19}{72}\sqrt{\xi^2+(1-\xi)^2}\right) \\
&\qquad = \frac{(\frac{1}{3}\xi-\frac{1}{2})(2\xi-1)(1-\xi)}{\sqrt{\xi^2+(1-\xi)^2}}\;.
\end{aligned}$$

Summing up (7.3) and (7.4) yields (7.1).

Now we consider (7.2). By partial integration we get

$$\begin{aligned}
&\int_{a=0}^{a=1} (1-a)^2 \log(\pm a + \sqrt{a^2+(1-a)^2})\; da \\
= &\int_{a=0}^{a=1} \tfrac{1}{3}(1-a)^3 \tfrac{1}{\pm a+\sqrt{a^2+(1-a)^2}} \left(\tfrac{2a-1}{\sqrt{a^2+(1-a)^2}} \pm 1 \right)\; da \\
= &\int_{a=0}^{a=1} \frac{\pm\frac{1}{3}(1-a)^3}{\pm a + \sqrt{a^2+(1-a)^2}} + \frac{\frac{1}{3}(1-a)^3(2a-1)}{(\pm a + \sqrt{a^2+(1-a)^2})\sqrt{a^2+(1-a)^2}}\; da\ .
\end{aligned}$$

For the first integrand we have

$$\begin{aligned}
\int_{a=0}^{a=1} \frac{\pm\frac{1}{3}(1-a)^3}{\pm a + \sqrt{a^2+(1-a)^2}}\; da \;&=\; \int_{a=0}^{a=1} \pm\tfrac{1}{3}(1-a)(\mp a + \sqrt{a^2+(1-a)^2})\; da \\
&\overset{(7.9),(7.10)}{=}\; -\tfrac{1}{18} \pm \tfrac{1}{12} \mp \tfrac{1}{24}\sqrt{2}\log(-1+\sqrt{2})\ . \quad (7.5)
\end{aligned}$$

The second integral yields

$$\begin{aligned}
&\int_{a=0}^{a=1} \frac{\frac{1}{3}(1-a)^3(2a-1)}{(\pm a + \sqrt{a^2+(1-a)^2})\sqrt{a^2+(1-a)^2}}\; da \\
= &\int_{a=0}^{a=1} \frac{\frac{1}{3}(1-a)(2a-1)(\mp a + \sqrt{a^2+(1-a)^2})}{\sqrt{a^2+(1-a)^2}}\; da \\
= &\int_{a=0}^{a=1} \frac{\frac{1}{3}(1-a)(2a-1)(\mp a)}{\sqrt{a^2+(1-a)^2}}\; da + \int_{a=0}^{a=1} \tfrac{1}{3}(1-a)(2a-1)\; da \qquad (7.6) \\
= &\; -\tfrac{1}{18}\ , \qquad (7.7)
\end{aligned}$$

since the first integral in (7.6) vanishes due to the symmetry properties of the integrand. Summing up (7.5) and (7.7) establishes (7.2). □

Lemma 7.2. *Let $C > 0$ be a positive constant and the function $S = S(\xi)$ be defined by $S(\xi) = \sqrt{\xi^2+(1-\xi)^2}$. Then the following formulas for $0 \le \xi \le 1$ are easily checked by straightforward differentiation:*

$$\frac{d}{d\xi}\log(\xi + \sqrt{C+\xi^2}) \;=\; \frac{1}{\sqrt{C+\xi^2}}\ , \qquad (7.8)$$

$$\frac{d}{d\xi}\left((2\xi-1)S(\xi) + \tfrac{1}{2}\sqrt{2}\,\mathrm{arsinh}(2\xi-1)\right) \;=\; 4S(\xi)\ , \qquad (7.9)$$

$$\frac{d}{d\xi}\left(\tfrac{4}{3}S(\xi)^3 + (2\xi-1)S(\xi) + \tfrac{1}{2}\sqrt{2}\,\mathrm{arsinh}(2\xi-1)\right) \;=\; 8\xi S(\xi)\ , \qquad (7.10)$$

$$\frac{d}{d\xi}\left(\tfrac{1}{9}(1-\xi)^3 - \tfrac{1}{3}(1-\xi)^3\log(C(1-\xi))\right) \;=\; (1-\xi)^2\log(C(1-\xi))\ , \qquad (7.11)$$

$$\frac{d}{d\xi}\left(\xi\log(-\xi+\sqrt{\xi^2+C}) + \sqrt{\xi^2+C}\right) \;=\; \log(-\xi+\sqrt{\xi^2+C})\ . \qquad (7.12)$$

Proof of Lemma 4.1.
Since the function $f(x,y) = 1/|x-y|$ is integrable on $\mathbb{R}^4$, we reduce the calculation of the fourfold integral to repeated one–dimensional integrations. First we consider the integration w. r. t. the variables x_1 and y_1: for any positive constant $C > 0$ we have

$$\begin{aligned}
&\int_{y_1=0}^{y_1=1-b} \int_{x_1=0}^{x_1=1-a} \frac{1}{\sqrt{(x_1-y_1)^2+C}}\; dx_1\; dy_1 \\
= &\int_{y_1=0}^{y_1=1-b} \int_{\xi=-y_1}^{1-a-y_1} \frac{1}{\sqrt{\xi^2+C}}\; d\xi\; dy_1 \\
\overset{(7.8)}{=} &\int_{y_1=0}^{y_1=1-b} \log\left(1-a-y_1+\sqrt{(1-a-y_1)^2+C}\right) - \log\left(-y_1+\sqrt{y_1^2+C}\right)\; dy_1 \\
= &\int_{y_1=a-1}^{y_1=a-b} \log\left(-y_1+\sqrt{y_1^2+C}\right)\; dy_1 \; - \int_{y_1=0}^{y_1=1-b} \log\left(-y_1+\sqrt{y_1^2+C}\right)\; dy_1 \\
\overset{(7.12)}{=} &(a-b)\log(-(a-b)+\sqrt{(a-b)^2+C})+\sqrt{(a-b)^2+C} \\
&\quad -(a-1)\log(-(a-1)+\sqrt{(a-1)^2+C})-\sqrt{(a-1)^2+C} \\
&\quad -(1-b)\log(-(1-b)+\sqrt{(1-b)^2+C})-\sqrt{(1-b)^2+C}+\sqrt{C}\;.
\end{aligned}$$

We notice that the result exhibits a logarithmic singularity for $C \downarrow 0$, which is integrable on $\mathbb{R}^2$. With $a = x_2, b = y_2$, and $C = (x_2-y_2)^2$ this gives

$$\begin{aligned}
&\int_{T_{ref}} \int_{T_{ref}} \frac{1}{|x-y|}\; dy\; dx \\
= &\int_{y_2=0}^{y_2=1} \int_{x_2=0}^{x_2=1} (x_2-y_2)\log(-(x_2-y_2)+\sqrt{2}|x_2-y_2|)\; dx_2\; dy_2 \\
&-\int_{y_2=0}^{y_2=1} \int_{x_2=0}^{x_2=1} (x_2-1)\log(-(x_2-1)+\sqrt{(x_2-y_2)^2+(x_2-1)^2})\; dx_2\; dy_2 \\
&-\int_{y_2=0}^{y_2=1} \int_{x_2=0}^{x_2=1} \sqrt{(x_2-y_2)^2+(x_2-1)^2}\; dx_2\; dy_2 \\
&-\int_{y_2=0}^{y_2=1} \int_{x_2=0}^{x_2=1} (1-y_2)\log(-(1-y_2)+\sqrt{(x_2-y_2)^2+(1-y_2)^2})\; dx_2\; dy_2 \\
&-\int_{y_2=0}^{y_2=1} \int_{x_2=0}^{x_2=1} \sqrt{(x_2-y_2)^2+(1-y_2)^2}\; dx_2\; dy_2 \\
&+\int_{y_2=0}^{y_2=1} \int_{x_2=0}^{x_2=1} (1+\sqrt{2})|x_2-y_2|\; dx_2\; dy_2\;.
\end{aligned}$$

The formula for the self–energy $I(T_{ref})$ in Lemma 4.1 now follows from the following results regarding the integration w. r. t. x_2 and y_2:

$$\begin{aligned}
&\int_{y_2=0}^{y_2=1} \int_{x_2=0}^{x_2=1} (x_2-y_2)\log(-(x_2-y_2)+\sqrt{2}\,|x_2-y_2|)\; dx_2\; dy_2 \\
&\qquad\qquad = \tfrac{1}{3}\log(-1+\sqrt{2})\;, \quad (7.13)
\end{aligned}$$

$$\int_{y_2=0}^{y_2=1}\int_{x_2=0}^{x_2=1}(x_2-1)\log(-(x_2-1)+\sqrt{(x_2-y_2)^2+(x_2-1)^2})\;dx_2\;dy_2$$
$$=\tfrac{3}{4}+(\tfrac{2}{3}+\tfrac{1}{4}\sqrt{2})\log(-1+\sqrt{2})\;,\quad(7.14)$$

$$\int_{y_2=0}^{y_2=1}\int_{x_2=0}^{x_2=1}\sqrt{(x_2-y_2)^2+(x_2-1)^2}\;dx_2\;dy_2$$
$$=\tfrac{1}{6}(1+\sqrt{2})-\tfrac{1}{6}(1+\tfrac{1}{2}\sqrt{2})\log(-1+\sqrt{2})\;,\quad(7.15)$$

$$\int_{y_2=0}^{y_2=1}\int_{x_2=0}^{x_2=1}(y_2-1)\log(y_2-1+\sqrt{(x_2-y_2)^2+(1-y_2)^2})\;dx_2\;dy_2$$
$$=\tfrac{3}{4}-(\tfrac{2}{3}+\tfrac{1}{4}\sqrt{2})\log(-1+\sqrt{2})\;,\quad(7.16)$$

$$\int_{y_2=0}^{y_2=1}\int_{x_2=0}^{x_2=1}\sqrt{(x_2-y_2)^2+(1-y_2)^2}\;dx_2\;dy_2$$
$$=\tfrac{1}{6}(1+\sqrt{2})-\tfrac{1}{6}(1+\tfrac{1}{2}\sqrt{2})\log(-1+\sqrt{2})\;,\quad(7.17)$$

and

$$\int_{y_2=0}^{y_2=1}\int_{x_2=0}^{x_2=1}|x_2-y_2|\;dx_2\;dy_2\;=\;\tfrac{1}{3}\;.$$

The last integration in this list needs no proof, and formula (7.17) follows from (7.15) by symmetry. We address (7.13):

$$\begin{aligned}
&\int_{b=0}^{b=1}\int_{a=0}^{a=1}(a-b)\log(-(a-b)+\sqrt{2}|a-b|)\;da\;db\\
=\;&\int_{b=0}^{b=1}\int_{a=0}^{a=b}(a-b)\log((b-a)(1+\sqrt{2}))\;da\;db\\
&+\int_{b=0}^{b=1}\int_{a=b}^{a=1}(a-b)\log((a-b)(-1+\sqrt{2})\;da\;db\\
=\;&\int_{b=0}^{b=1}\int_{a=0}^{a=b}(a-b)\log(b-a)\;da\;db-\int_{b=0}^{b=1}\int_{a=0}^{a=b}(a-b)\log(-1+\sqrt{2})\;da\;db\\
&+\int_{b=0}^{b=1}\int_{a=b}^{a=1}(a-b)\log(a-b)\;da\;db\;+\int_{b=0}^{b=1}\int_{a=b}^{a=1}(a-b)\log(-1+\sqrt{2})\;da\;db\\
=\;&-\tfrac{1}{3}\log(-1+\sqrt{2})\;.
\end{aligned}$$

Next we consider (7.14): for any $0\le a\le 1$ there holds

$$\begin{aligned}
&\int_{b=0}^{b=1}(1-a)\log(-(a-1)+\sqrt{(a-b)^2+(a-1)^2})\;db\\
=\;&(1-a)\Big[-b+(b-a)\log(1-a+\sqrt{(a-b)^2+(a-1)^2})\\
&\qquad+(1-a)\log(b-a+\sqrt{(a-b)^2+(a-1)^2})\Big]_{b=0}^{b=1}\\
=\;&2(1-a)^2\log((1-a)(1+\sqrt{2}))-(1-a)+a(1-a)\log(1-a+\sqrt{a^2+(1-a)^2})\\
&\quad-(1-a)^2\log(-a+\sqrt{a^2+(1-a)^2})\;,
\end{aligned}$$

where

$$\begin{aligned}
\int_{a=0}^{a=1} -(1-a)\ da &= -\tfrac{1}{2}\ , \\
\int_{a=0}^{a=1} 2(1-a)^2 \log((1-a)(1+\sqrt{2}))\ da &\overset{(7.11)}{=} -\tfrac{2}{9} - \tfrac{2}{3}\log(-1+\sqrt{2})\ , \\
\int_{a=0}^{a=1} a(1-a)\log(1-a+\sqrt{a^2+(1-a)^2})\ da &\overset{(7.1)}{=} -\tfrac{2}{9} - \tfrac{5}{24}\sqrt{2}\log(-1+\sqrt{2})\ , \\
\int_{a=0}^{a=1} -(1-a)^2\log(-a+\sqrt{a^2+(1-a)^2})\ da &\overset{(7.2)}{=} \tfrac{7}{36} - \tfrac{1}{24}\sqrt{2}\log(-1+\sqrt{2})\ .
\end{aligned}$$

Summing up gives (7.14). We turn to (7.15): for any $0 \le a \le 1$ there holds

$$\begin{aligned}
&\int_{b=0}^{b=1} \sqrt{(a-b)^2+(a-1)^2}\ db \\
&= \tfrac{1}{2}\Big[(b-a)\sqrt{(a-b)^2+(a-1)^2} + -(1-a)^2\log(a-b+\sqrt{(a-b)^2+(a-1)^2})\Big]_{b=0}^{b=1} \\
&= \tfrac{1}{2}\sqrt{2}(1-a)^2 - \tfrac{1}{2}(1-a)^2\log((1-a)(-1+\sqrt{2})) + \tfrac{1}{2}a\sqrt{a^2+(1-a)^2} \\
&\qquad + \tfrac{1}{2}(1-a)^2\log(a+\sqrt{a^2+(1-a)^2})\ ,
\end{aligned}$$

where

$$\begin{aligned}
\int_{a=0}^{a=1} \tfrac{1}{2}\sqrt{2}(1-a)^2\ da &= \tfrac{1}{6}\sqrt{2}\ , \\
\int_{a=0}^{a=1} -\tfrac{1}{2}(1-a)^2\log((1-a)(-1+\sqrt{2}))\ da &\overset{(7.11)}{=} \tfrac{1}{18} - \tfrac{1}{6}\log(-1+\sqrt{2})\ , \\
\int_{a=0}^{a=1} \tfrac{1}{2}a\sqrt{a^2+(1-a)^2}\ da &\overset{(7.10)}{=} \tfrac{1}{8} - \tfrac{1}{16}\sqrt{2}\log(-1+\sqrt{2})\ , \\
\int_{a=0}^{a=1} \tfrac{1}{2}(1-a)^2\log(a+\sqrt{a^2+(1-a)^2})\ da &\overset{(7.2)}{=} -\tfrac{1}{72} - \tfrac{1}{48}\sqrt{2}\log(-1+\sqrt{2})\ .
\end{aligned}$$

Summing up yields (7.15). Finally we consider (7.16): for any $0 \le a \le 1$ there holds

$$\begin{aligned}
&\int_{b=0}^{b=1} (a-1)\log(a-1+\sqrt{(a-b)^2+(a-1)^2})\ db \\
&= (a-1)\Big[-b - a\log(b-a)^2 + b\log(a-1+\sqrt{(a-b)^2+(a-1)^2}) \\
&\quad + a\log(1-a+\sqrt{(a-b)^2+(a-1)^2}) + (a-1)\log(b-a+\sqrt{(a-b)^2+(a-1)^2})\Big]_{b=0}^{b=1} \\
&= -(a-1) + 2a(a-1)\log(-1+\sqrt{2}) + 2a(a-1)\log a \\
&\quad + a(1-a)\log(1-a+\sqrt{a^2+(1-a)^2}) - (1-a)^2\log(-a+\sqrt{a^2+(1-a)^2})\ ,
\end{aligned}$$

where

$$\begin{aligned}
\int_{a=0}^{a=1} -(a-1)\ da &= \tfrac{1}{2}\ , \\
\int_{a=0}^{a=1} 2a(a-1)\log(-1+\sqrt{2})\ da &= -\tfrac{1}{3}\log(-1+\sqrt{2})\ , \\
\int_{a=0}^{a=1} 2a(a-1)\log a\ da &= \tfrac{5}{18}\ , \\
\int_{a=0}^{a=1} a(1-a)\log(1-a+\sqrt{a^2+(1-a)^2})\ da &\overset{(7.1)}{=} -\tfrac{2}{9}-\tfrac{5}{24}\sqrt{2}\log(-1+\sqrt{2})\ , \\
\int_{a=0}^{a=1} -(1-a)^2\log(-a+\sqrt{a^2+(1-a)^2})\ da &\overset{(7.2)}{=} \tfrac{7}{36}-\tfrac{1}{24}\sqrt{2}\log(-1+\sqrt{2})\ .
\end{aligned}$$

Again, summing up establishes (7.16), which proofs Lemma 4.1. □

References

[1] E. L. Allgower, K. Georg, and K. Kalik. Computation of weakly and nearly singular integrals over triangles in $\mathbb{R}^3$. *Zb. Rad. Prirod.-Mat. Fak. Ser. Mat.*, 22(1):149–158, 1992.

[2] T. J. Barth and J. A. Sethian. Numerical schemes for the Hamilton-Jacobi and level set equations on triangulated domains. *J. Comput. Phys.*, 145(1):1–40, 1998.

[3] D. Berkov, K. Ramstöck, and A. Hubert. Solving micromagnetic problems: Towards an optimal numerical method. *Phys. Status Solidi A*, 137:207–225, 1993.

[4] S. Börm and W. Hackbusch. Hierarchical quadrature for singular integrals. *Computing*, 74(2):75–100, 2005.

[5] S. Börm and J. Ostrowski. Fast evaluation of boundary integral operators arising from an eddy current problem. *J. Comput. Phys.*, 193(1):67 – 85, 2004.

[6] F. Bornemann and C. Rasch. Finite-element discretization of static Hamilton-Jacobi equations based on a local variational principle. *Comput. Vis. Sci.*, 9(2):57–69, 2006.

[7] D. Braess. *Finite elements*. Cambridge University Press, Cambridge, third edition, 2007. Theory, fast solvers, and applications in elasticity theory, Translated from the German by Larry L. Schumaker.

[8] S. C. Brenner and L. R. Scott. *The mathematical theory of finite element methods*, volume 15 of *Texts in Applied Mathematics*. Springer-Verlag, New York, second edition, 2002.

[9] F. Brezzi and M. Fortin. *Mixed and hybrid finite element methods*, volume 15 of *Springer Series in Computational Mathematics*. Springer-Verlag, New York, 1991.

[10] P. Bryant and H. Suhl. Thin-film magnetic patterns in an external field. *Appl. Phys. Lett.*, 54:2224–2226, 1989.

[11] C. Carstensen and D. Praetorius. Effective simulation of a macroscopic model for stationary micromagnetics. *Comput. Methods Appl. Mech. Engrg.*, 194(2-5):531–548, 2005.

[12] M. Costabel. Boundary integral operators on Lipschitz domains: elementary results. *SIAM J. Math. Anal.*, 19(3):613–626, 1988.

[13] M. G. Crandall, L. C. Evans, and P.-L. Lions. Some properties of viscosity solutions of Hamilton-Jacobi equations. *Trans. Amer. Math. Soc.*, 282(2):487–502, 1984.

[14] M. G. Crandall and P.-L. Lions. Viscosity solutions of Hamilton-Jacobi equations. *Trans. Amer. Math. Soc.*, 277(1):1–42, 1983.

[15] A. DeSimone. Energy minimizers for large ferromagnetic bodies. *Arch. Rational Mech. Anal.*, 125(2):99–143, 1993.

[16] A. Desimone, R. V. Kohn, S. Müller, and F. Otto. A reduced theory for thin-film micromagnetics. *Comm. Pure Appl. Math.*, 55(11):1408–1460, 2002.

[17] A. DeSimone, R. V. Kohn, S. Müller, F. Otto, and R. Schäfer. Two-dimensional modelling of soft ferromagnetic films. *R. Soc. Lond. Proc. Ser. A Math. Phys. Eng. Sci.*, 457(2016):2983–2991, 2001.

[18] P. Deuflhard. *Newton methods for nonlinear problems*, volume 35 of *Springer Series in Computational Mathematics*. Springer-Verlag, Berlin, 2004. Affine invariance and adaptive algorithms.

[19] J. Drwenski and F. Otto. $\mathcal{H}^2$-matrix method vs. FFT in thin-film stray-field computations. *SFB preprint*, 161, 2004.

[20] D. A. Dunavant. High degree efficient symmetrical Gaussian quadrature rules for the triangle. *Internat. J. Numer. Methods Engrg.*, 21(6):1129–1148, 1985.

[21] S. C. Eisenstat and H. F. Walker. Choosing the forcing terms in an inexact Newton method. *SIAM J. Sci. Comput.*, 17(1):16–32, 1996. Special issue on iterative methods in numerical linear algebra (Breckenridge, CO, 1994).

[22] V. J. Ervin, E. P. Stephan, and S. Abou El-Seoud. An improved boundary element method for the charge density of a thin electrified plate in $\mathbb{R}^3$. *Math. Methods Appl. Sci.*, 13(4):291–303, 1990.

[23] A. V. Fiacco and G. P. McCormick. *Nonlinear programming*, volume 4 of *Classics in Applied Mathematics*. Society for Industrial and Applied Mathematics (SIAM), Philadelphia, PA, second edition, 1990. Sequential unconstrained minimization techniques.

[24] M. Frigo and S. G. Johnson. FFTW: An adaptive software architecture for the FFT. In *Proc. 1998 IEEE Intl. Conf. Acoustics Speech and Signal Processing*, volume 3, pages 1381–1384. IEEE, 1998.

[25] L. Grasedyck and W. Hackbusch. Construction and arithmetics of $\mathcal{H}$-matrices. *Computing*, 70(4):295–334, 2003.

[26] L. Greengard and V. Rokhlin. A fast algorithm for particle simulations. *J. Comput. Phys.*, 73(2):325–348, 1987.

[27] W. Hackbusch. *Integral equations*, volume 120 of *International Series of Numerical Mathematics*. Birkhäuser Verlag, Basel, 1995. Theory and numerical treatment, Translated and revised by the author from the 1989 German original.

[28] W. Hackbusch. A sparse matrix arithmetic based on $\mathcal{H}$-matrices. I. Introduction to $\mathcal{H}$-matrices. *Computing*, 62(2):89–108, 1999.

[29] W. Hackbusch and S. Börm. $\mathcal{H}^2$-matrix approximation of integral operators by interpolation. *Appl. Numer. Math.*, 43(1-2):129–143, 2002. 19th Dundee Biennial Conference on Numerical Analysis (2001).

[30] W. Hackbusch, L. Grasedyck, and S. Börm. An introduction to hierarchical matrices. In *Proceedings of EQUADIFF, 10 (Prague, 2001)*, volume 127, pages 229–241, 2002.

[31] W. Hackbusch, B. Khoromskij, and S. A. Sauter. On $\mathcal{H}^2$-matrices. In *Lectures on applied mathematics (Munich, 1999)*, pages 9–29. Springer, Berlin, 2000.

[32] W. Hackbusch and B. N. Khoromskij. A sparse $\mathcal{H}$-matrix arithmetic. II. Application to multi-dimensional problems. *Computing*, 64(1):21–47, 2000.

[33] W. Hackbusch and Z. P. Nowak. On the fast matrix multiplication in the boundary element method by panel clustering. *Numer. Math.*, 54(4):463–491, 1989.

[34] M. R. Hestenes and E. Stiefel. Methods of conjugate gradients for solving linear systems. *J. Research Nat. Bur. Standards*, 49:409–436 (1953), 1952.

[35] R. Hiptmair. Finite elements in computational electromagnetism. *Acta Numer.*, 11:237–339, 2002.

[36] A. Hubert and M. Rührig. Micromagnetic analysis of thin-film elements. *J. Appl. Phys.*, 69:6073–6077, 1991.

[37] A. Hubert and Schäfer. *Magnetic domains*. Springer, 1998.

[38] H. Ishii. A simple, direct proof of uniqueness for solutions of the Hamilton-Jacobi equations of eikonal type. *Proc. Amer. Math. Soc.*, 100(2):247–251, 1987.

[39] P.-L. Lions. *Generalized solutions of Hamilton-Jacobi equations*, volume 69 of *Research Notes in Mathematics*. Pitman (Advanced Publishing Program), Boston, Mass., 1982.

[40] O. L. Mangasarian. *Nonlinear programming*. McGraw-Hill Book Co., New York, 1969.

[41] G. P. McCormick and C. Witzgall. Logarithmic SUMT limits in convex programming. *Math. Program.*, 90(1, Ser. A):113–145, 2001.

[42] J. A. Morrison and J. A. Lewis. Charge singularity at the corner of a flat plate. *SIAM J. Appl. Math.*, 31(2):233–250, 1976.

[43] W. Murray. Analytical expressions for the eigenvalues and eigenvectors of the Hessian matrices of barrier and penalty functions. *J. Optimization Theory Appl.*, 7:189–196, 1971.

[44] J. Nocedal and S. J. Wright. *Numerical optimization*. Springer Series in Operations Research and Financial Engineering. Springer, New York, second edition, 2006.

[45] N. Popović and D. Praetorius. Applications of $\mathcal{H}$-matrix techniques in micromagnetics. *Computing*, 74(3):177–204, 2005.

[46] W. H. Press, S. A. Teukolsky, W. T. Vetterling, and B. P. Flannery. *Numerical recipes in C++*. Cambridge University Press, Cambridge, 2002. The art of scientific computing, Second edition, updated for C++.

[47] P.-A. Raviart and J. M. Thomas. A mixed finite element method for 2nd order elliptic problems. In *Mathematical aspects of finite element methods (Proc. Conf., Consiglio Naz. delle Ricerche (C.N.R.), Rome, 1975)*, pages 292–315. Lecture Notes in Math., Vol. 606. Springer, Berlin, 1977.

[48] E. Rouy and A. Tourin. A viscosity solutions approach to shape-from-shading. *SIAM J. Numer. Anal.*, 29(3):867–884, 1992.

[49] A. Schmidt and K. G. Siebert. *Design of adaptive finite element software*, volume 42 of *Lecture Notes in Computational Science and Engineering*. Springer-Verlag, Berlin, 2005. The finite element toolbox ALBERTA, With 1 CD-ROM (Unix/Linux).

[50] J. A. Sethian. *Level set methods and fast marching methods*, volume 3 of *Cambridge Monographs on Applied and Computational Mathematics*. Cambridge University Press, Cambridge, second edition, 1999. Evolving interfaces in computational geometry, fluid mechanics, computer vision, and materials science.

[51] J. Stoer and C. Witzgall. *Convexity and optimization in finite dimensions. I.* Die Grundlehren der mathematischen Wissenschaften, Band 163. Springer-Verlag, New York, 1970.

[52] T. von Petersdorff. *Randwertprobleme der Elastizitätstheorie für Polyeder – Singularitäten und Approximation mit Randelementmethoden*. Dissertation, Universität Darmstadt, 1989.

[53] M. H. Wright. Why a pure primal Newton barrier step may be infeasible? *SIAM J. Optim.*, 5(1):1–12, 1995.